3-2003

Development of an Experimental Test Section for Forcing Unsteady Flow in a Linear Compressor Cascade Using Circular Rods

Patrick C. Wade

DEVELOPMENT OF AN EXPERIMENTAL TEST SECTION FOR FORCING UNSTEADY FLOW IN A LINEAR COMPRESSOR CASCADE USING CIRCULAR RODS

DISSERTATION

Patrick C. Wade
Captain, USAF

AFIT/DS/ENY/02-4

DEPARTMENT OF THE AIR FORCE

AIR UNIVERSITY

AIR FORCE INSTITUTE OF TECHNOLOGY

Wright-Patterson Air Force Base, Ohio

Report Documentation Page

Report Date	Report Type	Dates Covered (from... to)
25 Mar 03	N/A	-

Title and Subtitle Development of an Experimental Test Section for Forcing Unsteady Flow in a Linear Compressor Cascade using Circular Rods	**Contract Number**
	Grant Number
	Program Element Number
Author(s)	**Project Number**
	Task Number
	Work Unit Number
Performing Organization Name(s) and Address(es) Air Force Institute of Technology Graduate School of Engineering and Management (AFIT/EN) 2950 Hobson Way WPAFB OH 45433-7765	**Performing Organization Report Number** AFIT/DS/ENY/02-4
Sponsoring/Monitoring Agency Name(s) and Address(es) sponsoring agency and address	**Sponsor/Monitor's Acronym(s)**
	Sponsor/Monitor's Report Number(s)
Distribution/Availability Statement Approved for public release, distribution unlimited	
Supplementary Notes The original document contains color images.	
Abstract	
Subject Terms	
Report Classification unclassified	**Classification of this page** unclassified
Classification of Abstract unclassified	**Limitation of Abstract** UU
Number of Pages 200	

The views expressed in this dissertation are those of the author and do not reflect the official policy or position of the United States Air Force, Department of Defense, or the United States Government.

AFIT/DS/ENY/02-4

DEVELOPMENT OF AN EXPERIMENTAL TEST SECTION FOR FORCING UNSTEADY FLOW IN A LINEAR COMPRESSOR CASCADE USING CIRCULAR RODS

DISSERTATION

Presented to the Faculty

Graduate School of Engineering and Management

Air Force Institute of Technology

Air University

Air Education and Training Command

In Partial Fulfillment of the

Requirements for the Degree of

Doctor of Philosophy

Patrick C. Wade, B.S., M.S.

Captain, USAF

March 2003

Acknowledgments

I wish to acknowledge the efforts of everyone involved with this project. The contributions from the AFIT machine shop employees, notably Russ Hastings and Condie Inman were critical to the completion of this project. Their attention to detail and excellent workmanship allowed all of the pieces to fit together.

A special thanks goes to Andy Pitts, whom I leaned on very heavily for all aspects of the tunnel operation and instrumentation. Capt David Hopper provided the initial experimental set-up and worked out many of the bugs in the data acquisition software and the instrumentation. Thanks goes to Dr. Rolf Sondergaard who provided the procedure and calibration routines necessary to use the x-wire sensors with the IFA-100.

I wish to thank Lt. Col. Ray Maple for the extended hours that he spent helping me become Linux literate and learning how to use Fluent on the Beowulf cluster.

I owe the greatest debt to Dr. Paul King, who was my advisor for this project, for providing ideas and support for this project. With his help, I was able to make sense of my results and complete the work. Finally, I wish to thank Dr. Tom Buetner at AFOSR who provided the funding for this work.

Patrick C. Wade

Table of Contents

List of Figures

List of Tables

Nomenclature

Symbol	*Description*
a	Calibration constants
a	Speed of Sound
A	Amplitude
C	Calibration constant
d	Distance between cylinder centerlines
D	Calibration constant
D	Cylinder diameter
E	Bridge voltage
f	Cylinder shedding frequency
F	Force
g	gravity
k	Ratio of voltages for split film
M	Mach number
n	Number of cylinders
n	Calibration constant
Nu	Nusselt Number
r	Radial distance from cylinder center
R	Radius of cylinder
R_V	Velocity ratio
Re	Reynolds number
Re_{ns}	Unsteady Reynolds number
u	X-component velocity
$\bar{u}$	X-component mean velocity

v	Y-component velocity
$\bar{v}$	Y-component mean velocity
V_∞	Freestream velocity
$\vec{V}$	Velocity magnitude
Greek Symbols	
α	Angle of flow with sensor axis
ϵ	Error
Γ	Circulation
ω	Shedding frequency, radians
ϕ	Velocity potential
ρ	Density
θ	Angle from centerline of cylinder
Subscripts	
∞	Freestream
$0-3$	Calibration terms
1	Wire 1
2	Wire 2
$angle$	Angle calibration constants
$blade$	Blade surface
$calc$	Value obtained analytically
cfd	Computational value
$desired$	Value desired for analytical analysis
p	Phase
p	Pressure surface of blade
ph	Unsteady pressure at first harmonic of shedding frequency

pp	Unsteady pressure at shedding frequency
uh	Unsteady x-component of velocity at first harmonic of shedding frequency
up	Unsteady x-component of velocity at shedding frequency
vel	Velocity
vh	Unsteady y-component of velocity at first harmonic of shedding frequency
vp	Unsteady y-component of velocity at shedding frequency
s	Suction side of blade

List of Abbreviations

Abstract

Upstream propagating waves impinging on a cascade of compressor blades were examined in an effort to better understand the influence of downstream components on high cycle fatigue in turbine engines. An array of cylinders was used to simulate the unsteady field generated by a rotor downstream of a set of stators. The unsteady flow upstream of a single cylinder and an array of cylinders, with and without an upstream cascade, was examined experimentally and computationally. Computational results indicate that the cylinders would only shed coherently when placed downstream of a set of blades. Coherent shedding is created when each of the cylinders in the array shed a vortex at the same instant in time. The computational results were verified experimentally and the required flow conditions for coherent vortex shedding were examined. Coherent vortex shedding was maximized by placing the cylinders in the centerline of the blade passages. The unsteady velocity was measured over a cascade blade with the cylinders located in an array downstream of the blades. Unsteady velocities measured along the blade indicate that the downstream cylinders create upstream propagating velocity fluctuations that are maximum at the trailing edge. The increasing amplitude of the unsteady velocities towards the trailing edge of the blade was seen both experimentally and computationally. Additionally, the computational results show that the unsteady fluctuations in the pressure along the blade surface also increases towards the trailing edge of the blade. The magnitude of the upstream propagating velocity fluctuations was increased with increasing freestream velocity. Unsteady velocities generated by individual cylinders were superposed to recreate the unsteady flowfield of the cylinder array and compared favorably with the cylinder array results towards the trailing edge of the blade.

DEVELOPMENT OF AN EXPERIMENTAL TEST SECTION FOR FORCING UNSTEADY FLOW IN A LINEAR COMPRESSOR CASCADE USING CIRCULAR RODS

I. Introduction

The unsteady flow field within rotating turbomachinery remains poorly understood today. This unsteady flow can cause high cycle fatigue (HCF), a leading cause of failures and required maintenance in turbomachinery. El-Aini et al. [1] state that HCF can be described as a fatigue that results in cracking or fracture from a large number of cyclic stresses below the yield strength of the material. Much of HCF research in turbomachinery has focused on the need for increased reliability and durability of components, thus reducing both maintenance and operational costs while increasing flight safety, according to White [2].

The impact of HCF issues on engine design and operation is very large. El-Aini et al. [1] claim that while over 90% of HCF problems are discovered during the development testing of new engines, the remaining 10% account for nearly 30% of the total development cost and can lead to over 25% of all engine distress events. The average developmental program has over two serious HCF problems that must be resolved, according to Wisler and Shin [3]. For example, failure of fan and compressor airfoils was the second leading cause of in-flight engine shut down, and the third leading cause for aborted take-offs for commercial aircraft during a two-year span. During the same time period, turbine airfoil failures and fan and compressor airfoil failures were the two leading causes of unscheduled engine removal, according to Wisler [4]. These blade failures are mostly due to HCF effects [3]. Wisler and Shin estimate that approximately 5% of commercial field maintenance costs are caused by HCF failures.

The impact of HCF damage is a major concern not limited to the civil airline fleet; the U.S. Air Force also has large expenses and flight mishaps caused by HCF. According to

Thompson [5], high cycle fatigue has been attributed to 56% of the U.S. Air Force fighter-aircraft engine-safety mishaps between 1982 to 1996. Thompson and Griffin [6] state that approximately 30% of the U.S. Air Force maintenance budget is estimated to be absorbed by HCF-related engine mishaps. Military costs for HCF-related issues are expected to be in the billions through the year 2020, according to Wisler and Shin [3]. It is hoped that through a more accurate understanding of HCF these figures can be reduced.

1.1 Causes of High Cycle Fatigue

HCF is a result of vibratory stress cycles produced in engine flows with moderate levels of steady stresses applied at a frequency typically in the range of 100 Hz through 20 kHz, as stated by El-Aini et al. [1]. The cyclic applied stresses are caused by many factors present in blade-row interaction. This interaction can cause blade vibratory response that Wisler and Shin [3] rank among the most critical of the blade row interactions.

Periodic forces occur in a rotating environment as rotor blades move past vanes, perturbing the flow field upstream and downstream. According to Johnston and Fleeter [7, 8], the two main types of disturbances are vortical wakes and potential disturbances. Vortical wakes are total pressure deficits that are caused by viscous effects along a body. These wakes convect with the mean flow and decay slowly [7]. Potential disturbances, an inviscid effect, propagate at acoustic velocity both upstream and downstream and decay rapidly with distance [9]. The unsteady potential disturbances originate from the fluctuating bound vorticity generated as blade incidence rises and falls during transit through wakes and propagate both upstream and downstream, as noted by Wilson and Korakianitis [10]. Korakianitis [11, 12] showed that the potential disturbances and convected wakes can interact with a blade row to achieve a destructive interference for certain cases of stator-rotor gap and pitch ratio.

The effects of the upstream propagating potential waves have been largely ignored in the past. These waves have been shown by Fabian [13] to create disturbances of similar magnitude as the downstream propagating wakes. The need for a more detailed look at the effects of the upstream propagating waves led to this research.

1.2 Generation of Downstream Forcing

The creation of unsteady waves propagating upstream was of prime importance for this work. It was desired to create a hardware set-up in a linear cascade that would effectively simulate the unsteady flow propagating upstream from a rotor.

One of the requirements for the unsteady forcing was for an easily controlled forcing frequency that would remain stable for a series of runs. The forcing mechanism needed to be fairly easy to control and provide the high frequencies required for this work.

Commerfield and Carta [14] used a cylinder as a source for unsteady forcing on a single blade. This experiment utilized the von Karman vortex shedding from a cylinder placed upstream of a single blade. A pressure tap located inside the cylinder served as a trigger for the data collection that could be used for conditional triggering and phase-locking. This method of forcing was extended by Fabian [13] by placing an array of cylinders in a flow downstream of cascade blades.

There were many benefits to using cylinders. The cylinders produced a strong sinusoidal shedding for a wide range of velocities, and the frequency is a function only of the cylinder diameter and velocity of the flow. Thus, by changing the velocity or the diameter, the forcing frequency could be altered.

The ability to provide phase-locking of the results using the cylinder was easily implemented. By inserting a pressure transducer through the center of the cylinder and placing the pressure tap at the 90 degree point on the cylinder, the vortex shedding of the cylinder is seen as an oscillating voltage from the pressure transducer.

The main benefit of the cylinder was the ease of implementation and the flexibility in experimental set-up. External equipment was not required to produce the varying potential waves, simplifying the system design. The cylinders had only to be placed in the test section and held by the side walls. The cylinder location could easily be changed by simply moving the array to a different location.

The main disadvantage of using the cylinders was the lack of knowledge of the behavior of a cylinder array at high Reynolds numbers. Although much research exists examining the von Karman vortex street produced downstream by a cylinder [15, 16, 17, 18, 19, 20, 21],

little research has been performed to examine the unsteady upstream oscillations generated by a cylinder. For example work by Le Gal, et al. [19] examined the patterns of the wakes behind an array of cylinders for low Reynolds numbers, but the resulting flow was not measured.

Fabian [13] used the cylinder array for potential wave forcing, but an extensive examination of the flow generated by the array was not accomplished. The presence of coherent shedding behavior between the cylinders placed in the array was also an unknown. For this research, a coherent shedding structure from the cylinders was required for the results to be of use for the engine community.

Coherent shedding from an array of cylinders exists when the phase of vortex shedding between any two cylinders is approximately constant. The two main types of coherent shedding are synchronous and asynchronous, as seen in Fig. 1.1. Synchronous shedding is created when each cylinder sheds a vortex on the same side at the same instant in time. Asynchronous shedding occurs when a vortex is shed from the same side of every other cylinder and from the opposite side of the cylinders in between. In an engine, blades of a rotor pass through wakes at approximately the same time if the rotor and stator have approximately the same number of blades, creating an effect similar to synchronous shedding. Asynchronous shedding contains symmetry between every two cylinders, rather than each cylinder. The resulting flow from this shedding would approximate a rotor with half the number of blades of the upstream stator.

1.3 Experimental Work to Date

Fabian and Jumper [22] presented work designed to examine the effects of unsteady forcing on a loaded cascade for the case of either upstream or downstream forcing. An array of cylinders was placed at 80% of the chord (1.02 in) upstream or downstream of a loaded cascade and both the steady and unsteady pressures along the blades were examined. The peak pressure from the top surface of a cylinder triggered and phase-locked the unsteady velocities for subsequent ensemble averaging, reducing the noise present in the system. Fabian and Jumper [22] determined that the unsteady surface pressures resulting from the rearward cylinders was of the same order as the unsteady pressures generated by the wakes

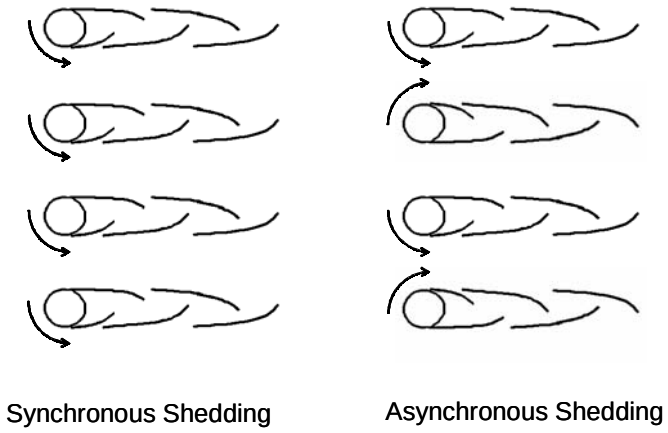

Figure 1.1 Coherent Cylinder Shedding Types

from cylinders placed forward of the blades. Fabian [13] showed that the large unsteady pressures disappeared when the downstream cylinders were removed.

Fabian and Jumper [23] presented further work examining unsteady forcing. In this experiment, rods were placed at 160% chord length (2.04 in) downstream and the unsteady pressures were again measured on the cascade blade surfaces. The results indicated that the cylinders produced acoustically-propagating, potential-like disturbances that interacted with the blades, producing relatively large unsteady pressures towards the trailing edge of the blade. The the blade thickness prevented pressure transducers from being placed aft of 80% chord. Fabian and Jumper [24] extended their work by showing that the unsteady pressure signal originates at the array of cylinders and propagates at acoustic speeds into the flow. The freestream Mach numbers used in this experiment ranged from 0.427 to 0.50.

The work of Fabian and Jumper was extended in actual engine testing performed at the U.S. Air Force Academy in the F109 test cell. Falk et al. [25] examined the flow at various points upstream of the fan of an F109 engine. The fan generated unsteady potential-like waves that propagate upstream at acoustic speed. It was noted that the unsteady velocities were largest at locations closest to the fan and dropped off rapidly with upstream distance. The largest fluctuations in the velocity were present in the swirl direction of the flow, with magnitudes up to 20% of the mean axial velocity at points closest to the fan.

Further work by Falk et al. [26] included an examination of the velocity field downstream of the fan of the F109 engine. The unsteady results indicated a strong vortical and potential interaction occurring in this region of the flow. The flow was accurately predicted through a model containing only the potential and vortical interactions.

Falk et al. [27] extended this work by examining the upstream unsteady pressure effects on a blade located upstream of the F109 engine. A single inlet guide vane (IGV) was placed 0.6 fan-blade chords upstream of the fan and unsteady pressure was taken at 4 different chordwise locations on both vane surfaces. The unsteady pressure differential ($\Delta P'$) measured across the IGV reached maximum amplitudes of six times the dynamic pressure. These unsteady pressure fluctuations contained a noticeable harmonic frequency and exhibited almost no amplitude decay with upstream distance.

In an effort to gain insight into the general physics present, Hopper [28] examined the unsteady velocity field (u') directly upstream of a single cylinder using an x-wire constant temperature anemometer (CTA). Comparison between multiple points in the flow was possible due to phase-locking the acquired voltages, which ensured that the velocity at each point in the flow field corresponded to an identical condition of the cylinder shedding. Hopper showed that there is a measurable influence on both components of the unsteady velocity (u' and v') due to the cylinder. The unsteady velocities were eliminated when Hopper removed the cylinder from the flow [28]. An unsuccessful attempt was made to model the flow using a simple model based on potential flow theory.

1.4 Purpose of Work

The focus of this work was to design a test section that could be used to produce unsteady forcing in a linear cascade through the use of an array of cylinders. This work was a joint project with Notre Dame and was a continuation of Fabian's work [13]. Experimental results of the upstream effects of both a single cylinder and an array of cylinders were required for this work. From this, the goals of this work were to:

1. Examine the unsteady flow upstream of a single cylinder. Very little work [28] has been performed on this subject in the past. Before any understanding can be gained

from the use of a cylinder array, the single cylinder flow must be known. To achieve this goal, both experimental measurements and computational simulations were used for the analysis.

2. Characterize the interaction between cylinders placed in an array. In order for this work to simulate the flow in an engine, coherence of the vortex shedding of cylinders was required. This work would provide the first look into the coherence of an array of cylinders at high velocities and the required flow conditions. Like the single cylinder work, both experimental work and computational simulations were used for a better understanding.

3. Once the requirements for coherence were known, a test section was designed to incorporate this coherence in order to produce the upstream propagating waves.

4. Research [22, 29, 30] has indicated that once the coherence of the cylinders is developed, strong unsteady waves propagate upstream onto the blades of the cascade. This unsteadiness is seen as a peak of the unsteady velocities at the trailing edge of the blades that decreases along the blade length upstream. Through the use of both computational simulations and experiments, the unsteady flow was examined and the peak fluctuations on the trailing edge of the blade were shown, indicating an upstream propagation of potential waves, and rearward rise in velocity fluctuations similar to those inferred by Fabian and Jumper [30].

   As will be shown, the cylinders did produce a measurable unsteady flow upstream of the array. As expected, the cylinders did not shed vortices coherently when the array was located in a freestream flow. However, as predicted by Fabian and Jumper [23], the cylinders shed vortices coherently when placed downstream of a loaded cascade. The unsteady flow generated by the array of cylinders produced unsteady velocity fluctuations along the cascade blades that were larger towards the trailing edge of the blade.

1.5 Organization of This Document

With these goals in mind, a description of the organization of this dissertation is as follows. Chapter II includes an examination of the physics involved in the vortex shedding of a single cylinder. Results of the upstream unsteady flow are presented along with a comparison to a potential model and computational results. Chapter III includes a description of the interaction of multiple cylinders located in an array. Expected requirements for coherent shedding are presented in this chapter.

The results from the cascade are presented in Chapters IV and V. Chapter IV includes the coherence of the cylinder shedding for the array of cylinders located downstream of a loaded cascade. The effects of changing flow and geometrical parameters and thus the coherence of the cylinder shedding are presented. Chapter V contains the velocity measurements along a blade in the cascade. Of importance from these results is the presence of a peak in the unsteady values at the trailing edge of the blades that is present only when the cylinders are shedding coherently.

An examination of the correlation between the unsteady velocity and pressure can be found in Chapter VI. The results of the computational simulations are used to estimate the trends in the unsteady pressures present on the blades.

The conclusions and summary are presented in Chapter VII. Potential ideas for future work are presented in Chapter VIII.

II. Flow Field of a Circular Cylinder

The goal of this research was to understand the unsteady velocity field created by an array of cylinders placed downstream of a loaded cascade. Before the array of cylinders can be understood, the unsteady flow generated by a single cylinder placed in crossflow must be examined and the unsteady velocity understood. The single cylinder effort of this work involved unsteady velocities captured through experiment, CFD, and predicted by a simple potential flow model suggested by Fabian and Jumper [24] and Hopper [28].

2.1 Characteristics of Vortex Shedding

The vortex shedding created by a single cylinder in crossflow has been heavily studied for a wide range of Reynolds numbers by many researchers [31]. For the Reynolds numbers used in this research (approximately 40,000 based on the cylinder diameter), the vortex street produced by the cylinder frequency contains a strong component at a single frequency although the amplitude of the shedding is highly irregular, according to Fung [32]. The Reynolds number based on cylinder diameter is defined as

$$\mathrm{Re} = \frac{DU_\infty}{\nu} \tag{2.1}$$

where D is the cylinder diameter, U_∞ is the freestream velocity, and ν is the kinematic velocity.

Causes of vortex shedding. The vortex shedding from a cylinder is asymmetric and is caused by the viscosity of the flow. The vortex street begins as vorticity is initially shed from the surface of the cylinder [33]. These separating shear layers contain well-defined concentrations of vorticity [34]. This vorticity entrains the adjacent irrotational flow and eventually forms the large-scale vortices present in the von Karman vortex street [33]. The circulation from the vortices in the wake influence the cylinder location upstream and can control the separation region of the cylinder [33].

Vortex shedding frequency. The shedding frequency of the vortices from a cylinder can be easily calculated through the use of the Strouhal number (S), defined as

$$S = \frac{fD}{V_\infty} \tag{2.2}$$

where f is the shedding frequency, D is the cylinder diameter, and V_∞ is the freestream velocity of the flow. According to White [31], the Strouhal number is equal to a constant value of 0.2 for values of Reynolds numbers studied for this research ($10^4 - 10^5$). The frequency of the shedding can be determined from Eq. (2.2) as solely a function of cylinder diameter and velocity, for the case of constant Strouhal number, as

$$f = \frac{0.2V_\infty}{D} \tag{2.3}$$

The shedding frequency, and thus the forcing frequency, can be controlled through the choice of the diameter of the cylinder and the velocity of the freestream. For this research, the cylinder shedding frequency was 5.25 kHz, corresponding to a freestream velocity of 125 m/s and cylinder diameter of 3/16 inches. According to Sarpkaya and Shoaff [16], oscillating lift is created by each period of vortex shedding, and the drag fluctuates at a frequency of twice the vortex shedding with a peak corresponding to each individual shed vortex. The frequency content of the unsteady cylinder pressures, and thus the flow velocities and pressures, desired for this work would include 5.25 and 10.5 kHz, the primary and first harmonic of the shedding frequency, respectively.

Although the shedding of the vortices from a cylinder produces a distinct vortex street that is reproducible on for $40 < \mathrm{Re} < 190$, Wille [15] proved that periodic vortex shedding exists at Reynolds numbers up to 10^7 and Eq. (2.3) remains valid for this Reynolds number range.

Three dimensional effects. Of major concern for this effort is the possibility of three dimensional effects influencing the results. In previous work performed by Hopper [28], the flow over a cylinder was assumed to be two dimensional. The assumption of two-dimensional flow allowed the hot-wire probe to be located off the test section center-

line along the cylinder span (1/2 inch in the work by Hopper [28]) to reduce the probe interference of the pressure tap on the cylinder.

In work performed by Szepessy [35] aimed at determining any three-dimensional effects of cylinder shedding at high subcritical Reynolds numbers ($\mathrm{Re} = 4.3 \times 10^4$), pressure taps were placed at various spanwise positions on a cylinder and the correlation between the shedding phase at each of the locations was examined. Szepessy's research determined that for a spanwise distance less than the diameter of the cylinder ($\Delta z/D < 1$), the probability distribution of the shedding phase was fairly narrow banded. At spanwise distances from two to four diameters, the probability distribution appeared to be broader and fit a Gaussian curve. For distances greater than six times the diameter, the fluctuations appeared to be fully random with a uniform probability distribution.

For the single cylinder experiment, the probe spanwise distance was 1/4 inch ($\Delta z/D = 1.33$). For this value, the time-dependent phase lag of the cylinder shedding exhibits a nearly Gaussian probability distribution with the mean at zero phase lag, according to Szepessy [35]. The effects of the uncertainty of the shedding can be reduced through the use of ensemble averaging. Due to the characteristic peak of a Gaussian probability, the shedding phase of a point on the cylinder located 1/4 inch away from the pressure tap will, on average, equal the shedding phase at the pressure tap.

2.2 Experimental Set-up

Tunnel. The testing for this research was performed at the Air Force Institute of Technology in the compressor cascade test facility. As shown in Fig. 2.1, this tunnel is an open exhaust blow-down facility. The airflow through the tunnel is provided by a 40-hp centrifugal blower which draws air through a 12 in duct from outside the building. The blower is rated at 3000 ft^3/min at 1.6 psig total head. The air pulled from outside the building is drawn through an electrostatic filter prior to passing through the blower and into the wind tunnel. After passing through the blower, the air passes into a 9 ft long diffuser with a divergence half angle of 7 deg. At this point, compressed house air at 100 psig can be added to the flow at the diffuser through a permanent ejector system. Upon exiting the diffuser, the airflow has been reduced to approximately 20 ft/sec.

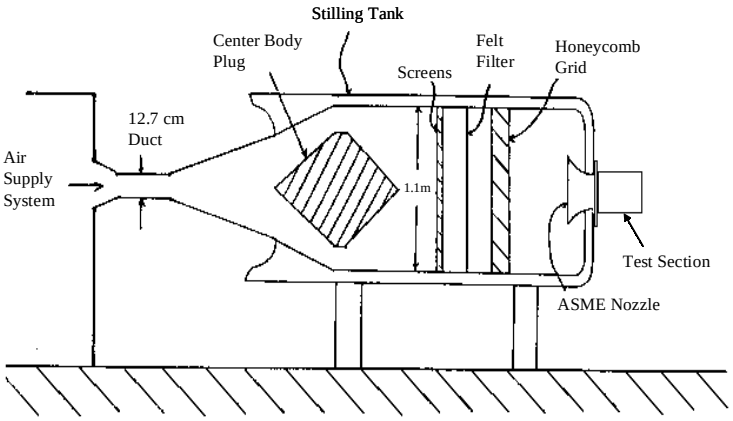

Figure 2.1 AFIT Cascade Test Facility (From Hopper [28])

The major influence in the quality of the airflow (i.e., lack of turbulence, constant freestream flow) is the design of the stilling chamber. The stilling chamber consists of a center body plug located in the center of the entrance of the chamber. This plug, covered with two-inch thick foam rubber, aides in the diffusion process of the airflow and reduces the airflow to approximately 10 ft/sec at the exit of the plug. Additionally, the plug location reduces the possibility of acoustic noise passing from the air supply system into the test section [36].

After passing around the center body plug, the flow passes through one layer of 40 mesh wire. The purpose of this screen is to provide a slight back pressure to the divergent portion of the center body plug and also to trap any particulate matter which may exist in the system. The flow then passes through a 4 in thick honeycomb grid designed to straighten the flow. Prior to entering the test section, the flow is finally passed through a 2-D long radius ASME bell mouth nozzle designed to accelerate the flow to the flow conditions desired in the test section. The turbulence level of the flow entering the test section is 1.5%, as measured by Allison [36]. Additional information regarding the tunnel design can be found in Allison [36].

The blower could only produce a maximum freestream velocity of approximately 130 m/s, lower than the slowest velocity reported in Fabian's work [13]. Higher velocities can be achieved through the use of the compressed air system, however run times become limited by the decreasing pressure of the compressed air system. Velocities up to 150 m/s

were achieved using this system, but the volume of compressed air available limited run time to a maximum of ten seconds.

For the velocity data obtained in this work, only the blower was used. Cylinder pressure results taken with the compressed air on and off showed the overall character of the flow was the same for the blower on and off cases. Freestream velocities of 110 m/s and 125 m/s were used for gathering velocity data.

One undesirable side effect of operating the tunnel at high speeds is the large increase in the flow temperature. The outside air is heated through the blower to temperatures over $100^{\circ}F$. The tunnel stagnation temperatures can approach $120^{\circ}F$ on a warm day. The increased temperature of the flow was a factor in the velocity measurements and was corrected using equations with temperature corrections.

Test section. Hopper [28] designed and used the test section to examine the upstream propagation of potential-like waves from a cylinder at a velocity of approximately 60 m/s. For the current work, the test section was used at the tunnel velocity of 125 m/s.

The dimensions of the test section were designed specifically to match the dimensions of the existing mating collar on the tunnel. The cross-sectional dimensions are 2 inches wide by 8 inches high, giving a throat area of 16 in^2, as recommended by Allison [36]. The length of the test section varies depending on the current experimental set-up, ranging from 7.5 to 9.75 inches. The tunnel was designed to have portions of the side walls move downstream to allow the downstream distance between the split-film probe and the cylinder to be increased while using a single split-film insertion point into the tunnel.

The height of the cylinder was set using sliders along the tunnel wall, allowing the cylinder to be placed at different height locations without disassembling the test section. The cylinder spanned the entire two inch width of the test section and contained a hole drilled in the center of the cylinder to measure pressure at the midspan of the cylinder. The position of the cylinder in relation to the split-film sensor can be seen in Fig. 2.2.

The cylinder diameter was chosen to be $3/16 \pm 0.0005$ inch to allow direct comparisons between this work and the work of both Hopper [28] and Fabian [13]. The original choice of the cylinder diameter was made by Fabian to match the reduced frequency present in

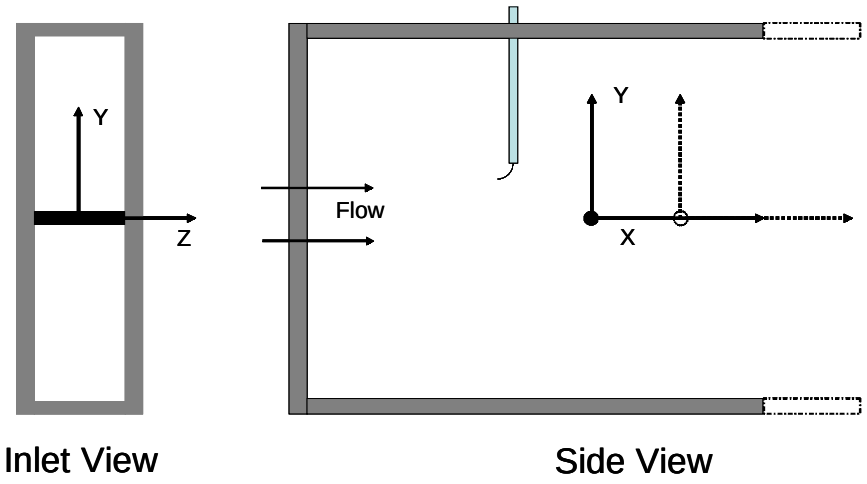

Figure 2.2 Single Cylinder Test Section

the F109 engine compressor of 4.5, calculated by

$$\tilde{f} = \frac{fc}{2V_\infty} \tag{2.4}$$

where f is the cylinder shedding frequency, c is the chord vane chord, and V_∞ is the freestream velocity.

For the purposes of this research, a new hole was drilled in the top of the tunnel 1/2 inch upstream of the farthest upstream cylinder position and 1/4 inch off-center of the width of the tunnel. The offset from the center of the tunnel was used to reduce flow interference from the split-film sensor over the cylinder at the pressure measurement position.

The spanwise offset of the split-film sensor from the tunnel centerline was a trade-off between probe interference effects and spanwise effects. The spanwise effects consisted of three-dimensional cylinder shedding and the effects of the sidewalls on the flow. Inserting the probe directly upstream of the pressure tap would ensure the velocity is phase-locked with the cylinder phase directly downstream, but the probe would interfere with the cylinder shedding. Moving the probe spanwise would eliminate the probe interference with the pressure tap, but the phase of the vortex shedding from the cylinder at the span loca-

tion directly downstream of the probe would not be known. For this reason, the 1/4 inch spanwise spacing for the insertion point was chosen.

The advantage of inserting the probe from the top of the tunnel was realized through the use of a traverse located just outside of the test section. The split-film probe was attached to the traverse, which allowed the probe to be placed accurately at various heights (y-direction) in the test section while the tunnel was running and without the need for any additional insertion points. Any three-dimensional effects of the cylinder shedding could not be checked because only one spanwise location could be used to acquire data. The three-dimensional effects are expected to influence the upstream unsteady velocities. As mentioned in Section 2.1, the Gaussian distribution of the vortex shedding phase along the cylinder span will cause a reduction in the amplitudes of the unsteady velocities. Additionally, constructive and destructive interference of the propagating waves can alter the velocity amplitudes at different spanwise points.

Data acquisition hardware. A diagram of the data acquisition system is shown in Fig. 2.3. This system provided measurements of the stagnation temperature, unsteady pressure over the cylinder, and two-component velocity at a point in the flow.

Split-film velocity sensors. The TSI model 1287 split-film probe [37], a boundary layer probe, was chosen because the geometry allowed the probe to be inserted into the top of the tunnel and measure the freestream velocity. The boundary layer probe allowed the film to be placed in the tunnel such that the probe supports were not located between the sensing film and the cylinder.

Two Dantec model 90C10 constant temperature anemometry (CTA) modules [38] controlled the split-film sensor and provided amplification, low-pass filtering, and an offset to the voltages from the split-film probe. These modules were controlled using a Model 90N10 frame [38] that used an external temperature probe to provide an ambient temperature reference required for the thermal correction of the split-film sensor.

The entire system was controlled using Streamware [38], a Dantec software package designed to control CTA sensors. Due to the difficulty of incorporating a hardware trigger

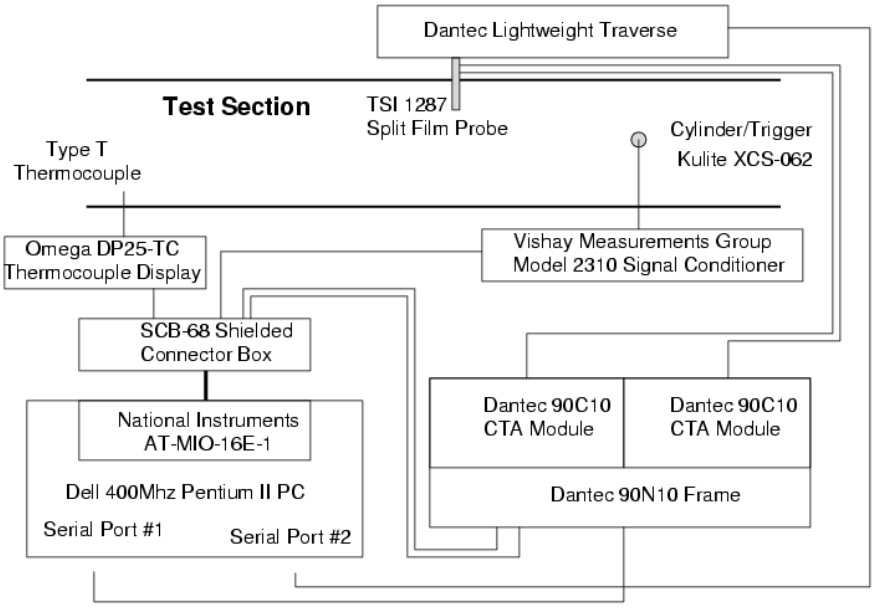

Figure 2.3 Single Cylinder Data Acquisition Hardware

required to lock the data collection with the cylinder pressure peaks, Streamware was unable to be used for the data collection. Instead, Streamware was used solely to control the split-film and provide signal conditioning.

Unsteady pressures. The data collection was triggered using the unsteady pressures on the cylinder surface through the use of an ultraminiature Kulite XCS-062 [39] differential pressure transducer The frequency response of the Kulite transducer was 300 kHz. The transducer was physically placed inside the cylinder through a hole drilled axially through the cylinder. The pressure was measured through a small hole drilled in the surface of the cylinder, perpendicular to the span of the cylinder. The cylinder was mounted in the test section in such a way that the pressure measurement hole was located on the top of the cylinder, perpendicular to the freestream flow; allowing an accurate indication of vortex shedding phase to be determined as used by Fabian [13] and Hopper [28]. The phase of the vortex shedding could be determined by fitting the measured unsteady pressure from the cylinder to a sine wave and determining the shift in the phase produced by the curve fit. This process will be further explained in Sections 2.3 and 2.4.

The pressure transducer was controlled using a Model 2310 [40] signal conditioner manufactured by Vishay Measurements Group Incorporated. This signal conditioner was used for excitation, amplification, and 10 kHz low-pass filtering of the pressure signal while only passing the unsteady portion of the signal. The unsteady portion of the pressure signal was used because Hopper [28] noticed that the mean signal for the pressure transducer tended to vary with time. Since only the unsteady pressure caused by the cylinder vortex shedding was desired, the unsteady portion of the signal was sufficient for this research.

Thermocouple measurements. All temperature measurements required for this research were obtained using Type-T thermocouples. An Omega DP25-TC [41] thermocouple meter was used to display the temperatures. The DP25-TC provided a cold junction offset which provided a $0^{\circ}C$ ($32^{\circ}F$) reference for the readings. An analog voltage output was provided from the thermocouple meter, with a resolution of 0-10 volts with $20^{\circ}F$/volt output. The accuracy of the readings was $\pm 0.9^{\circ}F$. The tunnel temperature values ranging from ambient conditions ($\sim 70^{\circ}F$) up through $130^{\circ}F$ were well within the Type-T thermocouple operational range of -$454^{\circ}F$ through $752^{\circ}F$.

A thermocouple placed in the stagnation chamber, downstream of the plug, was used to measure the temperature of the flow. In this region, the flow was approximately 10 ft/s, allowing for the assumption that the measured recovery temperature is the stagnation temperature of the flow.

The average temperature from the stagnation chamber was calculated for each measurement location. This average temperature was then used in the velocity calculation from the split-film measurements.

Data acquisition system. The analog voltage outputs from the CTA sensors, the pressure voltage from the Model 2310 signal conditioner, and the voltage from the thermocouple located in the stagnation chamber of the tunnel were collected by a National Instruments SCB-68 shielded connector box [42]. This box was configured to accept up to seven channels of data and had an additional channel for use as a hardware trigger. The

pressure voltage signal was connected to both an analog channel input and the hardware trigger point.

The voltages passed to the SCB-68 were then read by a National Instruments AT-MIO-16E-1 [42] sequential sampling board, located within a Dell 400 MHz personal computer, which is capable of reading up to 8 differential channels at a total sampling rate of 1.25 MHz. The data acquisition board provided 12-bit resolution with a minimum resolution of 4.88 mV.

Data acquisition was controlled through the use of National Instruments Lab View Version 5.0 [42]. Automation allowed all of the voltages required for a point in the flow to be collected with a single operation and included logic to ensure that each accepted sample contained a peak at the center of the pressure trace, as explained in Section 2.3.

CTA calibration system. The split-film anemometers were calibrated using a slightly modified TSI model 1125 calibrator [37]. The only modification to the calibrator was made by replacing the probe support with a probe support from a different TSI calibrator that provided better stability for the probe.

Pressurized air, available at a maximum of 100 psig, was used in the calibrator. A pressure transducer was located in the settling chamber and was used to monitor the airflow. A chart supplied in the calibrator manual provided a correlation of pressure settings to velocity for a range from 2.5 to 300 m/s. Software was developed to generate a curve fit to this routine using the Cubic Spline procedure found in Burden [43]. The use of this software, in addition to the digital pressure readout, allowed the calibration to be performed accurately in small velocity increments.

The temperature of the air entering the calibrator could be heated using a 220 volt heater, which was located just outside of the calibrator unit and controlled using a feedback-controlled thermostat. The temperature was set to match the temperature of the tunnel flow at maximum blower speed. The set-up required approximately 45 minutes for the temperature in the calibrator to stabilize.

The probe holder added to the model 1125 calibrator allowed the probe to be securely held such that the sensor was just above the exit jet. The only disadvantage was the off-

axis angle calibration because the probe angle could only be set in six-degree increments and negative angles below 6 degrees were not possible because the probe support would touch the nozzle of the calibrator.

The first step in the experimental process was to calibrate the probe by establishing the curve fit parameters unique to the specific probe. The process used for this calibration was modified from the process described by Fisk [44].

The initial step in the calibration process, described in TSI TB 20 [45], is to determine a value for the overheat ratios where the ratio of the voltages of the two CTA channels is constant with velocity for a flow along the probe axis. The voltage ratio should be roughly constant for the entire range of velocities being calibrated.

The magnitude of the velocity can be calculated by

$$E_1^2 + k^2 E_2^2 = (C_{vel} + D_{vel}\vec{V}^{n_{vel}})\Delta T \tag{2.5}$$

where $\vec{V}$ is the magnitude of the velocity, E_1 and E_2 are the voltages from each channel of the split-film sensor, k is the calibration ratio of E_1 and E_2, ΔT is the difference in temperature from the sensor surface and the freestream recovery temperature, and C_{vel} , D_{vel} , and n_{vel} are all calibration constants calculated through the calibration process.

The angle of the flow with respect to the sensor axis is calculated using

$$E_1^2 - k^2 E_2^2 = C_{angle}\left(E_1^2 + k^2 E_2^2\right)^{D_{angle}} \sin\alpha \tag{2.6}$$

where C_{angle} and D_{angle} are calibration constants. A more detailed description of the calibration process can be found in Appendix A.

2.3 Data Collection Set-up

Upon completion of calibration of the split-film sensors, the probe was mounted on the traverse and inserted into the test section. The sensor was lowered into the flow through the hole in the top wall of the test section.

Phase-locking the results. The velocity measurements acquired in the experiments were desired to be phase-locked with the cylinder shedding. The advantages of this were twofold: (1) velocities measured at different points in the flow at different times could be directly compared and (2) noise present in the velocity readings could be reduced through the use of ensemble averaging. Phase-locking was performed by capturing each sample with the data acquisition trigger capturing equal vortex shedding phase. The vortex shedding phase directly corresponded to the unsteady pressure measured at the top of the cylinder, so the unsteady peak pressure was used for phase-locking.

The phase-locking of the data acquisition was obtained through the use of a hardware trigger attached to the cylinder pressure transducer. The voltage required to trigger data collection was set to a value near the peak voltages seen in the pressure trace for the given conditions. The data acquisition board allowed the trigger point to be located anywhere in the 128 time step sample size. The trigger point was chosen to be located at the center of the sample, in keeping with the work by Hopper [28] and Fabian [13]. The choice of the location of the trigger point in the sample is arbitrary and will only effect the calculated phase of the cylinder shedding when the curve-fit is performed. The phase difference between the cylinder shedding and the measured unsteady velocities in the flow will not be changed.

A procedure was required to ensure that a peak of the pressure signal was obtained through use of the trigger. A Lab View procedure was written to automate this process by examining the pressure voltages from five time steps centered around the trigger point and ensuring that the trigger voltage was the peak and the voltage is reduced at each point away from the trigger. The pressures one time step before and after the trigger point were compared to the pressure at the trigger time. If the pressure at the trigger was smaller than either of these points, then the sample was rejected. If the pressure at the trigger time was larger, then the pressure measured at two time steps before and after the trigger time were compared to the pressure at one time step before and after, respectively. If pressure from one time step before the trigger point was smaller than the pressure from two time steps before the trigger point, the sample was rejected. Additionally, if the pressure from one time step after the trigger point was smaller than the pressure from two time steps

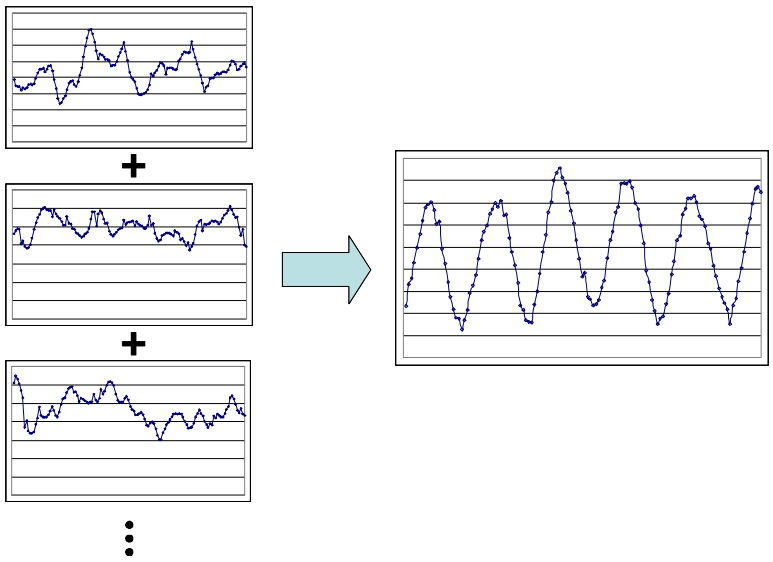

Figure 2.4 Use of Ensemble Averaging to Reveal Unsteady Velocity Fluctuations at the Cylinder Vortex Shedding Frequency

after the trigger point, the sample was rejected. This process ensured a pressure peak at the center of the trace with at least two points lower on each side of the trigger.

Ensemble averaging. The noise present in the phase-locked velocity measurements could be reduced using ensemble averaging, allowing fluctuations less than 0.5% of the mean flow to be measured. For ensemble averaging, each of the 128 sequential points for each channel are summed with corresponding points in successive samples and the sum is divided by the total number of samples.

An example of the importance of ensemble averaging is shown in Fig. 2.4. The measured voltages from one of the probe wires are shown for three different samples, and minimal amplitudes of the fluctuations at the cylinder frequency can be visibly seen in the signal. When each of the sets are averaged together, the resulting signal contains oscillations at the shedding frequency.

Ensemble averaging ensures that only the cylinder shedding causes the fluctuations present in the reduced data. Any other influences (i.e., tunnel vibrations) will be greatly reduced because the fluctuations will be random with respect to the cylinder shedding. The

ensemble averaging of the velocity voltages reduced the noise sufficiently and no additional filtering was necessary.

2.4 Data Reduction

The data acquisition speed was determined from the shedding frequency of the cylinder, calculated by Eq. (2.3). Because the buffer size restricted a sample size to be 128 time steps, a trade-off was made between the desire to achieve as many periods of oscillation as possible in a single set with the desire to have as many points as possible per oscillation to resolve the sinusoidal velocity fluctuations. The minimum frequency required to resolve a sinusoidal wave is over two times the sinusoidal frequency [46]. It was decided to obtain just over five oscillations per file, thus allowing over twenty time steps per oscillation. This was chosen because over ten time steps would be present per oscillation at the highest frequency desired in the flow, allowing resolution of the harmonic frequency signal when the results were curve-fit. For the cylinder vortex shedding at 5.25 kHz, the data collection frequency was chosen to be 120 kHz.

Each file acquired by the data acquisition process consisted of 250 samples. Each sample consists of one temperature voltage, and three data voltages acquired at 128 sequential time steps. The data voltages were either two velocities and a pressure signal or three pressure signals, depending on the set-up.

The first process for data reduction was ensemble averaging each file. Upon completion of ensemble averaging, the temperature voltages over the 128 sequential points were averaged to produce a single temperature for use in the temperature corrections in the data reduction equations. The time dependent velocity components and pressure voltages were written to a file, allowing velocity and pressure traces to be examined.

The final step was to curve-fit the pressure and velocity equations. Work performed previously by Hopper [28] and Fabian [13] showed the expected form of the results. Because the pressure trace was formed by the vortex shedding from a cylinder, the expected result is purely sinusoidal at the cylinder shedding frequency. The unsteady pressure can be fit

to

$$\tilde{P} = A_{pp} \sin\left(\omega t + \phi_{pp}\right) \tag{2.7}$$

where A_{pp} is the amplitude of the oscillations, ω is the vortex shedding frequency in radians, and ϕ_{pp} is the phase.

Once the shedding frequency of the cylinder was calculated, the velocity curve-fitting was performed using the frequency of the cylinder pressure as the velocity frequency. Previous experimental results by Fabian [13] and Hopper [28], and this current work have demonstrated that the frequencies present in the ensemble averaged unsteady velocity are only the cylinder shedding frequency and the first harmonic of the cylinder shedding [23]. The velocity components can be expressed as

$$\begin{aligned} u &= \bar{u} + A_{up} \sin\left(\omega t + \phi_{up}\right) + A_{uh} \sin\left(2\omega t + \phi_{uh}\right) \\ v &= \bar{v} + A_{vp} \sin\left(\omega t + \phi_{vp}\right) + A_{vh} \sin\left(2\omega t + \phi_{vh}\right) \end{aligned} \tag{2.8}$$

where $\bar{u}$ and $\bar{v}$ are the mean velocity components, ω is the cylinder shedding frequency, 2ω is the harmonic of the cylinder shedding frequency, A is the amplitude for the primary or harmonic frequency for each component, and ϕ is the phase shift for the two frequencies for each component. The unknown quantities in Eq. (2.8) are the mean of each component of the velocity ($\bar{u}$ and $\bar{v}$), the amplitudes of the primary frequency and first harmonic fits, and the phase shifts of both the primary and first harmonic fits. Typical values of A_{up} and A_{vp} were less than 1% of the mean freestream velocity. The harmonic amplitudes (A_{uh} and A_{vh}) were typically less than 0.05% of the mean freestream velocity.

The sinusoidal curve-fitting for both the pressure and the velocity curve-fits was performed using a non-linear regression routine seen in Appendix B. This routine uses an iterative method of altering guesses for the mean, amplitudes, and phase shifts until the new value of each parameter is within a specified error tolerance of the pervious iteration. For Eqs. (2.7) and (2.8), the routine provides for convergence for almost every file.

The final portion of the data reduction software was to output the results from the curve-fitting to a file that consists of a single entry for each input file that included the

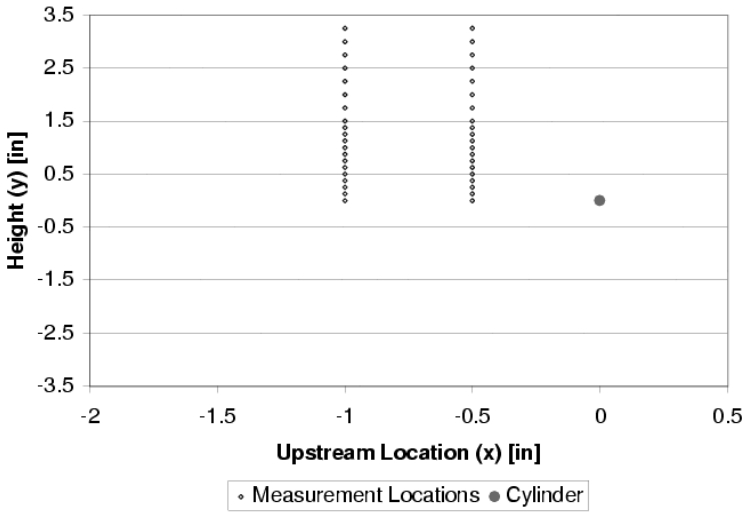

Figure 2.5 Measurement Locations for Single Cylinder Set-up

input filename, the values for each of the curve-fit parameters, a value of root mean square (rms) error for each channel for the ensemble averaging, and finally an rms error for each curve-fit. This file can be imported for plotting and further analysis.

The processing was designed to be as automated as possible, allowing for the user to select any number of files to be reduced and the results to be placed in a single output file. Additional information for the data reduction software can be found in Appendix C.

2.5 Results

The tunnel was run at 110 m/s and 125 m/s, with the cylinder at the centerline of the test section. The height (y-direction) of the split-film sensor was translated from the tunnel centerline through 3 1/4 inches above the centerline for two different upstream locations, 1/2 and one inch, as seen in Fig. 2.5.

Typical results. An example of a typical x-velocity and pressure trace of 128 points is shown in Fig. 2.6. This trace was taken from the data collected with the probe located at 1/2 inch upstream and 1/4 inch above the cylinder. As can be seen, the sinusoidal nature of the cylinder shedding is present in the pressure trace, but is not as clear in the velocity trace. The sinusoidal signal present in the velocity can be extracted through the

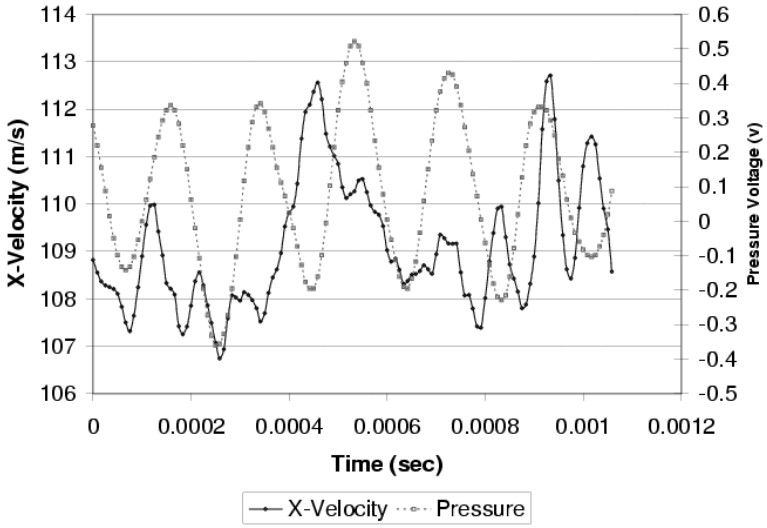

Figure 2.6 Single Trace with Probe 1/2 inch Upstream and 1/4 inch Above Centerline

use of ensemble averaging. The peak to peak variations in the pressure signal in Fig. 2.6 is typical for cylinder shedding at a cylinder Reynolds number of 39,000 [32].

As can be seen in Fig. 2.7, the ensemble averaged pressure voltage is similar to the single pressure voltage trace shown in Fig. 2.6. Although the amplitude is larger for the ensemble averaged pressure voltage, the phase of the sinusoidal signal is the same between the single trace and the ensemble averaged result.

The benefits of ensemble averaging the results can be seen by comparing the x-velocity trace from Fig. 2.6 with the ensemble averaged x-velocity, as shown in Fig. 2.8. The ensemble averaged velocity contains a strong sinusoidal component although it cannot be seen in the single velocity trace.

The velocities captured in the single trace contained noise that caused the peak velocity readings to be larger than those of the ensemble averaged case. Through ensemble averaging the high peak noise readings were reduced or eliminated, leaving only the sinusoidal fluctuations caused by the cylinder.

Curve-fitting of the unsteady velocities allowed results taken at various points in the flow to be compared. The results of curve-fitting the pressure data for the ensemble pressure voltage data, shown in Fig. 2.7, can be seen in Fig. 2.9, where the points are

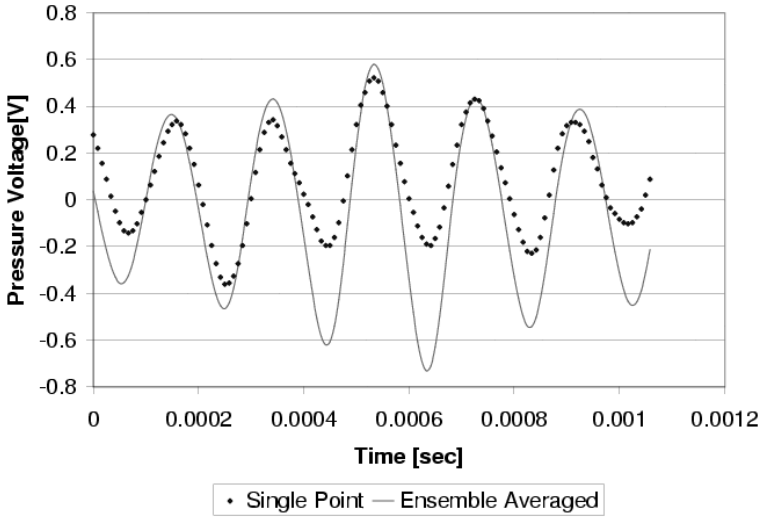

Figure 2.7 Pressure Voltage Trace For Cylinder in Freestream Flow

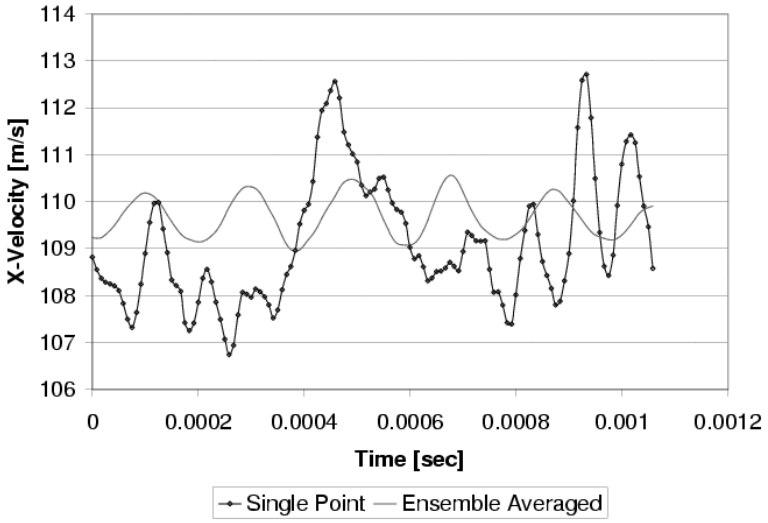

Figure 2.8 X-Velocity Trace at 1/2 inch Upstream and 1/4 inch Above Cylinder

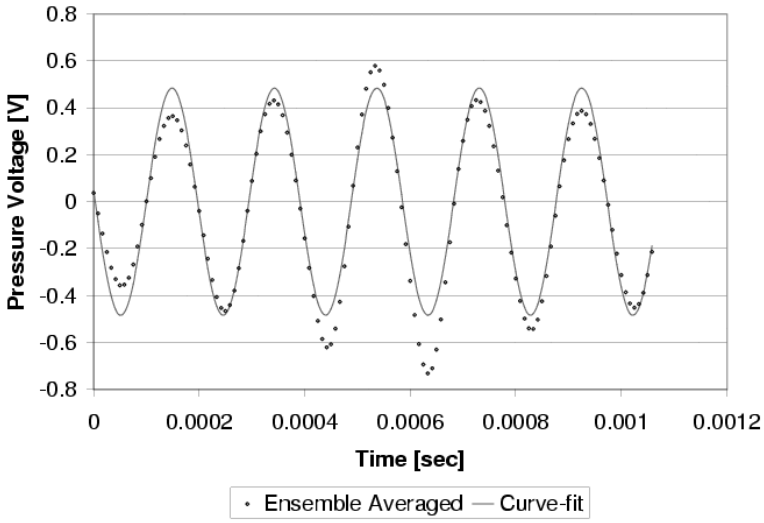

Figure 2.9 Pressure Voltage Curve-fit For Cylinder in Freestream Flow

the ensemble averaged pressure voltages and the line is the curve-fit. As can be seen, the curve-fit consisting of only the sinusoidal term at the cylinder shedding frequency provides an accurate description of the ensemble averaged data.

The curve-fit of the x-velocity results was performed using Eq. (2.8). A comparison of the velocity fit with the ensemble averaged velocities is shown in Fig. 2.10. Like the fit shown in Fig. 2.9, the velocity curve fit provides an accurate description of the ensemble averaged data.

The fit of the velocity shown in Fig. 2.10 allowed the data to be accurately described through the use of the velocity magnitude, cylinder shedding frequency, and the primary and harmonic frequency amplitudes and phase shifts. Although the first harmonic of the shedding frequency was used in the curve fit, the results are neglected because the harmonic amplitude is small in comparison to the amplitude of the primary frequency fit.

Velocity amplitude results. The amplitude of the velocity can be used to determine the effects of location on the unsteady fluctuations caused by the cylinder shedding. The velocity was measured at 13 different height locations at two different distances upstream for a freestream velocity of 125 m/s. A plot of the amplitudes of the x-velocity fluctuations, A_{up}, are shown in Fig. 2.11. As expected from the results by Hopper [28], the unsteady

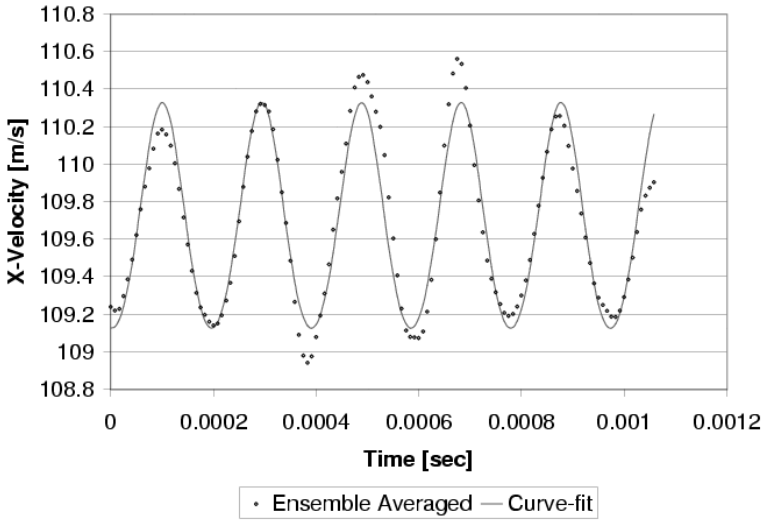

Figure 2.10 X-Velocity Curve-fit for 1/2 inch Upstream and 1/4 inch Above Cylinder

velocity amplitude is maximum above the centerline of the tunnel and falls off as a function of the height above the centerline, due to the increasing radius from the cylinder.

The unsteady x-velocity amplitudes show a dependence on both the height above the cylinder and the distance upstream. If the unsteady fluctuations were truly potential in nature, the amplitude of the unsteady fluctuations from the circulation around the cylinder should be reduced as a function of 1/r from the cylinder centerline. The amplitude for the unsteady velocity at the point one inch upstream of the cylinder and 1/4 inch above the centerline is expected to be 0.32 m/s when calculated from the unsteady velocity 1/2 inch upstream of the point. The measured velocity, however, is 0.414 m/s, or 27% larger than expected. The amplitudes of the unsteady oscillations do not follow the true potential flow theory

The unsteady velocities generated by the forcing are reduced with upstream distance slower than predicted by potential theory, in agreement with work by both Falk [27] and Hopper [28]. Although only two upstream distances were used for this work, the work by Hopper found the slow reduction in unsteady amplitudes for five upstream distances ranging from one to two inches. The benefits of increasing spacing between the sinusoidal forcing (i.e., cylinders or blades) and the upstream blades, in order to reduce the unsteady

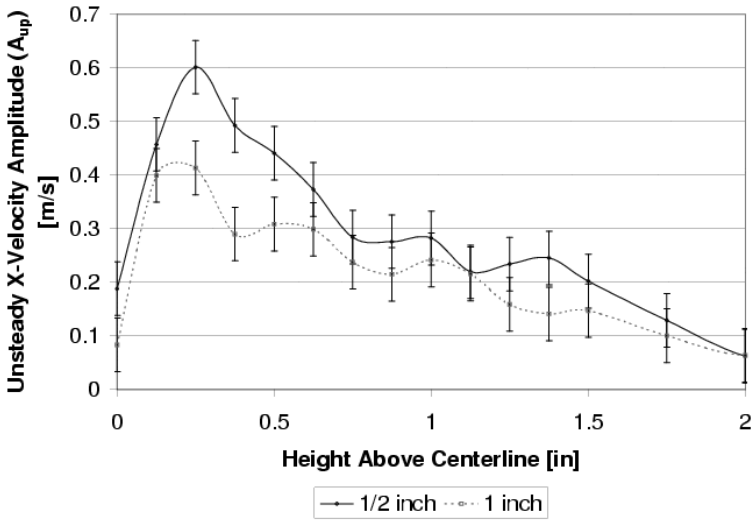

Figure 2.11 X-Velocity Unsteady Amplitude Upstream of a Single Cylinder

amplitudes, are not as large as potential theory would predict. Either the spacing must be increased even farther or the unsteady amplitudes must be accepted.

Estimation of the error. The two types of errors examined for this work were the errors caused by repeatability of the results and the error on the curve-fit parameters. The repeatability errors were caused because the flow was highly fluctuating. The cure-fit parameter errors were caused by the parameters used in Eq. (2.8) not completely describing the ensemble averaged flow.

The errors of the repeatability of the results were calculated to be ± 0.05 m/s and are shown as the error bars in Fig. 2.11. This error of the unsteady amplitudes was estimated by performing multiple ensemble averages using only 50 time traces. A total of 25 sets of ensemble averaged time traces were examined. The first 5 sets were taken sequentually from the file and the remaining 20 were created using a random sample of time traces.

The resulting ensemble averaged velocities for each of the 50 time traces were curve-fit to Eqs. (2.7) and (2.8). The deviation of the resulting amplitudes, calculated from the 25 sets of amplitudes using the biased estimate of the standard deviation, is defined as

$$\sigma = \sqrt{\frac{\sum \left(A_{up} - \bar{A}_{up}\right)^2}{N-1}} \tag{2.9}$$

where N is the number of samples (25 in this case). The calculated deviation of the results was ± 0.05 m/s. This was used as the estimated error in Fig. 2.11.

The curve-fit parameter errors were calculated through the use of TableCurve 2D, version 5.0. The standard error of the amplitude fit for each of the points ranged from 0.005 to 0.007 m/s. The curve-fit parameter errors were an order of magnitude less than the repeatability errors.

Errors From the Influence of Unsteady Cylinder Shedding. As mentioned previously, the amplitudes of vortex shedding of a cylinder at Reynolds numbers around 39,000 is highly irregular [32]. The method of data collection used for this work, by Hopper [28], and also by Fabian and Jumper [23, 24], involved using a trigger to capture data when the pressure voltage was above a certain level. The data reduction process ensured that the pressure voltage used for the trigger was located in a peak in the pressure. Any samples where the trigger voltage was not at the peak were rejected. This process provided two benefits for the data collection process. First, it ensured that the trigger point existed at a peak,simplifying the ensemble averaging process because each of the samples were guaranteed to be in phase. Second, the resulting unsteady velocities measured in the field are produced for equivalent vortex shedding strength.

The measured velocities do not necessarily give an accurate representation of the unsteady velocity field present for all time. The frequency of the fluctuations present in the field should remain roughly constant because the cylinder does shed vortices at a constant frequency; however, the magnitude of the fluctuations present in the field will vary over time. The velocities shown in Fig. 2.11 were for a fixed amplitude of pressure fluctuations from the cylinder. The true unsteady amplitude of points in the flow will vary with the varying amplitude of the pressure fluctuations.

The variability in the unsteady amplitude of the velocity fluctuations was not important for this work. The velocity field measured throughout the work at varying points was desired to be compared to other points in the flow under the same conditions. The process used for this work ensured that each of the results corresponded to a constant pressure peak, and thus vortex shedding strength.

Upstream Propagation of Unsteady Waves. The upstream propagation of the unsteady waves produced by the cylinder can be seen by an analysis of the phase shift of the unsteady velocities. For compressible flow, any potential-like disturbances propagate at acoustic speed through the flow. The acoustic speed is defined as the speed of sound modified by the flow velocity. Any waves propagating directly into the flow will propagate at a true speed of $(a - U_\infty)$ where a is the speed of sound. The general form of the phase shift required for acoustic upstream propagation, from Hopper [28], is

$$\phi_{shift} = \phi_{ref} + \frac{r\omega}{a\sqrt{1 + 2M\cos\theta + M^2}} \tag{2.10}$$

where M is the freestream Mach number, r is the radial distance from the cylinder to the desired point, and θ is the angle of r with respect to the freestream velocity. The term in the denominator of Eq. (2.10) is the acoustic speed of the potential-like wave, determined by the vector sum of the wave velocity and the freestream velocity, and ϕ_{ref} is a reference phase shift.

The phase shift calculated for ϕ_{up} is compared to the phase shift calculated from Eq. (2.10) for an upstream distance of 1/2 inch in Fig. 2.12. As can be seen, the phase calculated from the model predicts the delay in the phase as the radial distance is increased (by increasing y). A single value for ϕ_{shift} for the model was chosen to provide the best match of the model and was used throughout the model calculations.

The phase shift for a distance of one inch upstream is shown in Fig. 2.13. The value for ϕ_{shift} used for this calculation was the value used in the generation of Fig. 2.12. As can be seen, the phase reduction with tunnel height (y-direction) is matched by the model.

The model of the phase from an acoustically propagating wave agreed with the experimental results for both upstream distances. It can be concluded that the unsteady velocity waves are propagating upstream at acoustic speeds, a result in agreement with the work by Fabian [24].

Comparison to a simple potential flow model. A simple potential flow model was developed to explain the unsteady velocities present in the flow. From Fabian and Jumper

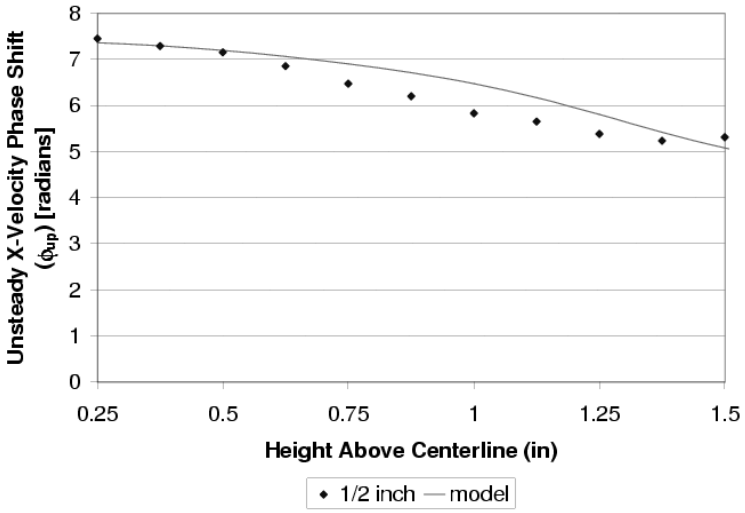

Figure 2.12 Unsteady X-Velocity Phase for 1/2 inch Upstream of a Single Cylinder

[24] and further work by Hopper [28], the unsteady velocity amplitude, in cylindrical coordinates, was estimated by

$$A_{\theta p} = \frac{|\,\Gamma\,|}{2\pi r\sqrt{\frac{\cos^2\theta}{1-M^2}+\sin^2\theta}} \tag{2.11}$$

where Γ is the circulation around the cylinder. The unsteady x- and y-velocity amplitudes (A_{up} and A_{vp}) can be found by a coordinate transform from cylindrical coordinates

The results shown in Fig. 2.11 were compared to results obtained from Eq. (2.11). The value for the cylinder circulation, Γ from Eq. (2.11), was determined by minimizing the rms error between the predicted amplitude from Eq. 2.11 and the experimental results for an upstream distance of 1/2 inch.

The comparison of the model with the experimental results for 1/2 inch upstream is shown in Fig. 2.14. The model does not accurately predict either the values or the trend of the unsteady amplitudes with height above the cylinder. The model does predict a decline in the amplitude with height; however, the reduction with height is not as steep as in the experimental data.

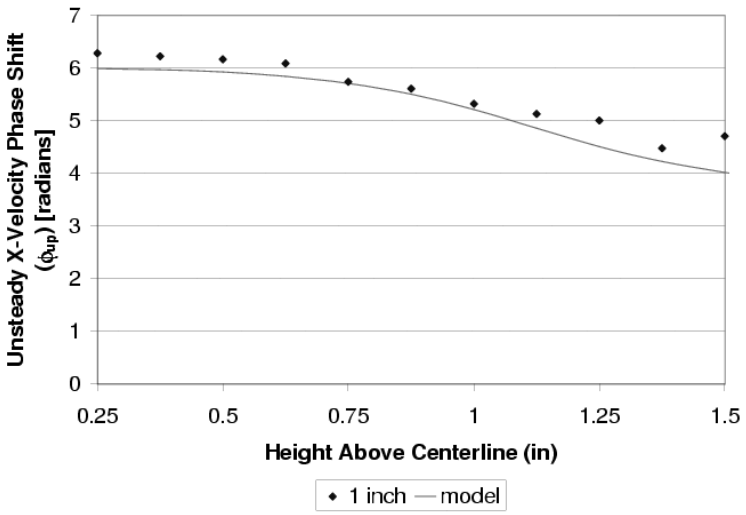

Figure 2.13 Unsteady X-Velocity Phase for 1 inch Upstream of a Single Cylinder

The model predicts that the unsteady x-velocity amplitude would be eliminated at the centerline and would increase steeply as the height is increased until a maximum value is reached, which is seen in the experimental results. The fall-off with heights greater than the location of the maximum amplitude is not accurately predicted by the model. The height of the location of maximum amplitude is also not accurately predicted.

A comparison of the potential flow model described in Eq. 2.11 and experimental results for an upstream distance of one inch is shown in Fig. 2.15. As can be seen, the model performs very poorly in predicting the unsteady velocity data at this distance upstream.

The poor performance of the Fabian and Hopper suggested potential model is not surprising for this flow. The model does not take into account the presence of concentrated vorticity in the wake behind the cylinder that would influence the flow. Additionally, the model does not take into account any tunnel specific influences such as the side walls, possible pumping of the freestream velocity, and any acoustic effects. The model does incorporate influences of the top and bottom walls by adding a mirror image of the cylinder at 8 inches above and below the tunnel centerline.

CFD Results. A CFD simulation was performed for this work to gain increased knowledge of the flow upstream of a single cylinder. The unsteady flow was obtained

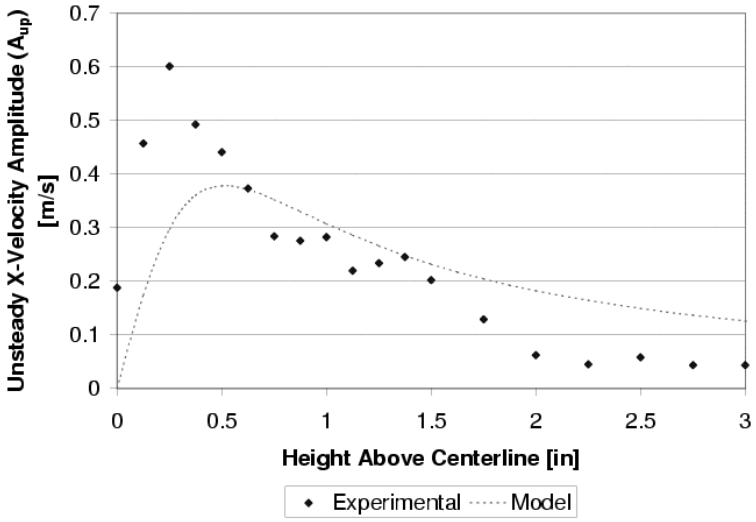

Figure 2.14 Failure of Simple Potential Model to Capture Unsteady X-Velocity Amplitudes 1/2 inch Upstream of a Cylinder

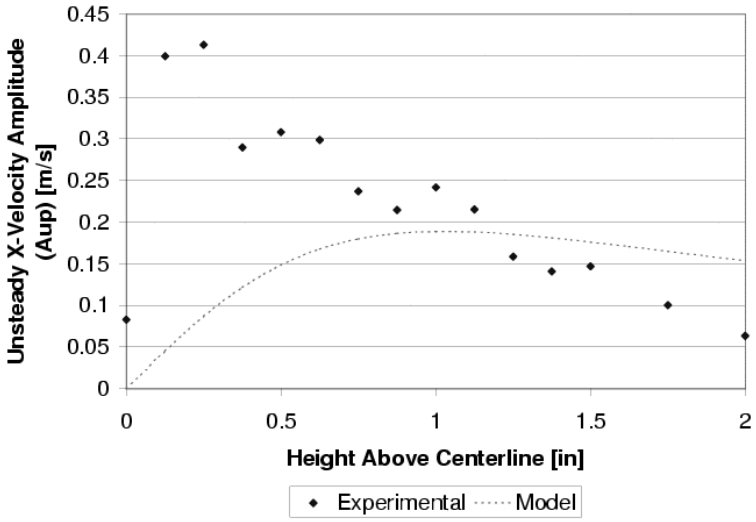

Figure 2.15 Failure of Simple Potential Model to Capture Unsteady X-Velocity Amplitudes One inch Upstream of a Cylinder

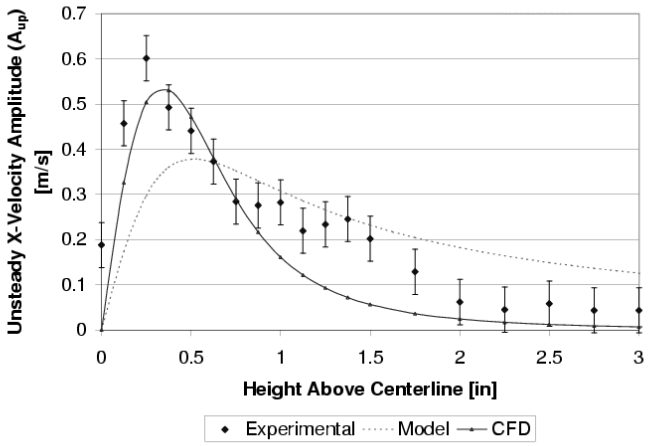

Figure 2.16 Failure of CFD to Predict Unsteady Unsteady X-Velocity Amplitudes 1/2 Inch Upstream of a Cylinder

using a laminar and incompressible flow model. A detailed description of the methods and results from the CFD analysis is shown in Appendix D. Like the potential model, the CFD results fail to accurately predict the flow, as seen in Fig. 2.16. This failure is caused by many factors including the lack of three-dimensional modeling, and any tunnel specific influences.

2.6 Summary

A single cylinder was placed in crossflow and the velocity upstream of the cylinder was measured. The oscillating circulation generated by the vortex shedding from the cylinder created fluctuations in the upstream flow at the shedding frequency of the cylinder. The decrease in unsteady oscillations with upstream distance was not as large as predicted by a simple potential theory, indicating that the upstream influences exist farther upstream than expected.

Neither the suggested simple potential flow model defined in Eq. 2.11 nor CFD were able to accurately predict the unsteady flow. Tunnel specific influences, in addition to the lack of randomness and three-dimensional effects were not present in either model. Through

the use of a model for an acoustically propagating potential-like wave, the unsteady velocity waves were shown to propagate upstream at acoustic speed.

III. Multi-Cylinder Array

The unsteady velocities upstream of a single cylinder were shown in the previous chapter. The unsteady flow upstream of an array of cylinders without the disturbances of blades was desired prior to inserting the cylinders into a cascade. This chapter examines the interaction of an array of cylinders placed in a freestream flow.

3.1 Previous Work on Interaction of Multiple Cylinders

Much research on the interaction of multiple cylinders placed in a uniform freestream flow has been performed [47, 19, 20, 21], but very little research has focused on Reynolds numbers, based on cylinder diameter, greater than 10,000. Ohya et al. [47] examined the effects of two cylinders located in the freestream for various Reynolds numbers, including this range. One of the key parameters of this study was the ratio of the distance between the centers of the cylinders (d) and the diameter of the cylinder (D). For Reynolds numbers in the range of 1.5×10^4 through 9.3×10^4 with the ratio $(d/D) > 2$, the frequency of the shedding from each cylinder is identical to that from an individual cylinder in the flow. For $(d/D) \leq 2$, the shedding frequency changed, indicating an interaction in the shedding between cylinders.

According to Ohya, for $\mathrm{Re} = 10^4$, the shedding of the pair of cylinders form independent vortex streets when (d/D) is large enough. At $(d/D) \approx 3.5$, the vortex streets begin to exhibit a dependence as each cylinder sheds vortices of opposite signs simultaneously, creating asynchronous shedding. This pattern existed down to a spacing of $(d/D) = 2$. Below this spacing, the shedding loses the symmetry and becomes biased toward one side. The creation of synchronous shedding was not obtained for $\mathrm{Re} = 10^4$ but was discovered for Reynolds numbers between 200 and 500.

The shedding of vortices of opposite signs at a given instant in time was also seen by Hamakwa, et al. [48]. In this work, an array of serrated-fin cylinders were placed with a spacing of 1.43 diameters between cylinders. The Reynolds number used in this work was $3.9x10^4$.

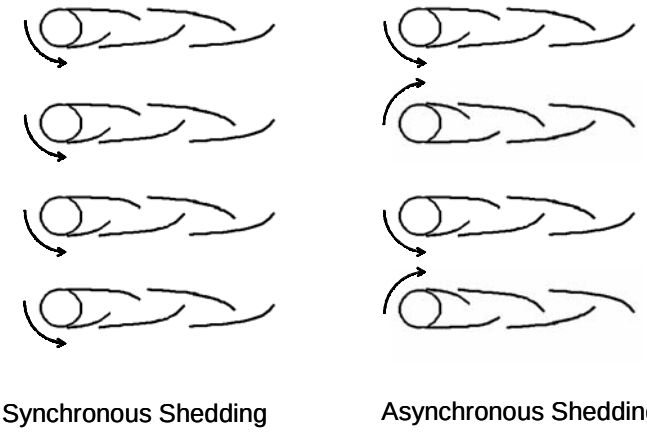

Figure 3.1 Coherent Cylinder Shedding Types (Repeated From Introduction)

3.2 Cylinder Array Coherence

The cylinder array is shedding in a coherent fashion when the phase of vortex shedding between any two cylinders is approximately constant. From the work of Ohya [47], the primary determining factor in the presence of coherence is the spacing between cylinders (normalized by the diameter). If the cylinders are not shedding in a coherent fashion, then the shedding from each cylinder is equivalent to that of a single cylinder and the vortex shedding relation between the cylinders is random with time.

Two types of coherent cylinder shedding have been found experimentally, synchronous and asynchronous, shown in Fig. 3.1. Synchronous shedding exists when a vortex is shed from the same side of each cylinder simultaneously. Asynchronous shedding is created when every other cylinder sheds a vortex from the same side simultaneously and from the opposite side for the remaining cylinders.

3.3 Experimental Set-up

The single cylinder test section discussed in Section 2.2 was modified to accommodate cylinders placed within an array perpendicular to the flow. The sliders that are used to hold the single cylinder were modified by drilling additional holes along the length to enable multiple cylinders to be inserted. A side view of the modified test section can be seen in Fig. 3.2.

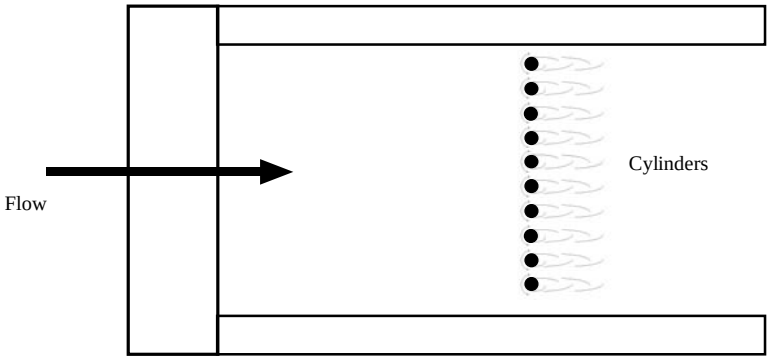

Figure 3.2 Ten Cylinder Test Section Configuration

Ten cylinders were placed in the flow and had a 0.8 inch separation between centerlines, in keeping with the work by Fabian [13]. By choosing the 0.8 in separation, the cylinders were equally spaced within the test section and the top and bottom cylinders were 0.4 inches from the top and bottom walls, respectively. Potential flow theory predicts each of the cylinders will produce a virtual cylinder located outside of the tunnel walls. The 0.4 spacing ensured that the top (and bottom) cylinder was located 0.8 inches from its virtual cylinder.

For the cases of multiple cylinder runs, only three of the cylinders were instrumented with a Kulite pressure transducer [39], as seen in Fig. 3.3. Each of these three cylinders was controlled using a separate Model 2310 [40] signal conditioner. In order to obtain pressure readings at each of the possible cylinder locations, two of the instrumented cylinders were moved to various positions and the data was taken again using the same cylinder to trigger the data collection. This process allowed pressure readings from various data runs to be phase-locked.

3.4 Experimental Results

The phase, referenced to cylinder 5, for each of the 10 different cylinders at a given instant in time are shown in Fig. 3.4. As can be seen, no coherent shedding exists between the cylinders. At the two different times, the relative phase between the trigger cylinder (cylinder 5) and the other cylinders is different.

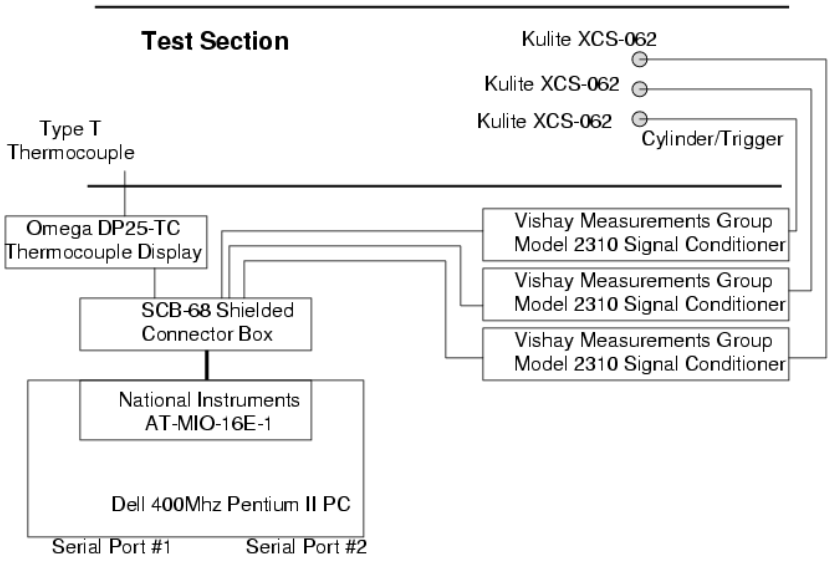

Figure 3.3 Data Acquisition System for 10 Cylinder Runs

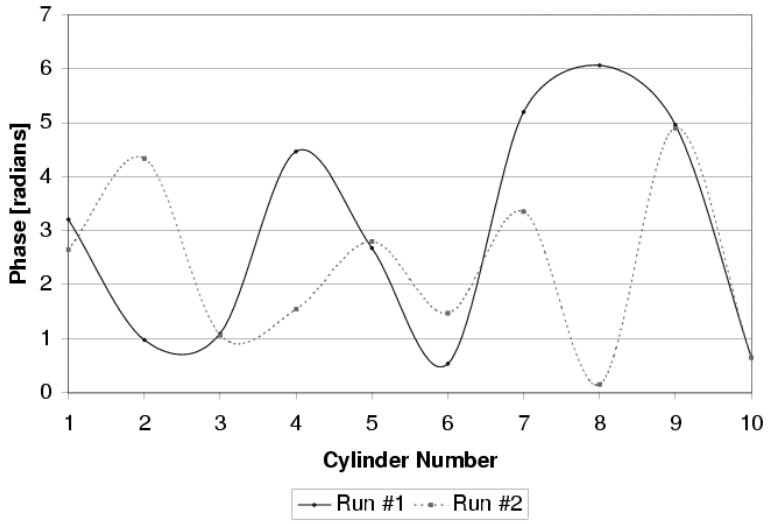

Figure 3.4 Instantaneous Cylinder Shedding Phase for 10 Cylinders at Two Times

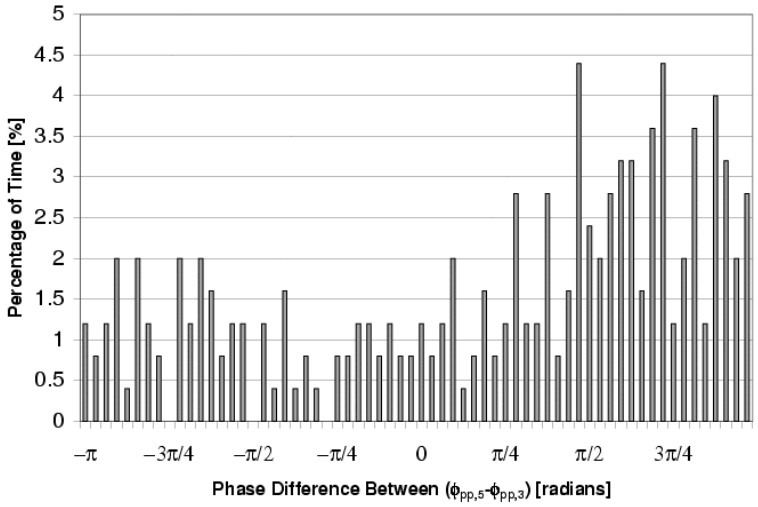

Figure 3.5 Phase Difference Histogram for Freestream Flow

The randomness of the relative cylinder shedding can be seen in the histogram of the relative shedding between the 4th and 5th cylinders, shown in Fig. 3.5. The relative shedding phases are fairly random because noticeable peaks are not present in Fig. 3.5. If coherent shedding were present for the flow shown in Fig. 3.5, a normal distribution with a fairly large peak would be seen in the phase difference.

Velocity effects. The velocity effects on the relative cylinder shedding for the freestream flow are shown in Fig. 3.6. This plot was created by calculating the standard deviation of the mean relative phase difference between the fourth and fifth cylinders $(\phi_{pp,5} - \phi_{pp,4})$. The standard deviation was calculated from Eq. (2.9). If the cylinders are shedding in a coherent fashion, the standard deviation should decrease. As can be seen, there is no trend present in the data, indicating that the velocity has no effect on the relative shedding for the freestream case.

3.5 Computational Results

An unsteady CFD solution was generated for the experimental set-up shown in Fig. 3.2 using Fluent Version 6.0 [49]. An incompressible and laminar model was used. The solution was generated using a time step of 2.0833×10^{-6} seconds, or 1/4 the time step used

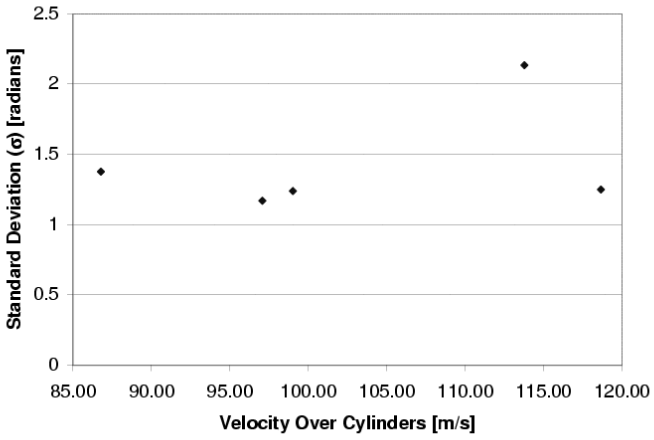

Figure 3.6 Effects of Velocity on Shedding Coherence in Freestream Flow

in the experimental data. A time step smaller than the experimental data acquisition time step was required for the solution to converge to a solution with the velocity and pressures oscillating with constant amplitudes. The process used for the computational solution was identical to the process used for the single cylinder and are further explained in Appendix D.

The flow was initialized to zero velocity throughout the test section. The flow was initiated by setting the inlet to a constant velocity and computing the solution. The flow time required for the oscillations to converge was 10,000 time steps, or approximately 0.021 seconds of flow time.

CFD was executed for flows containing 10 cylinders, with a 3/16 in diameter and a spacing of 0.8 inches between centers. This provided equal spacing between all cylinders and 1/2 spacing between the end cylinders and the endwall of the test section. This spacing was used in an effort to compare to the experimental results performed experimentally and also the results of Fabian [13].

The grid, shown in Fig. 3.7, was produced using the Elliptic-Laplace structured mesh option in the mesh generator add-on for TecPlot [50]. The grid was developed by dividing the flow field into 20 different regions, created by horizontal lines located through

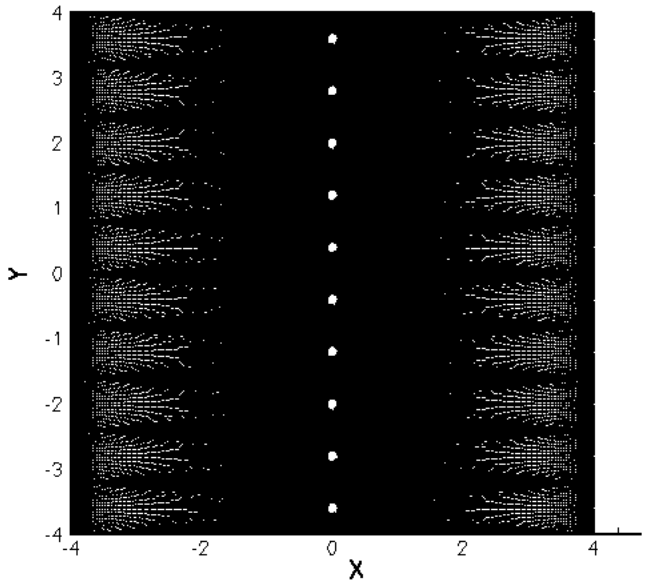

Figure 3.7 10 Cylinder Grid

each cylinder and at the midpoint between the cylinders. Grid spacing for each region was again established with 2-sided exponential spacing, allowing for point clustering along each cylinder and the walls. The method of using 20 different regions introduced very large inefficiencies in the grid point locations. Like the single cylinder grid, points are clustered around the inlet and outlet of the flow. Additionally, the region of the flow half-way between cylinders also has a grid spacing equivalent to the spacing at the walls. This inefficient set-up was used because a symmetric grid was desired in order to reduce any potential influences on the shedding based on grid spacing around the cylinders. Approximately 180,000 nodes were used for the flow.

The cylinders and the top and bottom tunnel walls were set as a wall boundary with zero normal velocity and no-slip tangential velocity. The outlet of the test section was established using the default outflow boundary condition available in Fluent. The inlet boundary was set to a constant velocity of 125 m/s.

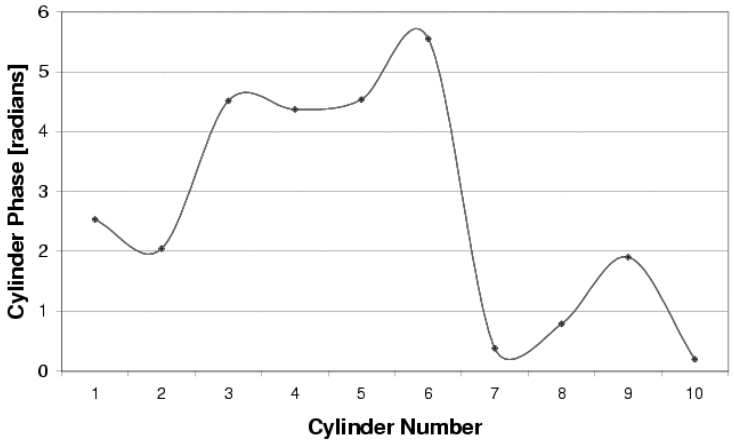

Figure 3.8 CFD Pressure Phase of Each Cylinder in Uniform Freestream

Uniform freestream. It was hoped that the shedding of the cylinders would behave in some coherent fashion. The sinusoidal pressure on the top of each cylinder was fit using

$$P = \bar{P} + A_{pp} \sin\left(\omega t + \phi_{pp}\right) + A_{ph} \sin\left(2\omega t + \phi_{ph}\right) \tag{3.1}$$

where A_{ph} and ϕ_{ph} are the pressure amplitudes and phase shift at the first harmonic frequency of the cylinder vortex shedding.

The results of the phase of the shedding of each cylinder are shown in Fig. 3.8. As can be seen, only three of the cylinders, 3-5, corresponding to +y locations, were shedding vortices in phase. The lower cylinders, 6-10, failed to shed in a coherent fashion. The out-of-phase shedding is caused by the chaotic nature of the initiation of vortex shedding from a cylinder. The results shown in Fig. 3.8 are repeatable solely due to the lack of randomness present in a CFD solution.

Computational results from two different points, chosen arbitrarily, upstream of the cylinders are shown in Figs. 3.9-3.11. For each of these plots, the x-location is kept constant at 2 inches upstream, and the y-location is either 1 or -1 inches from the tunnel centerline.

As seen in Fig. 3.9, the pressure fluctuations are almost identical for both of the points observed. The pressure fluctuations are composed primarily of a sine wave at the

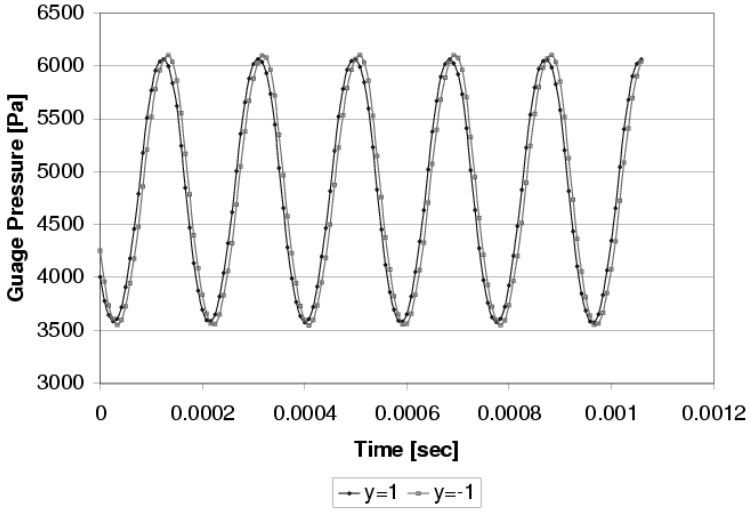

Figure 3.9 CFD Pressure Trace 2 Inches Upstream of Cylinder Array With Random Shedding

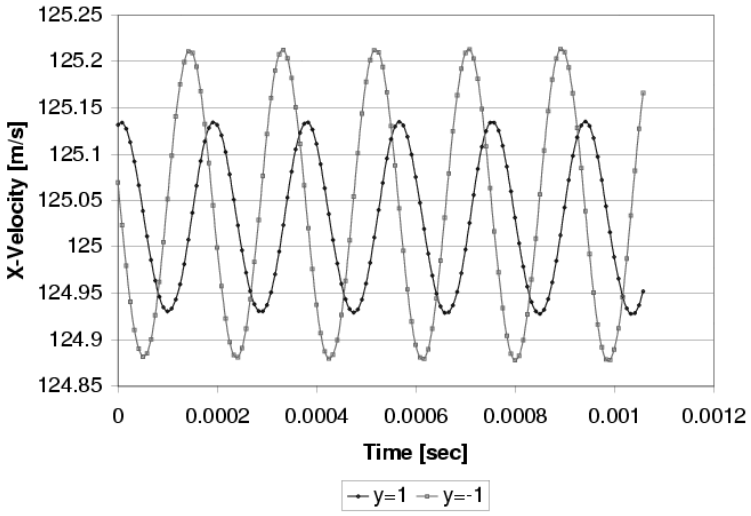

Figure 3.10 CFD X-Velocity Trace 2 Inches Upstream of Cylinder Array With Random Shedding

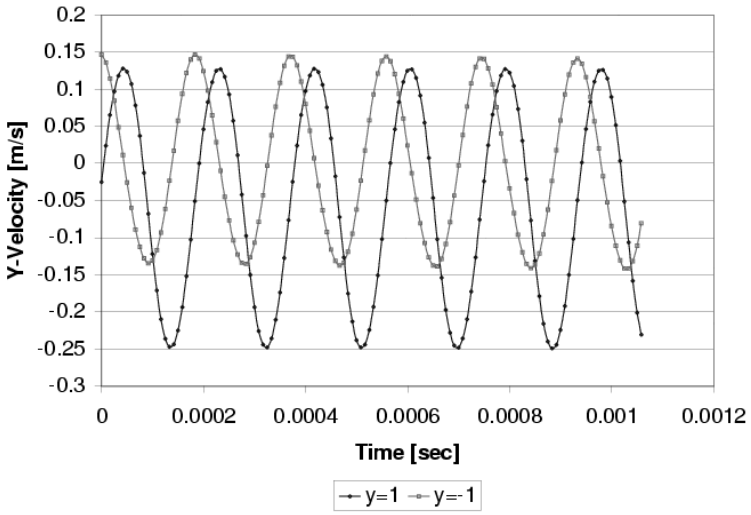

Figure 3.11 CFD Y-Velocity Trace 2 Inches Upstream of Cylinder Array With Random Shedding

cylinder shedding frequency with the first harmonic frequency comprising less than 5% of the fluctuations.

Differences in the velocity results between the two points can be seen in Figs. 3.10 and 3.11. For both the x-velocity and y-velocity, the average value, amplitude of the fluctuations, and the phase of the fluctuations were different for the two points analyzed. This difference is caused by the difference in the cylinder shedding phases shown in Fig. 3.8. The lack of coherence of the cylinder shedding causes the influences on the velocity fluctuations by each cylinder to be additive in certain regions and destructive in others, with no symmetry in the flow.

The flow at two locations upstream of the bank of cylinders is presented in Figs. 3.12 and 3.13. The y-velocity fluctuations are shown along with the phase shift in each of the plots. As seen in Fig. 3.12, for 1/2 inch upstream of the array of cylinders, the variation in amplitude of the fluctuations corresponds to cylinder spacing, with maximums on cylinder centerlines.

The peaks in the y-velocity fluctuation amplitudes are smoothed out farther upstream, as seen in Fig. 3.13. At a distance of three inches, each point is influenced by multiple cylinders, causing the shedding peaks to vanish. The amplitudes correspond-

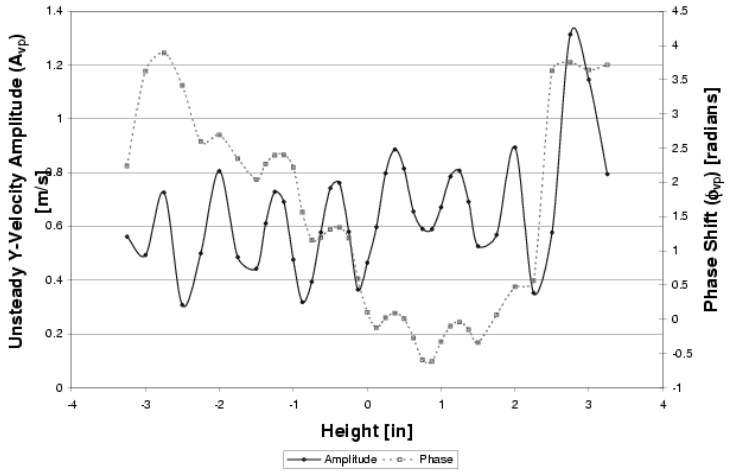

Figure 3.12 CFD Y-Velocity Amplitudes 1/2 Inch Upstream of Cylinder Array With Random Shedding

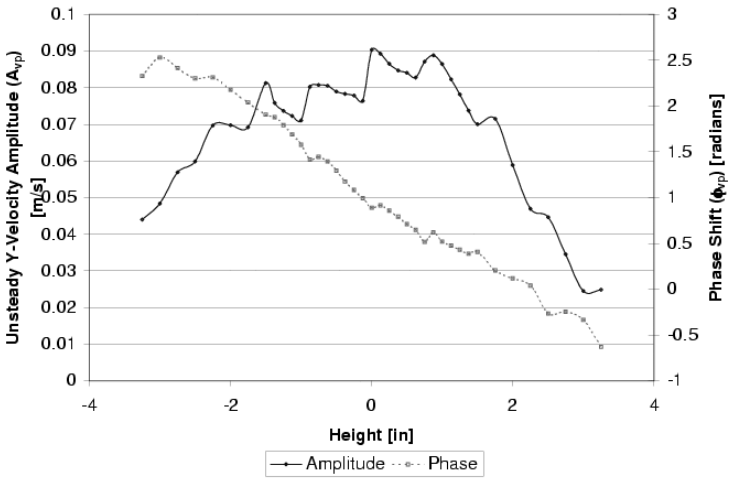

Figure 3.13 CFD Y-Velocity Amplitudes 3 Inches Upstream of Cylinder Array With Random Shedding

ing to locations above the test section centerline, cylinders 1-3 in particular, are reduced because the corresponding cylinders are not shedding in a synchronous or asynchronous manner. This random shedding causes the fluctuations in this region to be reduced by the other cylinders.

The randomness in the relative phases of the vortex shedding of each cylinder prevents the flow from being accurately predicted. The interference of vortex shedding from each of the cylinders creates a flow with higher unsteady velocities below the centerline of the tunnel (y-direction).

Upstream wake. An effort was made to force the cylinders to shed in a coherent fashion by modifying the inlet conditions. There are two possible relations between the cylinders which will provide coherent shedding: symmetric and asymmetric cylinder shedding. For the symmetric case, the vortex shedding phase for each cylinder is the same. The asymmetric shedding is created when the vortex shedding phase between consecutive cylinders is exactly π radians out of phase, forcing every other cylinder to be in phase.

The synchronization of the cylinders was created by dividing the inlet boundary into 20 different sections, creating 20 stream tubes. Either type of synchronization could be achieved by setting the different inlet sections to a velocity 15 m/s above or below the desired mean flow of 125 m/s in a fashion explained below.

The synchronous shedding was created by alternating high and low velocities between stream tubes, as seen in Fig. 3.14. For the 10 inlet sections just above each cylinder centerline, the inlet forcing velocity was set to 140 m/s. For the remaining sections, below each cylinder, the inlet velocity was set at 110 m/s. The resulting flow field contains velocity interfaces in front of each cylinder and also half-way between the cylinders. The velocity variation thus simulated a series of wakes from upstream airfoils.

The asynchronous cylinder shedding was established by using a modification of the method mentioned above. The velocity was set to either a higher or lower value for a stream tube just above a cylinder and also the stream tube just below the adjacent cylinder, as seen in Fig. 3.15. This produces a flow field that is segregated between high and low velocities with the interface located in front of each cylinder.

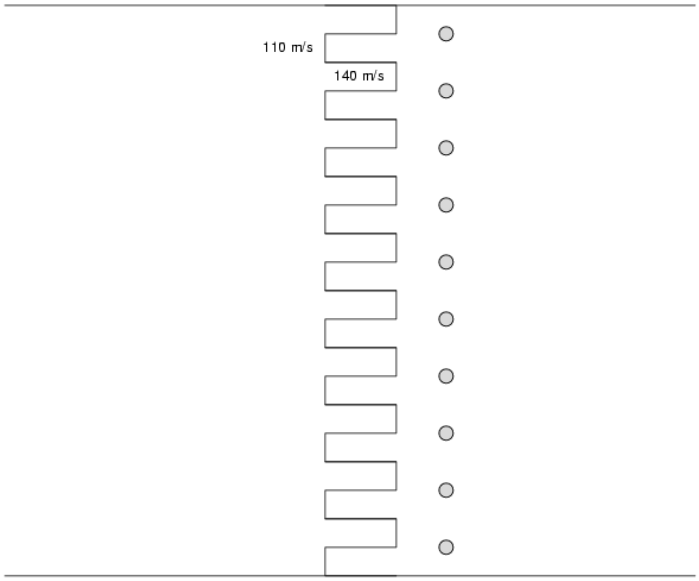

Figure 3.14 CFD Inlet Conditions Used to Create Synchronous Shedding

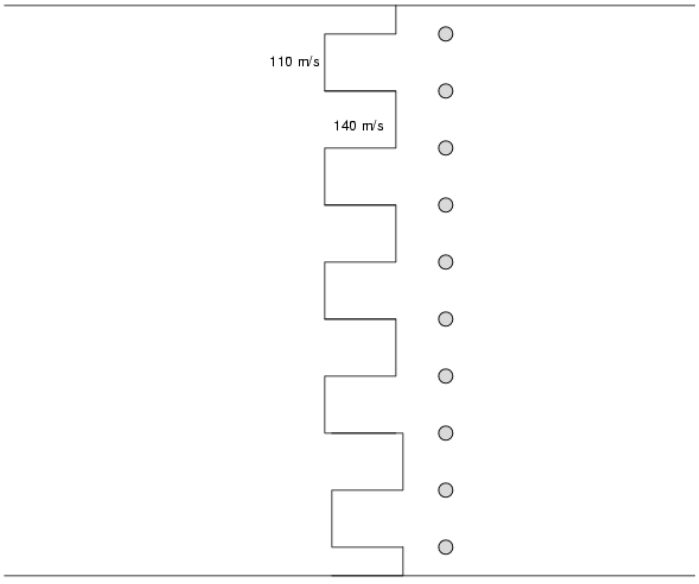

Figure 3.15 CFD Inlet Conditions Used to Create Asynchronous Shedding

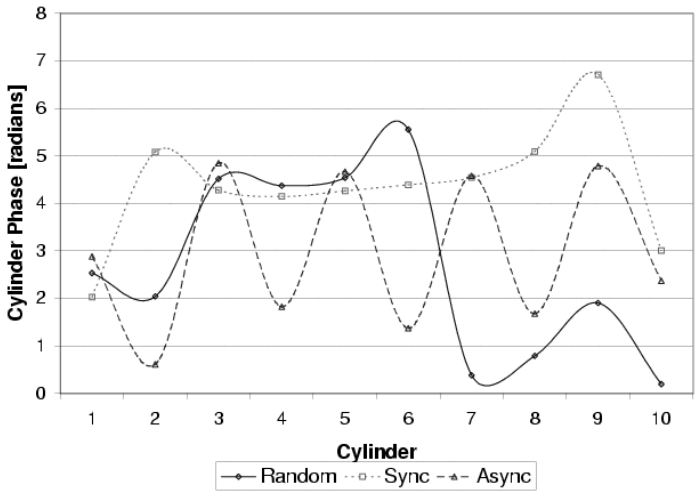

Figure 3.16 CFD Cylinder Shedding Phase for Synchronous and Asynchronous Shedding

3.6 Result Comparison

The phase of the vortex shedding on each cylinder for the three cases is shown in Fig. 3.16 with the phases from Fig. 3.8 plotted for comparison purposes. For the symmetric shedding case, the phase of cylinders 3-7 are all within 1/2 radian from each other, producing a flow with a strong coherent pattern. The asymmetric shedding case also produces a coherent pattern with each of the even numbered cylinders (except for cylinder 2) π radians out of phase from the odd numbered cylinders. Through the use of modified inlet conditions, the desired synchronous or asynchronous shedding was achieved and the resulting constructive and destructive interference on the upstream flow can be examined.

Velocity amplitude effects. The fluctuation amplitudes were measured at three different upstream locations for test section heights of -3.5 to 3.5 inches, as seen in Fig. 3.17. At each of these locations, the unsteady pressure and velocities were calculated for all three of the inlet conditions.

The values of the y-velocity fluctuation amplitudes at 1/2 inch upstream of the cylinder array are shown for the random, synchronous, and asynchronous shedding from the cylinders along with the single cylinder results in Fig. 3.18. The variation in amplitude of the fluctuations corresponds to cylinder spacing, with maximums on cylinder centerlines.

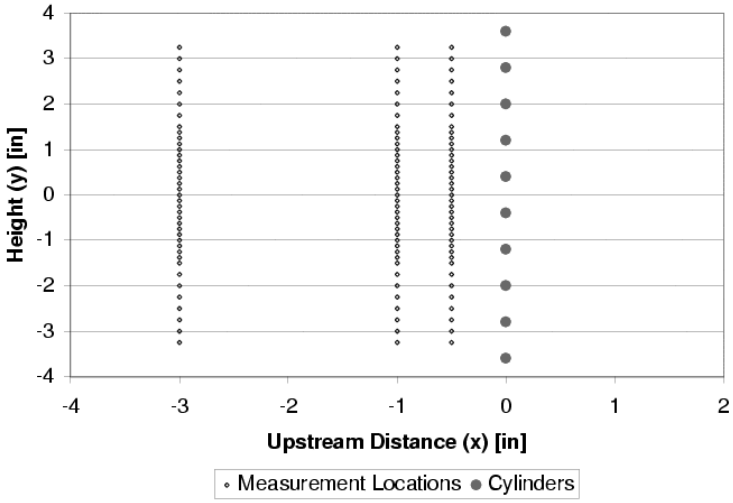

Figure 3.17 CFD Measurement Locations

The single cylinder case has a larger amplitude at the centerline of the tunnel because only the single cylinder case has a cylinder located at the centerline of the test section. The amplitude results of the multi-cylinder cases have very similar results, with the only difference being the magnitudes of the amplitudes.

At one inch upstream of the bank of cylinders, each of the cases produce very different results, as can be seen in Fig. 3.19. The influence of each individual cylinder is no longer noticeable, as can be seen in the lack of peaks directly upstream of the cylinders. The random shedding case results in a flow field lacking a coherent structure, with the largest amplitudes corresponding to the region directly upstream of the cylinders that are synchronized. The flow upstream of the cylinders shedding in a random fashion contains a large reduction in the unsteady velocity amplitudes. For all points, the amplitudes are larger than the amplitudes produced by the single cylinder case.

The asynchronous shedding produces unsteady y-velocity amplitudes closely resembling, in shape, the amplitudes present 1/2 inch upstream (shown in Fig. 3.18), but with lower magnitudes. The influence of each individual cylinder remains visible as peaks in the amplitudes in Fig. 3.19. Around the centerline of the tunnel, a large region exists where the single cylinder has a larger amplitude than the asynchronous case. This implies

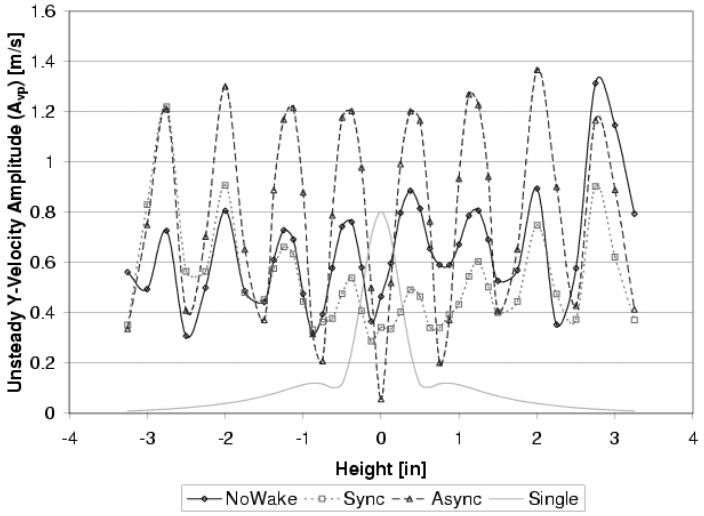

Figure 3.18 CFD Y-Velocity Amplitudes 1/2 Inch Upstream of Cylinder Array With Coherent Shedding

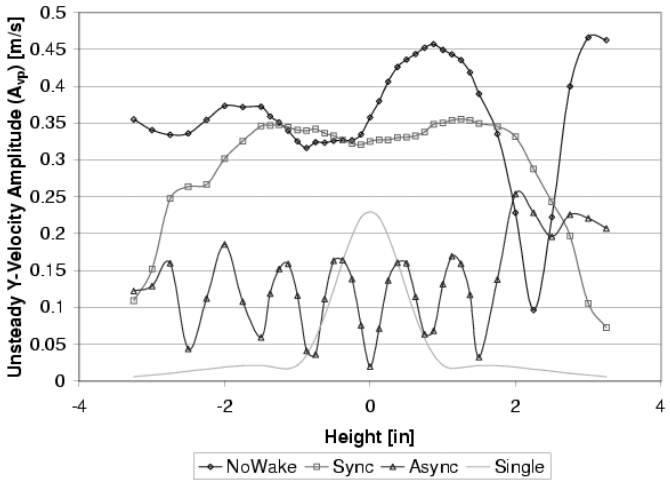

Figure 3.19 CFD Y-Velocity Amplitudes 1 Inch Upstream of Cylinder Array With Coherent Shedding

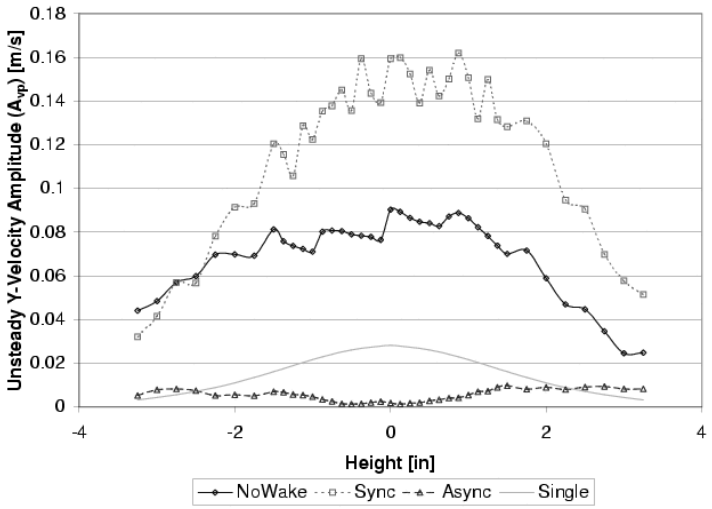

Figure 3.20 CFD Y-Velocity Amplitudes 3 Inches Upstream of Cylinder Array With Coherent Shedding

that the velocity amplitudes created by the asynchronous flow field are being reduced with distance at a higher rate than for the single cylinder case.

The synchronous shedding case, also shown in Fig. 3.19, produces amplitudes which are roughly constant with height through the center of the test section, from approximately -2 in to 2 in. Beyond this region, there is a sharp drop-off of the amplitude as the wall effects alter the shedding and, in turn, the amplitudes at these points. Like the single cylinder results, the amplitude fluctuations for the synchronized shedding cylinders are approximately symmetric about the centerline of the tunnel.

The effect of upstream distance on the velocity amplitudes is more noticeable at a distance of three inches upstream, shown in Fig. 3.20. The amplitudes of both the random and synchronous shedding are approximately symmetric about the centerline of the tunnel, similar to the single cylinder case. The effect of the array of cylinders for both cases is a large increase in the amplitudes over the single cylinder case. The random shedding produces amplitudes three times greater, and the synchronous shedding results in a fivefold increase.

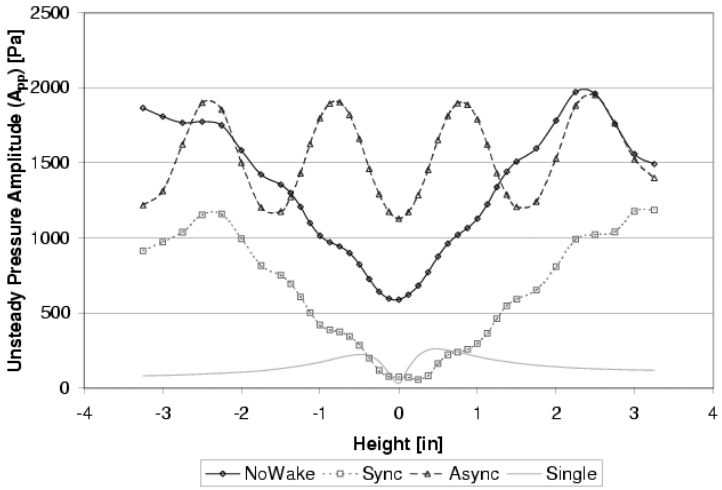

Figure 3.21 CFD Pressure Amplitudes 1/2 Inch Upstream of Cylinder Array With Coherent Shedding

The asynchronous shedding case produces the lowest amplitudes of the four cases. Along the centerline, as shown in Fig. 3.20, there are virtually no y-velocity fluctuations in the flow because of the destructive interference of the cylinders.

Pressure amplitude effects. The pressure amplitudes at points 1/2 inch upstream are shown in Fig. 3.21. For each of the four cases shown, a minimum in the pressure amplitude is produced along the centerline. For the single cylinder case, this is expected because the centerline is a stagnation streamline for the flow field.

For the synchronous and random shedding cases, the shape of the amplitudes is in the form of a "V" with the minimum located at the centerline. The unsteady pressure amplitudes are maximum towards the top and bottom walls for these two cases. For the symmetric shedding solution, the centerline of the test section has the smallest pressure fluctuations because the pressure effects from each cylinder above the centerline are reduced by the corresponding cylinder below the centerline.

As seen in Fig. 3.21, asynchronous shedding produces results that are very different from the other cases. The pressure amplitudes oscillate with test section height (y-direction) in a sinusoidal fashion. The peaks and valleys of the pressure amplitudes corre-

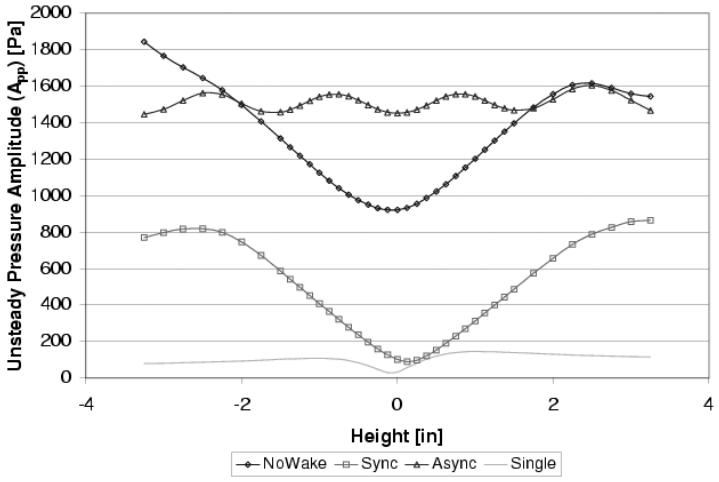

Figure 3.22 CFD Pressure Amplitudes 1 Inch Upstream of Cylinder Array With Coherent Shedding

spond to the stream tubes used to create this flow field. The maximum amplitudes occur at the center of the high speed streamtubes, and the minimum is in the center of the low speed. The frequencies of the velocity fluctuations (ω) are equal for all points in the flow field, so only the amplitudes are influenced by the velocity streamtubes.

In order to understand the influence of upstream distance on the unsteady pressures, the curve-fit amplitudes for points one inch upstream are shown in Fig. 3.22. Unlike the velocities, shown in Figs 3.18 and 3.19, the mean values of the unsteady pressure amplitudes for the multi-cylinder cases are unaffected by the upstream distance. In contrast, the single cylinder pressure amplitudes are reduced by approximately 50% from the values from Fig. 3.21.

Synchronous shedding produces the same basic shape as was produced at 1/2 inch upstream, but the values are slightly reduced in the high amplitude regions. The minimum amplitudes are increased with the increased distance, and are located above the centerline at a y distance of 0.125 inches. Likewise, the random shedding amplitudes are in the same shape as for the 1/2 inch upstream case. The amplitudes in the heights corresponding to the high amplitude region are approximately the same between the two upstream distances,

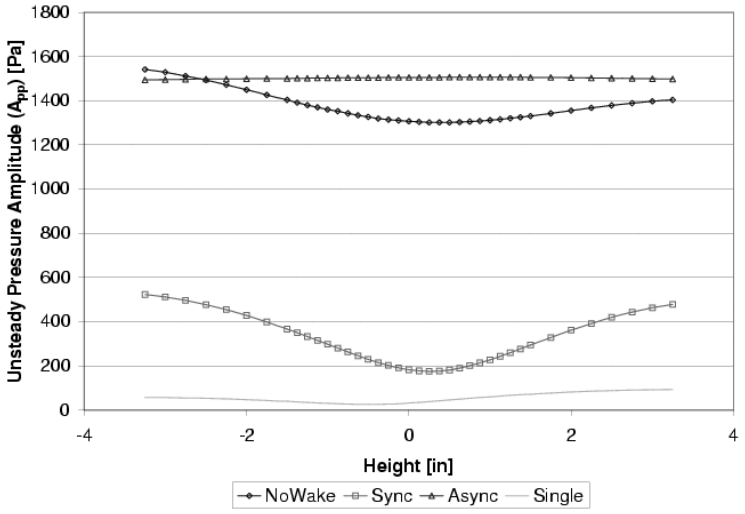

Figure 3.23 CFD Pressure Amplitudes 3 Inches Upstream of Cylinder Array With Coherent Shedding

varying slightly at each point. The minimum unsteady amplitude one inch upstream is 50% larger than the corresponding unsteady amplitude at 1/2 inch upstream.

The difference in the shape of the amplitudes for the asynchronous shedding is clearly noticeable between Figs. 3.21 and 3.22. The sinusoidal pattern present at 1/2 inch upstream is almost nonexistent at double that distance, however the mean unsteady amplitude (with y-direction) at the upstream distance of one inch is the same as for the upstream distance of 1/2 inch. The pressure amplitudes created are not dependent on the y-location in the flow field. At a distance of one inch upstream, the unsteady pressure wave from the asynchronous shedding appears to be unaffected by the walls of the test section. the one-dimensional propagating pressure wave will appear as a "chugging" of the tunnel in regions greater than one inch upstream.

The furthest upstream pressure amplitude data was taken from an upstream location of three inches, shown in Fig. 3.23. The pressure amplitudes for the single cylinder case are almost nonexistent for a distance this far upstream, but the influences of the multi cylinders are still strong.

For both the random and synchronous shedding, the minimum amplitudes continue to increase with increasing upstream distance as the higher amplitude regions decrease with

distance, as seen in Fig. 3.23. This creates unsteady pressure amplitudes that contain less variation with the test section height (y-direction) than were present at upstream distances closer to the cylinders. The random shedding produces larger pressure fluctuations, approaching the values of the asynchronous shedding. The interference of the unsteady pressure waves generated by each cylinder constructively or destructively interfere to produce the unsteady pressure field.

The amplitudes of the pressure created by asynchronous shedding are unaffected by upstream distance. Once the distance is large enough to eliminate the sinusoidal results shown in Fig. 3.21, the unsteady pressure amplitudes are constant with both height in the tunnel and upstream distance.

Implications. One important result from the unsteady flows created by the different inlet conditions is the fact that the pressure and velocity are not directly correlated. For the asymmetric case, the unsteady pressure amplitudes are approximately constant with upstream distance, but the unsteady velocity amplitudes fall-off rapidly. For the symmetric shedding case, the opposite is true. The pressure amplitudes are greatly reduced with upstream distance, but the velocity amplitudes reduce more slowly. The constructive and destructive interference of the waves generated by the cylinders causes this effect to occur. Thus, the expected result of larger unsteady pressure amplitudes being present with large unsteady velocity amplitudes does not hold for this flow, as will be further shown in Chapter VI.

3.7 Chapter Summary

Cylinders located in an array of cylinders, with a spacing to diameter ratio of 4.27, placed perpendicular to a freestream do not influence the shedding of the surrounding cylinders. The unsteadiness present in the flow caused each of the cylinders to shed in a random fashion with respect to the other cylinders.

CFD was used to determine the conditions required to force the cylinders to shed in a coherent fashion. Altering the inlet conditions using a square wave velocity inlet forced the cylinders to shed coherently. The width of the velocity square wave dictates whether

the coherence will be synchronous or asynchronous. The presence of shear layers in the flow impacting the cylinder array appears to have to effect of creating a form of coherent shedding of the cylinder array.

CFD predicts that the constructive and destructive interference produced from the synchronous and asynchronous flows will produce very different flows; thus knowledge of the shedding coherence type is important in determining an expected flow. The interference of the waves propagating from each of the cylinders causes the regions with largest unsteady pressure amplitudes to not necessarily have the large unsteady velocity amplitudes.

IV. Cylinder Array Downstream of a Cascade

Computational results from Chapter III indicate that the presence of wakes upstream of a cylinder array could force the cylinders to behave in a coherent fashion. A cascade was designed and built that would place an array of cylinders downstream of cascade blades. The shedding relation between three of the cylinders in this array was examined for different conditions to determine the requirements for coherent shedding.

4.1 Experimental Set-up

Tunnel. The cascade results were obtained using the tunnel described in Section 2.2. The test section used in Chapters II and III was removed and the cascade was bolted to the tunnel.

Cascade. The cascade was designed with flexibility in mind. The design included the ability to change the inlet angle, stagger of the blades, and the location downstream of the cylinders. Changing the inlet angle of the cascade allowed the wakes behind the blades to be strengthened, with increasing inlet angle, without changing the location of the wakes passing through the cylinder array. Variation of the cylinder downstream location was used to determine the effect of locating the forcing at different distances from the cascade, simulating different spacing between a set of stators and a rotor.

A diagram of the cascade can be seen in Fig. 4.1. The flow enters the cascade and is turned by the cascade blades before passing through the array of cylinders.

Three different inlet angles were used for this work: 19, 25, and 31 degrees. The stagger, and thus the exit angle, were kept constant. The stagger angle was 0 degrees, and the exit angle was 9 degrees. The total cascade turning was 28, 34, and 40 degrees for the 19, 25, and 31 degree inlets, respectively. The equivalent diffusion ratio [10] is calculated as 1.25, 1.35, and 1.50 from the 19, 25, and 31 degree inlet angles, respectively. The 31-degree inlet provided total turning of the flow roughly equivalent to the turning used by Fabian [13]. The two lower cascade angles were used to determine the effects of weaker wakes from the blades, created by less turning, on cylinder coherence.

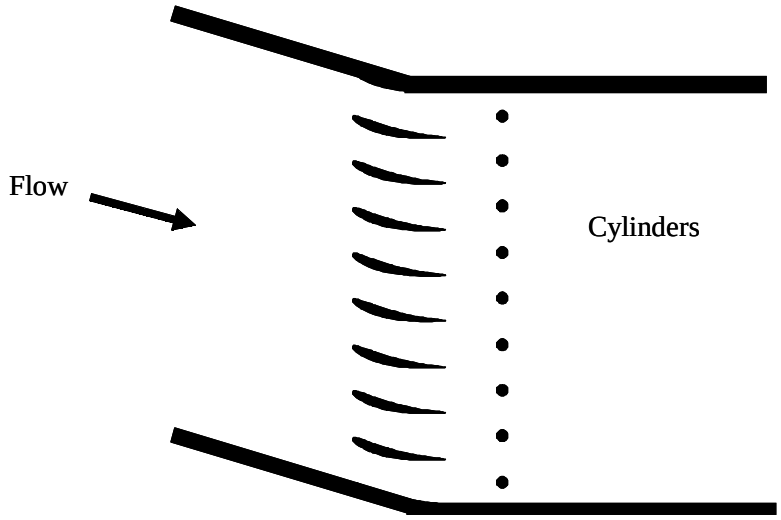

Figure 4.1 Diagram of the cascade set-up

The stagger angle was held constant to ensure that the wakes from the cascade blades would be located at the same location for each of the runs. A constant stagger angle forced the exit angle of the flow from the blades, and thus the wake location, to be constant.

The cross sectional area of the inlet into the blades was 9 inches by 2 inches, giving a total cascade inlet area of 18 square inches. The outlet of the test section was 9 1/2 inches by 2 inches. The length of the test section was 15 inches. The top and bottom walls downstream of the blades were hinged to allow for easy movement of tailboards which are used to balance the flow.

Blades. The blade profile was generated from mid-span coordinates of a F109 compressor blade as given by Fabian [13]. The blades have a chord length and width of 1.5 and 2 inches, respectively. The blade spacing was one inch, creating a solidity, σ, of 1.5. The maximum thickness of the blade was 0.12 inches located at the center chord. The camber angle of the blade is 48 degrees. The inlet and outlet blade angles are 25.6 and 22.7 degrees, respectively.

Each blade was pinned to allow rotation about the 75% chord location, allowing the stagger, or setting angle (see Fig. 4.2), of the cascade to be modified. A slider located

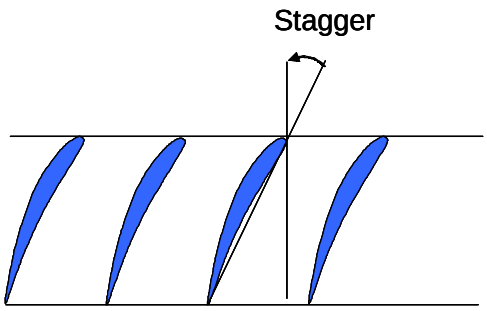

Figure 4.2 Stagger of a Cascade

at the leading edge of the blades allowed all of the blades to be rotated simultaneously through a total rotation of 45 degrees.

Cylinder holder. The downstream sidewall of the cascade was designed to allow cylinders to be placed in the flow with one cylinder located within each blade passage. The presence of a single cylinder within each passage could simulate a downstream rotor with approximately equal number of blades as the stator. To achieve this, the cylinders were placed at a distance of one inch between the cylinder centerlines, with a total of nine cylinders located in the flow. The ratio of the distance between cylinders to the diameter (d/D) for this configuration was 5.33. The cylinder diameter was kept at 3/16 $\pm$0.0005 inch in order to keep the shedding frequency the same.

The height of the cylinder within the passage is controlled using a set of 8-32 screws that allowed the cylinders to be moved as an array, keeping the one inch separation between cylinders at all times. The height of the cylinders in the test section was accurately set to within 1/128 inch by using quarter turns of the screws. The design allowed the cylinders to be moved while the tunnel was running, reducing the need for tunnel shut-down and allowing for thermal equilibrium to be maintained during the high velocity case. The total travel for the cylinder height was 1 1/8 inches.

The downstream portion of the test section was designed to allowed the greatest flexibility in the downstream location of the cylinders. A modular design of the walls allows the cylinders to be placed any distance between 1/2 inch to 16 inches downstream of the blades in 1/4-inch increments. For the purpose of this work, the data was obtained

with the cylinders located downstream in 1/2-inch increments, with the cylinders between 1/2 inch and 1 1/2 inch downstream, or 1/3 to one chord downstream. Typical axial gap between blade rows in a compressor is 30% chord [51] (approximately 1/2 inch in this work).

Data acquisition. The data acquired for the analysis of the cylinder shedding downstream of a cascade consisted of the tunnel total temperature and three channels of the unsteady pressure voltage. The data acquisition process was identical to the process used in Chapter III. The data acquisition speed used for the data collection was 120 kHz.

Each unsteady pressure measurement was produced by an ultraminiature Kulite XCS-062 [39] differential pressure transducer powered by a Vishay Measurements Group model 2310 Signal Conditioning Amplifier [40]. The amplifiers, which passed only the AC component of the signal, provided only the fluctuations of the pressure.

4.2 Results

The CFD results indicated that a coherent shedding pattern between cylinders could be produced if the flow field impinging the cylinders has variations such as wakes. Two different types of coherent shedding were created in the CFD solutions: symmetric and asymmetric. Previous work by Ohya et al. [47] indicates that only asynchronous shedding can be experimentally created at these velocities (85 m/s through 135 m/s). As will be seen, the creation asymmetric cylinder shedding was verified in this experiment.

Histograms. The relative phase of the 3rd cylinder with respect to the 5th cylinder was examined to determine the cylinder shedding. These cylinders were chosen because the vortex shedding of these two cylinders would be in phase for both synchronous and asynchronous shedding.

The phase difference between the two cylinders in an array located 1/2 inch downstream of the blades is shown in Fig. 4.3 for a cascade exit velocity of 85 m/s. As can be seen, there is no evidence of a peak in the shedding, indicating that the cylinders are shedding in a random fashion for this flow field.

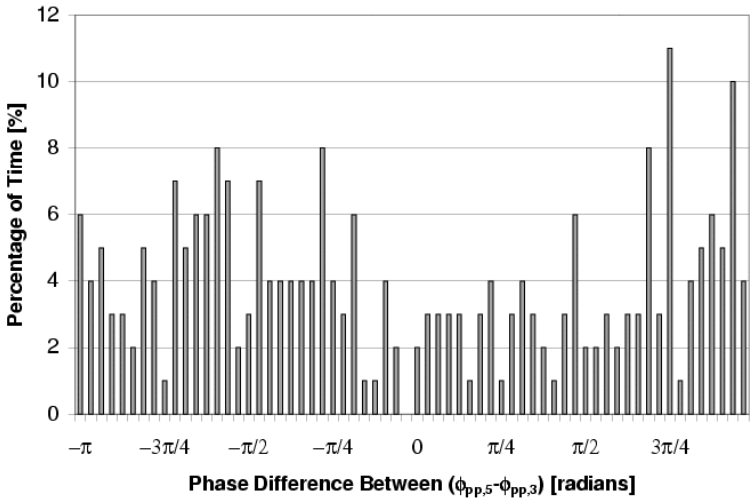

Figure 4.3 Phase Difference Between Cylinders 3 and 5 for 85 m/s Cascade Exit Velocity

The relative shedding between the cylinders for a cascade exit velocity of 135 m/s is shown in Fig. 4.4. Unlike the trends present in Fig. 4.3, a clear peak is present in the phase differences. The histogram results resemble a normal distribution rather than the random histogram. The mean of the histogram is centered around 0 phase difference between the two cylinders, indicating that the cylinders are shedding in phase.

The pressure voltages of three cylinders placed in the flow field used for Fig. 4.4 are shown in Fig. 4.5. The pressure was measured on the 3rd, 4th, and 5th cylinders. As determined from the histogram, cylinders 3 and 5 have peaks that occur at the same time. Cylinder 4, however, has peaks exactly out of phase with the other two cylinders, indicating that the cylinders are shedding in an asynchronous fashion.

Velocity effects. As seen in Figs. 4.3 and 4.4, the exit velocity from the cascade is very important in creating a coherent cylinder shedding pattern. The standard deviation of the mean relative phase differences between two cylinders for various velocities can be seen in Fig. 4.6. As can be seen, the standard deviation decreases with increasing freestream velocity. This decrease in the standard deviation occurs because the cylinders are shedding coherently in a higher percentage of samples taken at higher velocities. The velocity plays

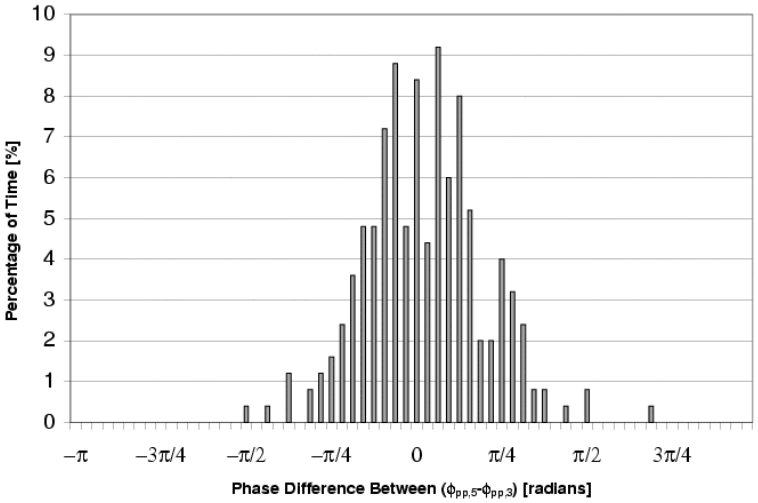

Figure 4.4 Phase Difference Between Cylinders 3 and 5 for 135 m/s Cascade Exit Velocity

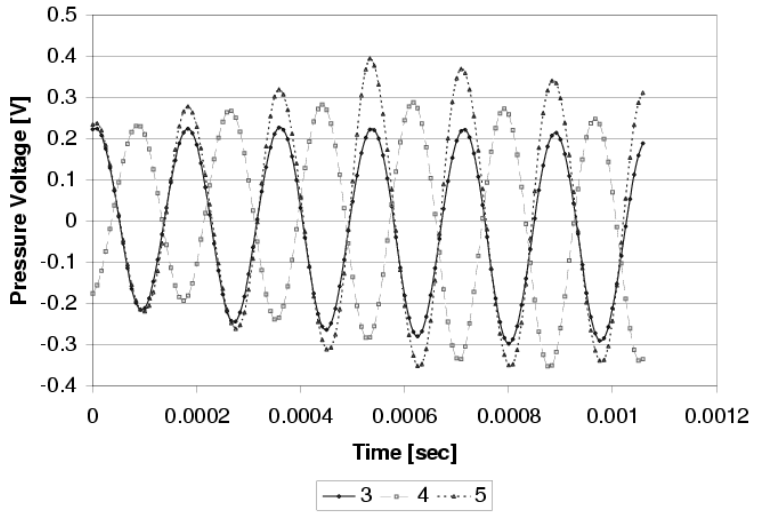

Figure 4.5 Ensemble Averaged Pressure Trace for Cylinders Located Downstream of Cascade

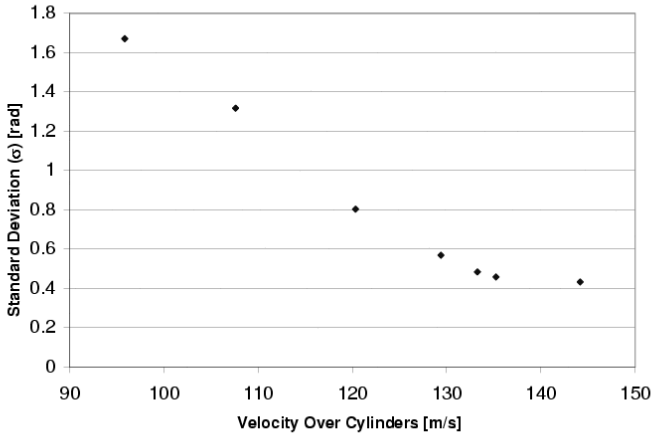

Figure 4.6 Standard Deviation of the Mean Relative Phase Differences Between Cylinders 4 and 5 for Various Velocities

a major roll in the coherence of the cylinder shedding, with higher velocities ensuring a more coherent cylinder shedding pattern.

Cylinder height effects. Like the velocity, the height of the cylinders within each passage plays a role in creating coherent shedding from the cylinders. The height was measured with respect to the chordline of a cascade blade in the test section. A negative value indicates that the cylinders are located in the passage below the design passage for that cylinder, creating a passage without a cylinder, and dropping one of the cylinders from the flow field.

The standard deviation of the mean relative phase difference between cylinders four and five is shown for various cylinder heights for an exit velocity 125 m/s in Fig. 4.7. The effects of the cylinder height on the shedding coherence can be clearly seen. The minimum coherence exists for the point where the cylinder is located either directly behind the blade, or slightly toward the suction side of the blade, where flow separation over the blade is present. Increasing or decreasing the cylinder height from this point creates a more coherent flow field. The minimum standard deviation measured was for the cylinder location of 1/2 inch, exactly half way between the blades.

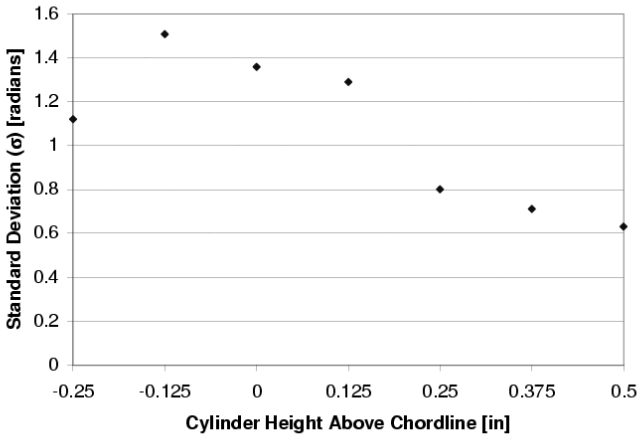

Figure 4.7 Standard Deviation of the Mean Relative Phase Difference Between Cylinders 4 and 5 for Various Cylinder Heights

The cylinders could not be moved above 1/2 inch. The value for the cylinder location of -0.25 inches is equivalent to 0.75 inches due to the periodicity of the cascade. As can be seen in Fig. 4.7, the standard deviation of the cylinder shedding is greater for -0.25 inches than it is for 0.5 inches, indicating a reduction in coherence for cylinders located at 0.75 inches.

Reduced number of cylinders. Two possible scenarios were developed to explain the phenomenon of the cylinder shedding coherence downstream of the cascade as the velocity is increased. The first explanation was that the wakes from the blades increases the maximum cylinder spacing that will provide coherent shedding. Without the upstream blades, the required distance for synchronous shedding is less than 3.5 diameters. The wakes allow for a spacing of 5.33 to behave coherently. The second explanation was that the wakes from the blades directly cause the coherence of the cylinders. These explanations can be differentiated by increasing the distance between the cylinders.

For the second explanation, the cylinders are not being influenced by the neighboring cylinders and the spacing between cylinders is irrelevant. The CFD results for the freestream flow field from Chapter III is an example of this. The removal of cylinders

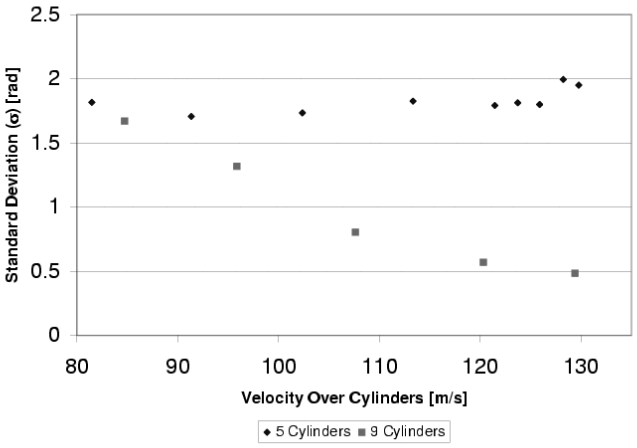

Figure 4.8 Standard Deviation of the Mean Relative Phase Difference Between Two Cylinders at Various Velocities for 9 and 5 Cylinder Arrays

would not alter the shedding relationship of the remaining cylinders because the coherence is caused by the forcing present in the inlet velocity conditions.

The theory of the wake directly dictating the shedding coherence was tested by removing half of the cylinders from the cylinder array. Every other cylinder was removed, producing a cylinder array with five cylinders and a spacing of two inches between cylinders ($d/D = 10.66$). If the wakes of the blades were directly causing the coherence in the cylinder shedding, the results from an array of half cylinders should have the same coherence as the same cylinder location in an array with all of the cylinders.

A plot similar to Fig. 4.6 can be used to compare the coherence of shedding between the full array and the half array of cylinders. As can be seen in Fig. 4.8, the removal of half of the cylinders has a very strong effect on the standard deviation of the mean relative phase difference, and thus the coherence of the shedding. The five-cylinder array has random shedding between the cylinders which is not a function of velocity.

Therefore, it is assumed that the first explanation is correct. The coherence of the cylinders downstream of a cascade appears to be caused by the wakes from the upstream

blades increasing the maximum spacing where the cylinders will shed coherently in an asymmetric fashion.

Data Acquisition Effects on Measured Cylinder Coherence. The histograms shown in Figs. 4.3 and 4.4 show the relative phase difference between two cylinders at a given time for a specific trigger cylinder vortex shedding strength. As mentioned in Chapter II, the data acquisition process used for this work captured voltages only when a peak in the cylinder pressure was a certain level. This process does not provide a clear look at the coherence length of the shedding between two cylinders. The process used in this work only looked at a small percentage of the vortices shed by a cylinder. Each of the vortices examined were of the same strength (seen in the pressure voltage peak).

The coherence length of the vortex shedding between two cylinders can be determined by examining a long set of data without the use of a trigger and then determining the number of vortices shed coherently before the shedding becomes random. The standard deviation of the mean phase difference between two cylinders is not a measure of the coherence length of the vortex shedding, but rather is a measure of the expected phase relation between two cylinders in an instant in time with the trigger cylinder shedding a vortex of a specific strength.

4.3 Chapter Summary

As predicted by CFD, coherence of the vortex shedding between cylinders in an array was produced; however only asynchronous shedding was obtained. The coherence is eliminated when the spacing between cylinders is doubled to one cylinder per two blades, indicating that the wakes from the blades allow for the coherence of cylinders over a larger spacing than is possible without the wakes.

The CFD results presented in Chapter III predicted that the presence of shear layers in the flow creates coherent cylinder shedding. The cascade velocity shedding shows that the shear layers from the cascade blades does create asynchronous cylinder shedding. However, the shear layers only create coherent shedding for a limited range of cylinder spacing.

Doubling the cylinder spacing without altering the blade spacing will not produce the coherent cylinder shedding.

Two main influences on the intermittency of the coherence are the velocity over the blades and the location of the cylinder within the passage. The higher velocities produced longer periods of coherence. The optimal cylinder height location occurred at the centerline of each passage, with respect to the blade chordlines.

V. Unsteady Velocity Measurements on a Blade Upstream of a Cylinder Array

The use of a cascade to produce coherent shedding between cylinders was shown in Chapter IV. The unsteady velocity amplitudes along the blades caused by the coherence was desired to be measured. Previous work by Fabian [13] predicted that the unsteady pressure and velocity amplitudes would be maximum toward the trailing edge of a blade. For this work, the unsteady velocities were measured along the blade.

5.1 Data Collection Hardware

Velocity measurements over the blade surface required the velocity probe to be inserted from the side of the tunnel, preventing the use of the split-film sensor used for the single cylinder results. A different experimental set-up from the one used in Chapter II was required for the cascade velocities. A diagram of the set-up can be seen in Fig. 5.1.

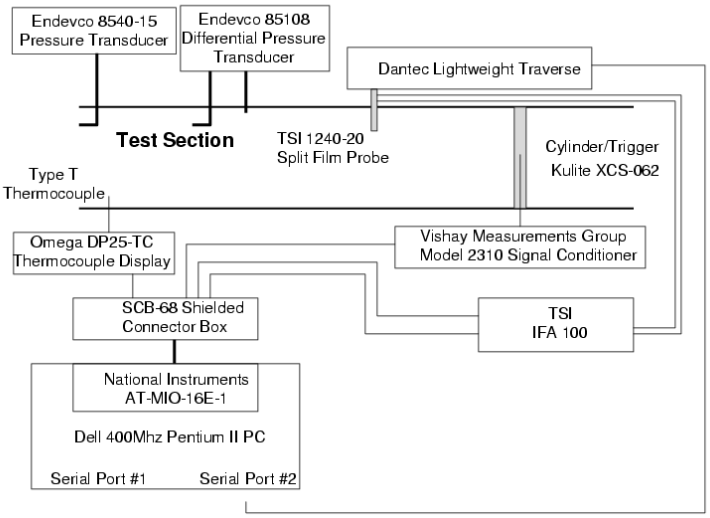

Figure 5.1 Data Acquisition System for Cascade

Velocity measurements. A TSI model 1240-20 cross flow x-film [37] was used for velocity measurements along the blade surface. A film sensor was chosen over a wire sensor for the added robustness present in the film. The main disadvantage in using a film is that

the frequency response is lower than the response of a wire. For this work, the desired frequencies are well within the performance of the film.

Each wire of the sensor is controlled through the use of a TSI IFA-100 Intelligent Flow Analyzer [37]. The IFA-100 operated the sensors and also provided a signal conditioner which was used to modify the signal through implementation of a gain and offset. The voltage from the internal signal conditioner was then captured by the SCB-68 [42] shielded connector box.

The location of the x-wire sensor on the blade was controlled in three dimensions by a Dantec Lightweight Traverse [38]. The spanwise location was set to 1/16 inch from the center of the test section and remained in that position for all measurements. The traverse was used to move the sensor along the surface of the blade to allow measurements between 50% and 100% chord. The location of the sensor along the blade was verified visually through the use of marks along the blade edge corresponding to every 10% of the chord.

The shaft of the probe was placed touching the span of the blade, allowing the intersection of the sensing wires to be located 0.0625 inches from the blade surface. The cross-sectional height of the sensors measured the velocity from approximately 0.05 to 0.075 inches from the surface of the blade.

The blade holder was designed specifically to allow maximum access to the blade with the hot wire sensors. A slot was cut 3/16 inch wide and 5/8 inch long. The end of the long side of the slot is able to be rotated about the blade rotation point (75% chord), allowing velocity measurements anywhere along the blade surface between 40% up to 100% chord.

Unsteady pressures. The data collection was triggered using the unsteady pressures on the cylinder surface through the use of an ultraminiature Kulite XCS-062 [39] differential pressure transducer. This set-up was further explained in Section 2.2

Steady pressure. Steady pressure measurement was required for various parameters needed for this research. These parameters included the ambient room pressure, the tunnel stagnation pressure, and the static pressure through the blades.

For the ambient room pressure and the tunnel stagnation pressure measurements, an Endevco model 8540-15 [52] was used. This model provides measurements in the range of 0-15 psia. The values for the pressures were manually entered into the database.

The static pressure was measured using an Endevco model 85108 [52] transducer that has a range of 0-2 psig. The static pressure port on the sidewall just in front of the blades was referenced to a pitot probe inserted into the flow along the centerline, 1.5 inches from the bottom wall of the inlet block. Like the stagnation pressures, the static pressure differential was entered into the database.

Thermocouple measurements. All temperature measurements obtained in this research were obtained using Type-T thermocouples. An Omega DP25-TC [41] thermocouple meter was used to display the temperatures.

A thermocouple placed in the stagnation chamber, downstream of the plug, was used to measure the temperature of the flow field. In this region, the flow was approximately 10 ft/s, allowing for the assumption that the measured recovery temperature is the stagnation temperature of the flow.

The temperature of the hot-film calibration system was very critical in developing the velocity calibrations. A thermocouple was placed in the settling chamber of the calibrator to measure this temperature.

The flow temperature affects the voltages from the hot-wire probes. If not corrected, higher temperatures cause a slower velocity to be measured. Appendix F further describes the equations used to correct for the temperature.

Data acquisition system. The analog voltage outputs from the CTA sensors, the pressure voltage from the Model 2310 signal conditioner [40], and also the voltage from a thermocouple located in the stagnation chamber of the tunnel were collected by a National Instruments SCB-68 shielded connector box. The voltages were phase-locked and acquired by the computer in the process explained in Section 2.2. The data was acquired at 120 kHz for this work.

Velocity calibration. The TSI 1240-20 was calibrated using a TSI model 1125 calibrator [37]. This calibrator allowed the incoming compressed air to be heated to allow the stagnation chamber temperature to reach the temperatures present in the tunnel during data collection. Like the calibration performed for the split film sensor, the calibration of the x-film required a two-step process.

The first step was to estimate the velocity seen by each sensor. This portion of the calibration was completed with a non-dimensional curve fit between the Nusselt Number and Reynolds Number using [53]

$$Nu = C_{cal} + D_{cal}\,\mathrm{Re}^{0.45} \tag{5.1}$$

where C_{cal} and D_{cal} are determined through the calibration.

Once the estimated velocity over each sensor is calculated, the second step can be performed that calibrates the probe for the flow angle. The angle calibration was performed by altering the probe angle in 6 degree increments between -30° to 30°. The estimated velocities are used to created an estimated velocity magnitude, $\vec{V}_{est}$, and angle of flow, α_{est}. The parameters are then used to determine the true angle by

$$\alpha_{true} = a_{a0} + a_{a1}\alpha_{est} + a_{a2}\alpha_{est}^2 + a_{a3}\alpha_{est}^3 \tag{5.2}$$

where α_{true} is the true angle, and a_0 through a_3 are calibration constants. Through an empirical process, the third order calibration equation, Eq. (5.2), was established. The cubic term, a_{a3} was less than 1% of a_{a2} for every case, and a fit using a fourth order term produced negligible constants on the fourth order term.

Once the angle is known, the velocity ratio can be calculated as

$$R_v = a_{v0} + a_{v1}\alpha_{true} + a_{v2}\alpha_{true}^2 a_{v3}\alpha_{true}^3 \tag{5.3}$$

where a_{v0} through a_{v3} are calibration constants and R_v is the velocity ratio which is used to calculate the true velocity magnitude as

$$\vec{V} = \frac{\vec{V}_{est}}{R_v} \tag{5.4}$$

The velocity calculated in Eq. (5.4) and the angle from Eq. (5.2) are then used to decompose the velocity into the Cartesian velocity components. More details of the calibration process can be seen in Appendix F.

5.2 Data Reduction

Each file acquired by the data acquisition process contains 500 samples. Each sample consists of one temperature voltage, the velocity voltage of each velocity component, and the pressure voltage acquired at 128 sequential time steps.

The first process for data reduction was ensemble averaging of each file. After the voltages have been ensemble averaged, the temperature voltages over the 128 sequential points are averaged to produce a single voltage that is converted to a temperature which is used to calculate the non-dimensional parameters used in Eq. (5.1). The other parameters required in calculating the parameters, pressure for example, are entered manually into a database which is queried by the data reduction process.

The unsteady pressures and velocities are then fit to the sinusoidal equations, used in Chapter II. The curve-fit equations, Eqs. (2.7) and (2.8), are shown again for convenience as

$$P = \bar{P} + A_{pp} \sin\left(\omega t + \phi_{pp}\right) \tag{5.5}$$

and

$$\begin{aligned} u &= \bar{u} + A_{up} \sin\left(\omega t + \phi_{up}\right) + A_{uh} \sin\left(2\omega t + \phi_{uh}\right) \\ v &= \bar{v} + A_{vp} \sin\left(\omega t + \phi_{vp}\right) + A_{vh} \sin\left(2\omega t + \phi_{vh}\right) \end{aligned} \tag{5.6}$$

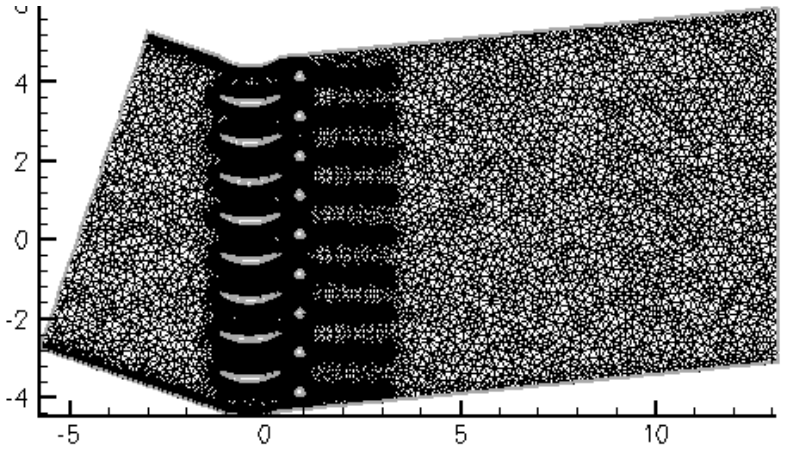

Figure 5.2 Cascade grid

5.3 Role of CFD for This Work

As seen in Chapter II, CFD results for the single cylinder case did not match the experimental results. For the case of the cylinder array, CFD was used to guide the experimental set-up after it was discovered that modifying the wake-like inlet conditions created coherent shedding for the cylinders. With this CFD success in mind, the computational results for the cylinders downstream of a cascade were used to drive expectations of the effects of configuration changes to the experimental set-up. The overall CFD results can be seen in Appendix E.

The cascade was modeled using Gridgen [54] through the use of both structured and unstructured grids. A structured grid was created from the surface of each of the blades and cylinders as seen in Fig. 5.2. The remaining area was filled using an unstructured grid.

CFD simulations were executed using an unsteady, laminar, incompressible model. The time step used for the solution was 2.0833×10^{-6}. A total of 25,000 iterations were used to converge the solution to the constant amplitude oscillations.

5.4 Discussion of Flow Transition

Steady State Flow. The location of the transition point, for the case of 19 degree inlet angle, from laminar to turbulent flow was calculated using two different models: the

one-step method of Michal and the correlation of Dunham [31]. The one-step method of Michal only accounts for the effect of a pressure gradient on the transition point. The correlation of Dunham accounts for both the pressure gradient and the inlet turbulence level. For this calculation, the turbulence level in the inlet was 1.5% [36]. These two methods are explained in Appendix G. The local velocities, outside of the boundary layer, for the entire chord of the blade were obtained from CFD results. Experimental velocity measurements were not available towards the leading edge of the blade, as is required for both models.

The results from both models show that the favorable pressure gradient on the pressure side of the blade prevents transition from occurring . Thus, laminar flow is expected along the entire chord of the blade on the pressure side. Both models predict transition from laminar to turbulence at 63% chord on the suction side of the blade. This transition point is approximately 12% chord upstream of the measured separation point of the flow.

Unsteady Flow. The amplitudes of the unsteady oscillations can cause the flow over a blade to transition at a location upstream of the steady state transition point. According to White [31], the unsteady Reynolds number can be used to determine if the oscillating flow causes transition. The unsteady Reynolds number can be written as [31]

$$\mathrm{Re}_{ns} = \frac{N_A U_o^2}{\omega \nu} \tag{5.7}$$

where ω is the frequency of the fluctuations, ν is the kinematic viscosity, and N_A is determined from fitting the velocity at the point to

$$U = U_o \left(1 + N_A \sin(\omega t)\right) \tag{5.8}$$

From White [31], if the unsteady Reynolds number is greater than 26,000, the influence of the unsteadiness will have an effect on the transition of the flow. From the unsteady velocities of this work, the amplitude of the unsteady velocities is of the order of 1 m/s. Thus, $N_A = 0.008$. The unsteady Reynolds number for the flow is approximately 250, a factor of 100 less than the values required for the transition point to be influenced.

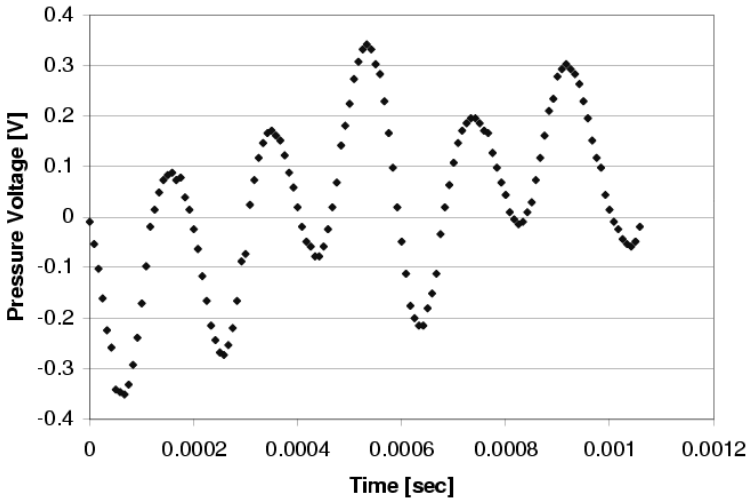

Figure 5.3 Cylinder Pressure Trace Downstream of Cascade Blades

The amplitudes of the unsteady velocities present along the blades does not effect the location of the transition point along the blade surface. The transition point is determined from the steady state flow transition.

5.5 Typical Results

The results taken from 70% chord on the pressure side of the blade are used to show the typical results. These results were chosen because the velocity fluctuations at this location were smaller than towards the trailing edge, so the curve-fit will be poorer for this location. A single trace of the pressure can be seen in Fig. 5.3. The inherent unsteadiness of the pressure signal can be seen. The sinusoidal nature of the cylinder shedding is evident; however, the peaks and valleys in the signal are not constant with time.

A single trace of the x-velocity contains no visually noticeable characteristic at the cylinder shedding frequency, as seen in Fig. 5.4. The high unsteadiness present in the velocity dominates the effects of the cylinder, causing single-point fluctuations of ± 3 m/s. Any attempt to curve-fit the x-velocity shown in this single trace would produce results that are erroneous.

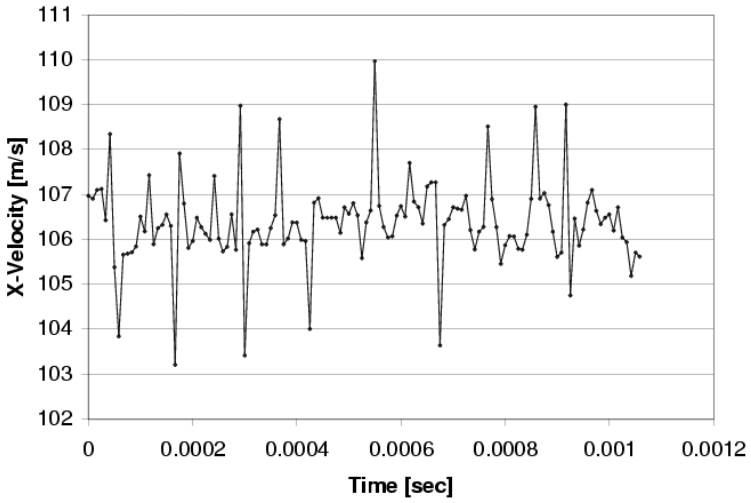

Figure 5.4 X-Velocity Trace From 70% Chord, Pressure Side

Ensemble averaging the pressure signal creates a clean sinusoidal wave, as seen in Fig. 5.5. The peak voltage in the center of the signal is still larger than the other peaks because the center peak is forced to be a maximum during collection of each trace. The unsteadiness, as seen in Fig. 5.3, causes the remaining peaks to be diminished in the ensemble average. Any unsteadiness seen as either an amplitude reduction or a change of the vortex shedding frequency will cause a reduction in the pressure peaks at points other than the trigger point when ensemble averaged.

The ensemble averaged pressure is accurately described by a single frequency sine wave, as shown in Fig. 5.6. The peak used for the data collection trigger is not fully captured, but the remaining peaks are well fit by the single sinusoidal curve.

A two-frequency sinusoidal fit is used to describe the ensemble average of the x-velocity, as seen in Fig. 5.7. Like the single cylinder results from Chapter II, the oscillations at the cylinder shedding frequency dominates the signal. The amplitude from the harmonic frequency fit, A_{uh}, is less than 2% of the primary frequency amplitude, A_{up}, and thus can be neglected. The ensemble averaged x-velocity still contains a large amount of noise due to the very small amplitude of the unsteady velocity caused by the cylinder. The two-frequency curve-fit does a good job of describing the velocity present at this point. In the regions with larger fluctuations, the curve-fit performs even better.

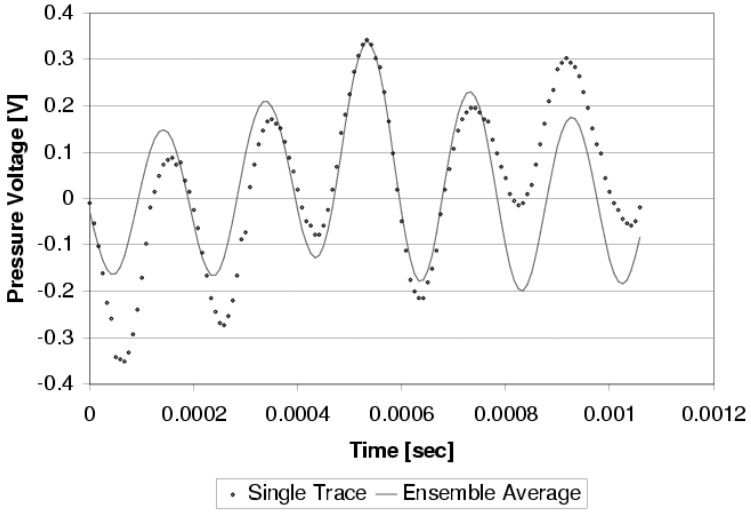

Figure 5.5 Ensemble Averaged Cylinder Pressure Trace Downstream of Cascade Blades

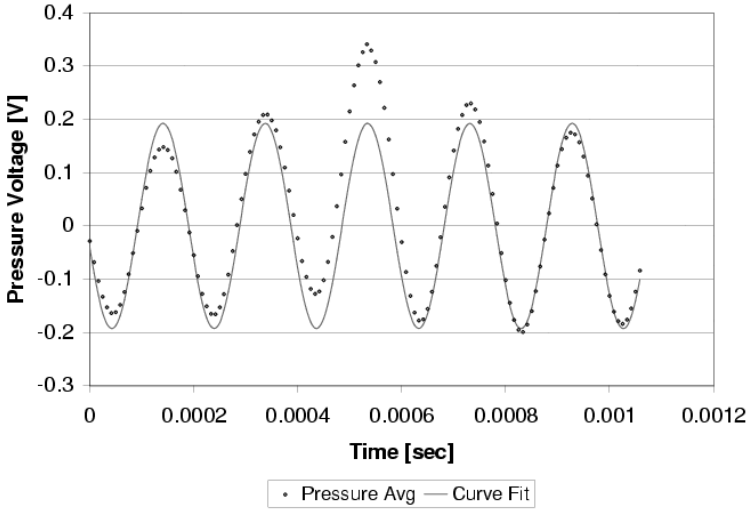

Figure 5.6 Curve-Fit Ensemble Averaged Cylinder Pressure Trace Downstream of Cascade Blades

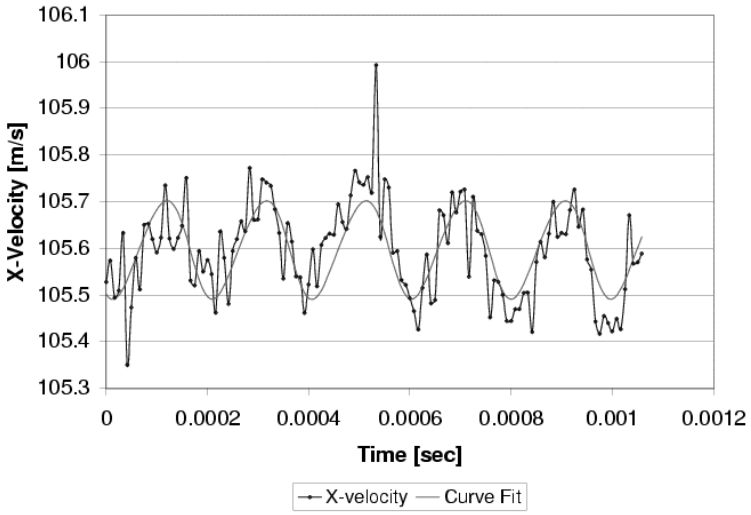

Figure 5.7 Curve-Fit Ensemble Averaged X-Velocity From 70% Chord, Pressure Side

5.6 Velocity Field Over the Blades

Velocity readings for this experiment were taken in increments of 5% chord as close to the surface as could be achieved with the experimental set-up. Measurements were obtained between 50-100% chord, 1/16 inch from the span centerline of the tunnel.

The x-velocity fluctuations for two different turning angles are shown in Fig. 5.8. The velocity fluctuation amplitudes increase towards the trailing edge for both cases, however the amplitudes are less than 1 m/s.

Increasing the turning angle, and thus the loading on the blade, does appear to have a slight impact on the velocity fluctuations towards the rear of the blade, with an increase of 30% of the amplitude at the trailing edge. At locations less than 90% of the chord length, the effects of turning angle are not apparent. In this region, the x-velocity fluctuations are less than 0.2% of the freestream velocity for both turning angles. The noise inherently present prevents any determination of turning angle influences in this region.

The y-velocity fluctuations, shown in Fig. 5.9, for the two turning angles contain the same shape as the x-velocity fluctuations. A large increase in the y-velocity fluctuations, up to 0.45 m/s, is present as the measurement location is increased. The turning angle has the same effect on the y-velocity fluctuations as it did for the x-velocity. The larger turning

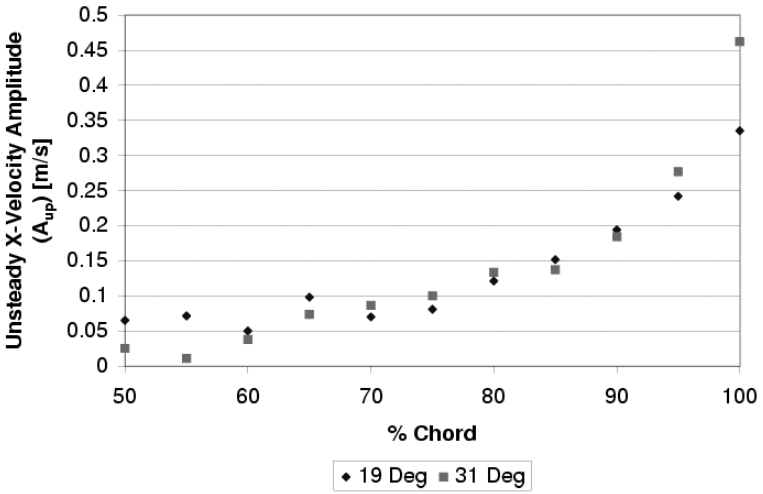

Figure 5.8 X-Velocity Amplitude on Pressure Side of Blade for Different Cascade Inlet Angles

angle produces larger fluctuations, but only at the trailing edge. At all points upstream of 95% chord, the two turning angles create comparable fluctuations.

The results of the velocity measurements on the suction side are far less coherent than those on the pressure side. The separation of the flow in addition to the large destructive interference along the suction side prevented any high amplitude oscillations from being present.

The suction side x-velocity amplitudes for the two different turning angles are shown in Fig. 5.10. As can be seen, no dominant character can be determined although the higher turning angle appears to have amplitudes at the trailing edge that are larger than the points just upstream. No pattern can be seen in the 19-degree turning angle except to notice that the fluctuations towards the trailing edge are lower than those around the midchord.

The y-velocity on the suction side also does not behave in a manner that would allow for characterization of the oscillations to be made, as seen in Fig. 5.11. It can be noted that for both of the turning angles, the fluctuations at the trailing edge are higher than those at 95% chord, indicating a slight increase in the amplitudes towards the trailing edge.

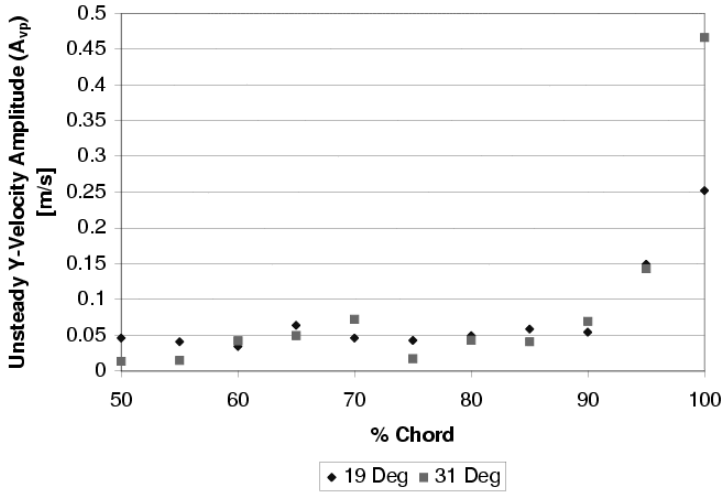

Figure 5.9 Y-Velocity Amplitude on Pressure Side of Blade for Different Cascade Inlet Angles

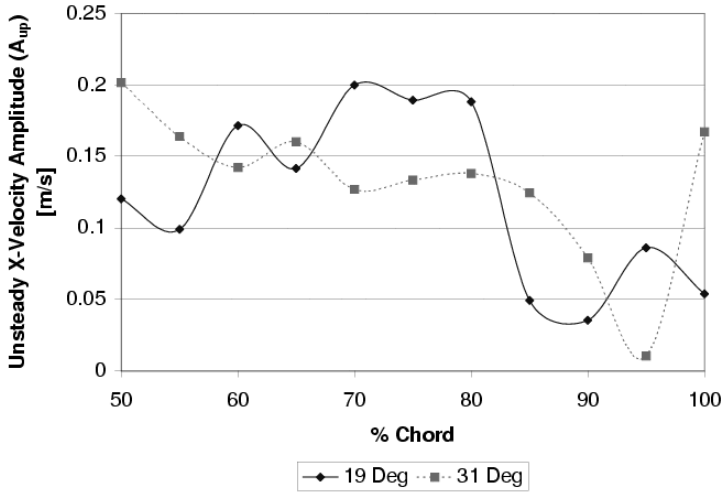

Figure 5.10 X-Velocity Amplitude on Suction Side of Blade for Different Cascade Inlet Angles

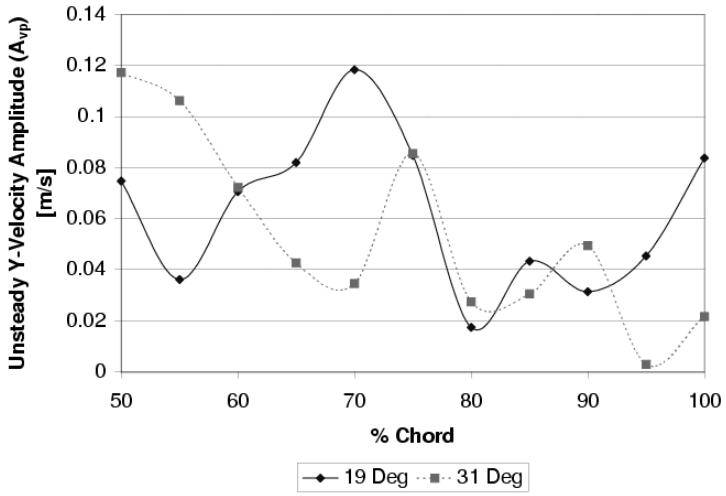

Figure 5.11 Y-Velocity Amplitude on Suction Side of Blade for Different Cascade Inlet Angles

Multiple factors affected the unsteady velocity on the suction side of the blade. The unsteady oscillations from the cylinder array were unable to cleanly propagate through the separated region of the flow. Thus, separation can help reduce the unsteady velocities. CFD results, seen in Appendix E, predicts separation from the blade on the suction side around 75% chord. The separation at 75% chord was verified using oil flow on the suction side of the blade.

Another influence on the suction side unsteady velocity is the destructive interference of the waves from each cylinder. As will be seen in Section 5.11, superposition of the flow predicts that the destructive interference of the unsteady velocities on the suction side will lead to the results similar to those in Figs. 5.10 and 5.11.

5.7 Data Acquisition Trigger Effects

It was noticed during the data collection and reduction processes that the trigger voltage used for the data collection can greatly influence the unsteady amplitude results. The influence of the trigger on the unsteady x-velocity along the pressure side of the blade with an inlet angle of 31° and cylinders 1/2 inch downstream is shown in Fig. 5.12. The

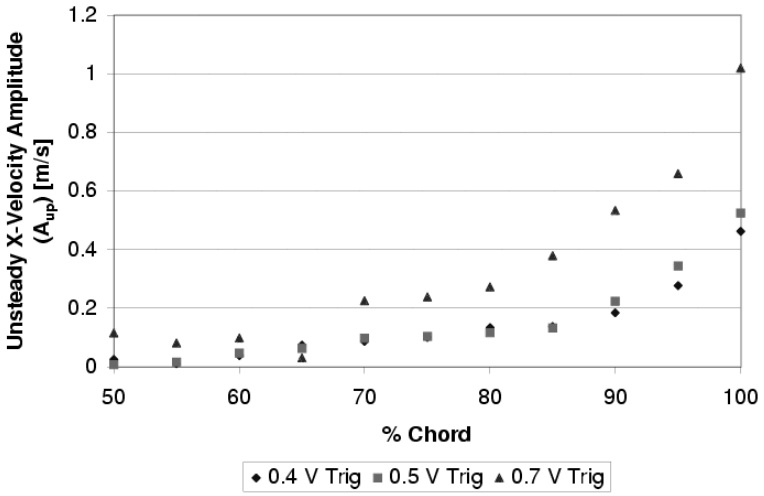

Figure 5.12 X-Velocity Amplitudes on Pressure Side of Blade for Various Data Acquisition Trigger Threshold Values

trigger alters the amplitude of the unsteady velocities, with higher trigger voltages resulting in higher unsteady amplitudes.

The trigger effect on the unsteady velocity field can be explained by examining the ensemble-averaged pressure. A comparison of the ensemble averaged pressure voltages is shown for trigger levels of 0.5 and 0.7 volts in Fig. 5.13. The cylinder shedding captured by the 0.7 volt trigger is much larger than the shedding captured by the lower trigger. The unsteady velocity amplitudes are larger for the higher trigger because the unsteady pressures caused by stronger vortices are being captured, an influence caused by the data collection software.

Collection of a single trace of data was initiated by an up-slope in the pressure voltage that reaches a defined level (the trigger voltage). Once data collection was triggered, logic was performed that ensures this level was reached at the peak of the signal rather than along the upside of the sine wave. This ensured that a vortex that produces a peak of 0.7 volts was be rejected by the trigger at 0.5 volts. Thus, the higher trigger voltage captured the stronger shedding of the cylinder, and the higher unsteady velocities.

The capture of larger amplitudes for higher trigger settings affected this work in two ways. First, this effect provided insight into the flow. As mentioned in Chapter

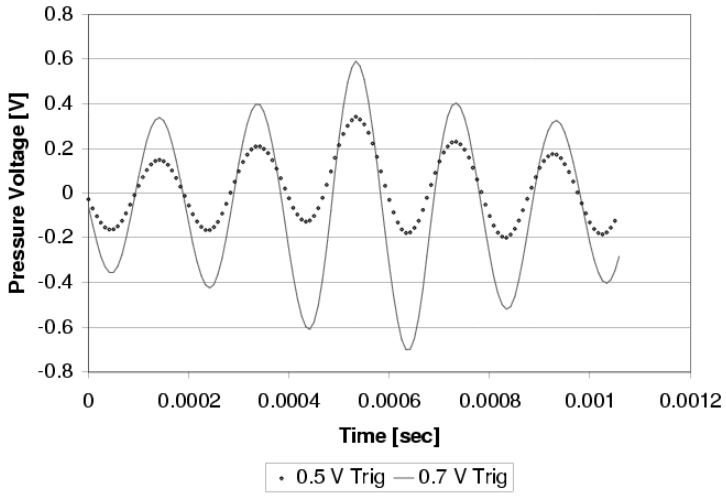

Figure 5.13 Ensemble Averaged Pressure for Various Data Acquisition Trigger Threshold Values

II, Fung [32] showed that the vortex shedding from the cylinder is very unsteady for these Reynolds numbers. The unsteady vortex shedding caused the oscillations present on the blade to contain unsteady amplitudes. The unsteady velocity along the blade was a constant frequency, but contained a highly fluctuating amplitude. The data reduction software captured a trace of the velocities only when the cylinder was shedding with a specific amplitude at the center of the peak. Thus, although the blade contained unsteady velocities with a constant frequency, strongly varying amplitudes were present in the traces.

The second influence on this work was the difficulty of comparing results if the trigger shedding amplitude being captured is not constant. For this reason, a conscious effort was made to ensure that the results presented are taken with identical cylinder pressure levels. Unless noted otherwise, all velocities presented in this chapter were taken with the trigger set at 0.5 volts.

5.8 Cylinder Height Effects

The height of the cylinders above the chord lines was varied in 1/8 inch increments. The different cylinder locations are shown in Fig. 5.14. Changing the cylinder locations was expected to impact the velocity oscillation amplitudes on the blades. From Section

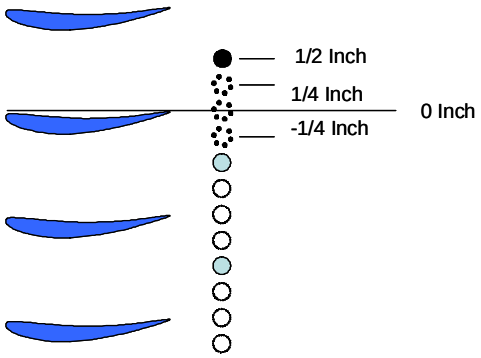

Figure 5.14 Cylinder Height Locations

4.2, the coherence of the cylinder shedding is reduced as the cylinders are moved from the centerline between passages. This reduction in the coherence was expected to cause a reduction in the unsteady velocity amplitudes.

The experimental configuration allowed placement of the cylinders at heights between 1/4 inch below the chord lines up to 1/2 inch above. It was not possible to move the cylinder above 1/2 inch, but the 1-inch blade spacing ensures that most of the possible cylinder locations are observed. The value for the cylinders at 1/4 inch below the chord line is equivalent to 3/4 inch above. The only cylinder array position unable to be measured is 5/8 inch above the centerline.

Figs. 5.15 shows the effects of the cylinder height on the x-velocity fluctuations. The measurement location was at 90% chord on the pressure side of the blade. The cylinder location produces a very strong effect on the cylinder shedding.

For the x-velocity oscillations, the maximum amplitude (A_{up}) occurs at exactly half way between the blades. The amplitudes fall off sharply as the cylinder height is moved from this position. When the cylinder is in the wake from the blade (at height around 0), the unsteadiness in the wake disrupts the vortex shedding from the cylinder and the frequency becomes erratic. Without this single frequency of vortex shedding, the frequency of the unsteady velocities present on the blade will vary greatly. When ensemble averaged, the unsteady velocities (A_{up} and A_{vp}) are greatly reduced because the different frequencies act destructively.

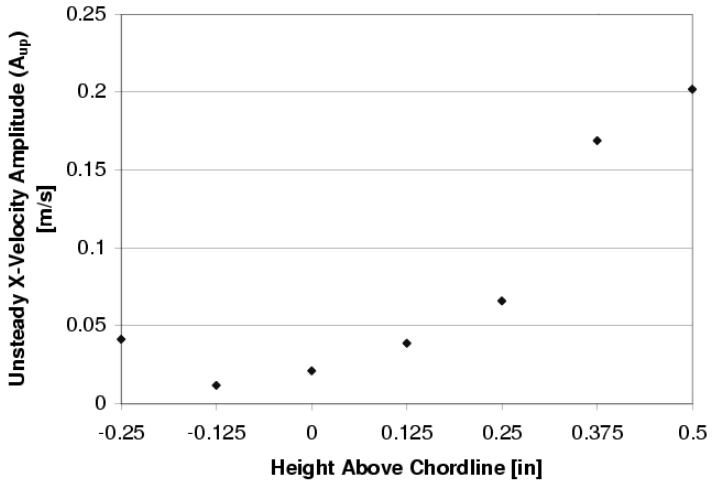

Figure 5.15 X-Velocity Amplitude on Pressure Side of Blade for Different Cylinder Heights Within Passage

In the region between chordlines and the centerline of the passage, the amplitudes drop off quickly as the distance is moved towards the chordline. This is very similar to the results seen in Fig. 4.7 for the shedding coherence of the array. The cylinder height of the minimum unsteady x-velocity amplitude, seen in Fig. 5.15, and the cylinder height for minimum percentage of time of coherent cylinder shedding, seen in Fig 4.7, occur at the same height; thus the percentage of time of cylinder shedding coherence is directly related to the unsteady velocity along the blade.

5.9 Cylinder Downstream Location Effects

CFD results. CFD results were used initially to help predict the effects of placing the cylinders at different downstream locations. A modification of the grid shown in Fig. 5.2 was used for different cylinder locations. The effect of the distance between the cascade and the cylinder array was examined using three different downstream cylinder locations. The distances used were 33% chord (1/2 inch), 67% chord, and 100% chord, as seen in Fig. 5.16. For all locations, the cylinders were located exactly between the chordlines of the blades forming each passage. The expected influence of the cylinder locations would be a decrease in the amplitudes with downstream distance.

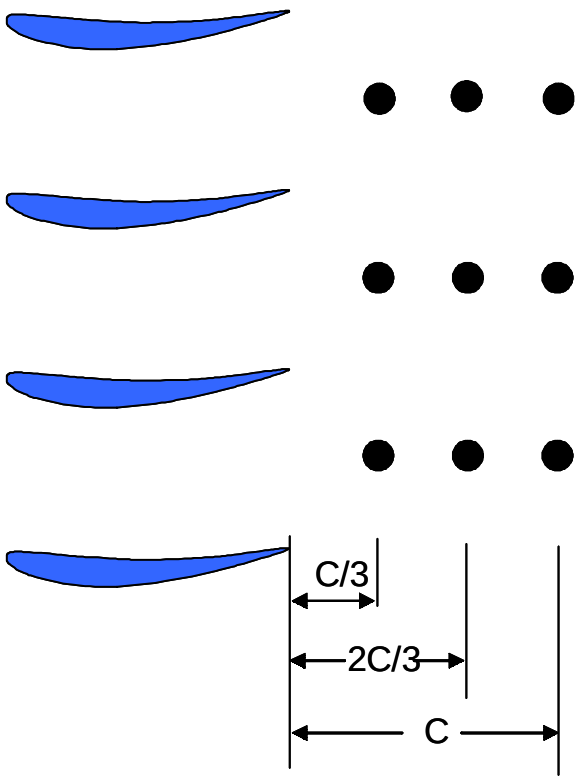

Figure 5.16 Cylinder Downstream Locations

The effect of the downstream location of the cylinder array can be seen in Fig. 5.17. The array of cylinders closest to the blades produced a larger unsteady velocity amplitude on the trailing edge of the blade than the other downstream locations. Moving the cylinder array from 33% chord downstream to 100% chord downstream reduced the unsteady x-velocity amplitude on the trailing edge by 83%. For each of the downstream cylinder array locations, the unsteady x-velocity amplitude increased towards the trailing edge; although the value of the unsteady amplitude at the trailing edge was smaller with the cylinder array located farther downstream.

Experimental results. The CFD results predicted approximately a 40% decrease in the unsteady x-velocity amplitude when the cylinders were moved from 1/3 to 2/3 chord downstream. Experimental results were obtained with cylinders at these two downstream distances. Like the CFD, the cylinders for both downstream locations were kept at a height (y-direction) half way between the blade chordlines.

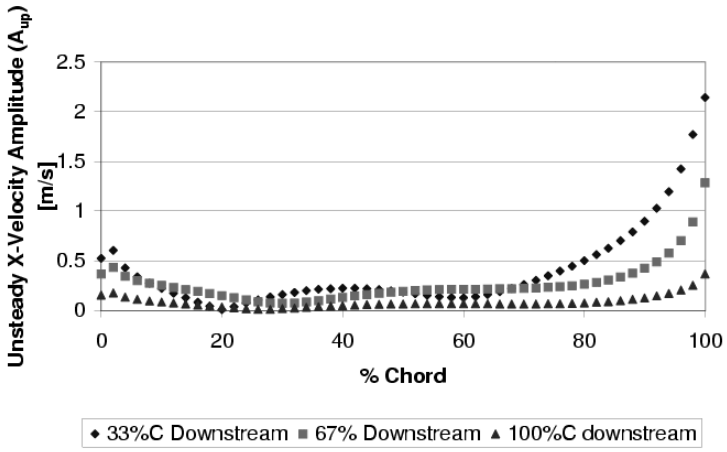

Figure 5.17 CFD X-Velocity Amplitude on Pressure Side of Blade for Multiple Downstream Cylinder Locations

The pressure side unsteady x-velocity amplitude for two different cylinder locations are shown in Fig. 5.18. The downstream location of the cylinder affects the unsteady x-velocity amplitudes strongly at the trailing edge. At measurement locations forward of 90% chord, the effect of downstream cylinder distance is not noticeable.

The results from the experiment shows approximately a 40% reduction in the unsteady x-amplitude at the blade trailing edge by moving the cylinder downstream. The percentage of the unsteady amplitude reduction for both the experiment and the CFD are in agreement. Thus, although the magnitude of the unsteady x-velocity predicted by the CFD is larger than for the experiment, the percentage reduction of the unsteady velocity by moving the cylinder downstream was accurately predicted by the CFD.

The pressure side unsteady y-velocity amplitude for the same cylinder downstream locations is shown in Fig. 5.19. Like the x-velocity fluctuations, the cylinder location affects the y-velocity amplitude at the trailing edge of the blade. However, forward of 95% chord, the unsteady y-velocity amplitude is not altered by the cylinder downstream location.

The reduction in the unsteady x- and y-velocity amplitudes with downstream cylinder distance can be attributed to the increased distance between the forcing and the blades. The propagating waves emanating from a cylinder are reduced with upstream distance. The closer cylinder locations to the blade will produce larger unsteady amplitudes.

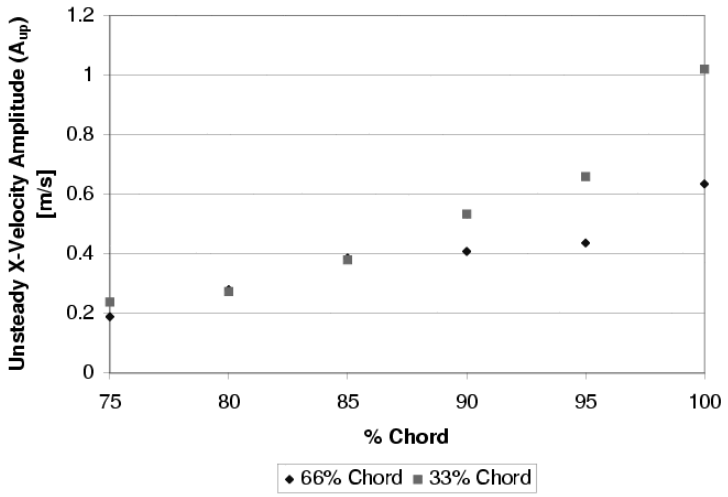

Figure 5.18 X-Velocity Amplitude on Pressure Side of Blade for Cylinders Located 1/3 and 2/3 Chord Downstream

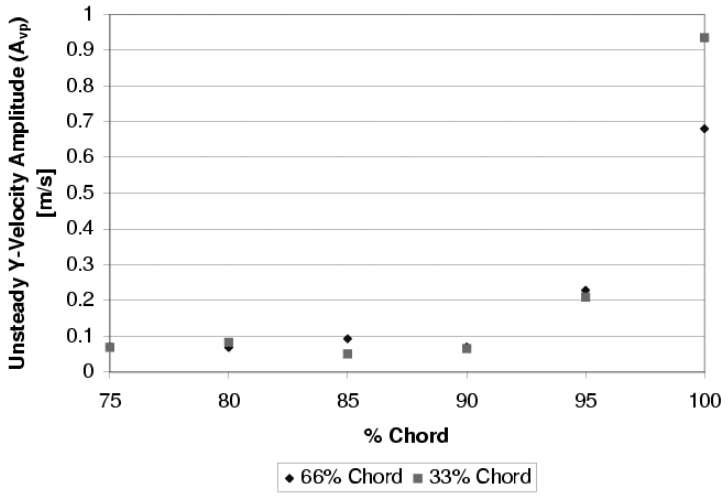

Figure 5.19 Y-Velocity Amplitude on Pressure Side of Blade for Cylinders Located 1/3 and 2/3 Chord Downstream

The results presented in Figs. 5.18 and 5.19 were acquired using a trigger voltage of 0.7. The amplitude of cylinder oscillations captured in these figures is larger than for the remainder of the work presented in this chapter, thus the magnitude of the unsteady velocities are larger.

5.10 Freestream Velocity Effects

The effect of the freestream velocity on the flow is another influence examined. The pressure histograms shown previously indicate that increasing the velocity creates a larger percentage of time of coherent cylinder shedding. For this reason, the velocity oscillations were expected to increase with increasing freestream velocity.

CFD results. CFD results were generated for three different inlet velocities in order to see the effects of increased velocity. An incompressible solver was used for each of the three cases to ensure an equivalent comparison, although the highest velocity case (150 m/s) would certainly contain compressible effects.

The effect of the inlet velocity magnitude on the velocity fluctuations can be seen in Fig. 5.20. On the pressure side of the blade, increasing the inlet velocity increases the velocity amplitudes at the trailing edge of the blade. The general shape of the curve remains approximately the same with increasing amplitudes at the leading and trailing edge of the blade.

Increasing the velocity from 100 m/s to 125 m/s generated almost three times the unsteady x-velocity amplitude at the trailing edge. The effect of increasing the velocity is even more pronounced at 90% chord where an increase of 25% velocity increased the unsteady x-velocity amplitudes over 4.4 times.

Experimental results. Unsteady velocity amplitudes were measured for various freestream velocities. The x-velocity oscillations, shown in Fig. 5.21, were taken at 90% chord on the pressure side for various freestream velocities. For these measurements, the cylinders were located at the 1/2 inch height above the chord lines.

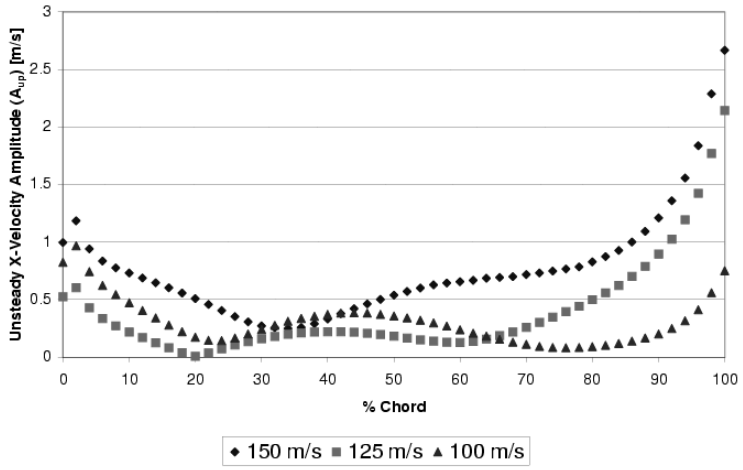

Figure 5.20 CFD X-Velocity Amplitude on Pressure Side of Blade for Multiple Freestream Velocities

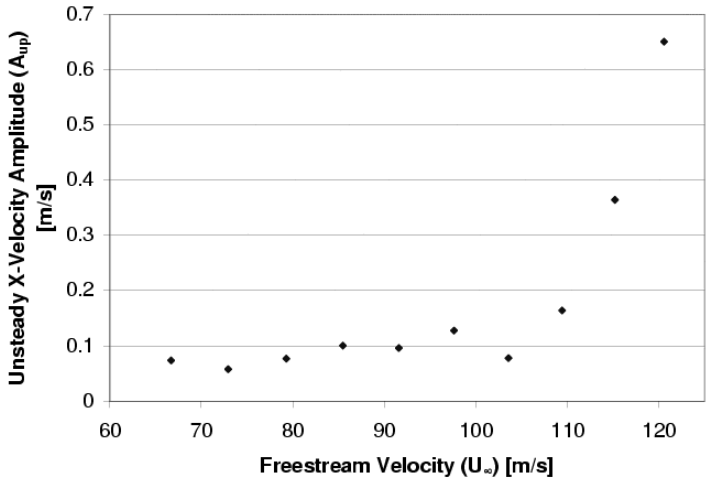

Figure 5.21 X-Velocity Amplitudes at 90% Chord, Pressure Side for Various Reynolds Numbers

A very strong influence of the freestream velocity on the oscillation amplitude can be seen. For freestream velocities below 105 m/s, no significant fluctuations are present in the flow field because the cylinders are shedding in a more random fashion, as seen in Fig. 4.6.

As the freestream velocity is increased above 105 m/s, the amplitudes begin to rise quickly. The largest measured oscillations occurred at the highest velocity used in this experiment. A reasonable assumption from Fig. 5.21 would be that the amplitudes would continue to increase at a high rate as the velocity is increased.

The increase of 25% in the velocity (from 97 m/s to 121 m/s) caused a fivefold increase in the unsteady x-velocity amplitudes at the 90% chord location. Two different effects influence the increasing unsteady velocity amplitudes: the increased magnitude of the vortices shed at higher velocities and the increased percentage of time of coherence.

The increased magnitude of the vortices shed causing the increased unsteady x-velocity amplitudes is predicted by the CFD results. Increasing the freestream velocity increases strength of the vortices shed from the cylinder and thus the unsteady pressure on the cylinder. This increased unsteady pressure from the cylinders propagates upstream and is seen as increased unsteady velocities on the blades.

The increase in the percentage of time of coherence between cylinders increases the amplitudes of the unsteady velocities. When the cylinders are shedding in a random fashion, the unsteady velocity effects from the cylinders not used for triggering are random and reduced or eliminated when ensemble averaged. As the percentage of time of coherent shedding is increased, more of the 500 total samples contain the results of coherent shedding and the overall measured unsteady velocity amplitudes are increased when the samples are ensemble averaged.

5.11 Superposition of Results

The upstream effects from the cylinders produce potential-like waves that propagate upstream. One of the benefits of potential flow theory is the linearity present in the

equations, thus superposition can be used to combine elementary flows into a more complex solution.

Superposition was used to create the unsteady flow over a cascade blade located upstream of an array of cylinders through the use of only one cylinder. The main benefit of using superposition rather than an array is that the desired phase between individual cylinders can be forced through the use of a phase shift from individual cylinder results.

The solution to the superposed unsteady velocities over a blade can be developed by summing the sinusoidal velocity fits generated from each individual cylinder. The first step in the summation process is to determine the desired shedding phase of each cylinder. This phase is generated by adding an additional phase shift term to the cylinder phase shift as:

$$\phi_{i,s} = \phi_{i,desired} - \phi_{i,pp} \tag{5.9}$$

where i is the cylinder number, $\phi_{i,s}$ is the required additional shift, $\phi_{i,pp}$ is the phase shift generated from the data reduction for the pressure signal, and $\phi_{i,desired}$ is the desired cylinder phase.

Once the required shift is known, the summation of the velocity curve fits is performed. The summation requires the computation of two parameters. The first is

$$B = \sum_{i=1}^{n} A_{i,up} \cos(\phi_{i,up} + \phi_{i,s}) \tag{5.10}$$

where $A_{i,up}$ is the amplitude of the unsteady x-velocity for each cylinder, n is the total number of cylinders, and $\phi_{i,up}$ is the phase for the unsteady x-velocity.

The second parameter is calculated by

$$C = \sum_{i=1}^{n} A_{i,up} \sin(\phi_{i,up} + \phi_{i,s}) \tag{5.11}$$

Once B and C are known, the superposed amplitude can be calculated by

$$A_{up} = \sqrt{B^2 + C^2} \tag{5.12}$$

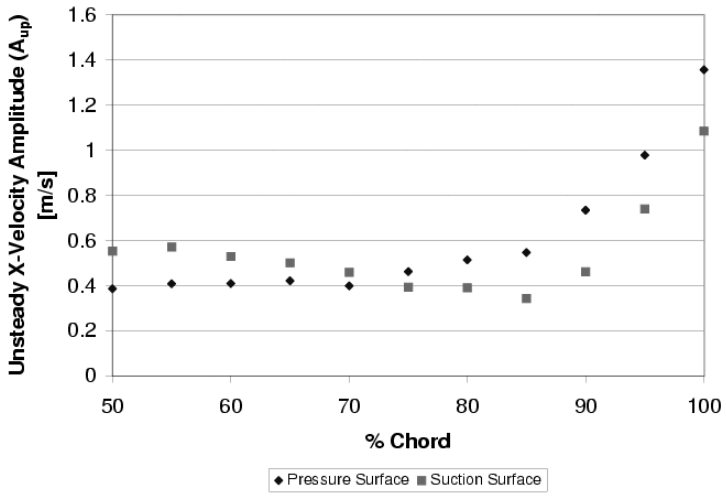

Figure 5.22 Superposition Maximum X-Velocity Amplitude Over Cascade Blade

and the phase is

$$\phi_{up} = \tan^{-1}\left(\frac{C}{B}\right) \tag{5.13}$$

Through the use of superposition, the maximum possible amplitude can be determined. This maximum amplitude can only be created when the unsteady velocities at a given point have a phase such that the peaks in the unsteady velocities produced by each cylinder occur at the same time. For this case, the combined unsteady velocity amplitude becomes simply the summation of the unsteady velocity amplitudes generated by each cylinder at a given point. The maximum amplitude is shown in Fig. 5.22 for both the pressure and suction sides of the blade.

The results from the superposed velocity amplitudes on the pressure side display the same trend as the unsteady velocities caused by the cylinder array. The suction surface unsteady velocities also exhibit this pattern of increasing magnitude towards the trailing edge for the superposed results. Superposition predicts that a coherent unsteady velocity amplitude is present through the separation region on the suction side of the blade, and the destructive interference of the potential-like waves is the main cause of the lack of amplitude rise in the cylinder array shown in Fig. 5.10.

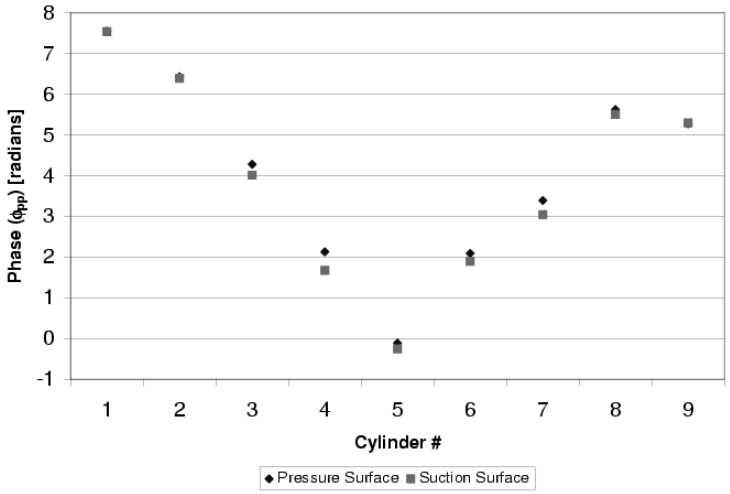

Figure 5.23 Superposition Cylinder Phase Required to Generate Maximum X-Velocity Amplitude on Blade

The maximum amplitude possible, shown in Fig. 5.22, corresponds to a specific phase relation between each of the cylinders, as shown in Fig. 5.23. The required phase relation agrees with what is expected. The cylinders farther from the blade must shed a vortex earlier than the cylinder in the centerline for the unsteady velocities to be in phase along the blade. This causes the required phase relation between the blades to be in a "V" pattern, as seen in Fig. 5.23. Although this pattern produces the maximum amplitude on the blade where the velocity measurements were made, the amplitude of the velocities along the other blades would not be maximized from this phase relation.

The two different coherent cylinder shedding relationships, discussed in Chapter III, are synchronous and asynchronous shedding. Both of these methods of coherent shedding can be simulated through the use of superposition of the results. A comparison of the unsteady x-velocity amplitudes created by the two coherent shedding structures, along with the maximum superposed amplitudes, is shown in Fig. 5.24. As can be seen, both the synchronized and asynchronized results contain a large amount of destructive interference in the unsteady velocity amplitudes. The unsteady amplitudes at the trailing edge for both cases are only a fraction of the maximum amplitude created if the cylinders where shedding according to Fig. 5.23. Both the asynchronous and the maximum amplitude shedding produce amplitudes which increase with chord distance downstream of 85% chord.

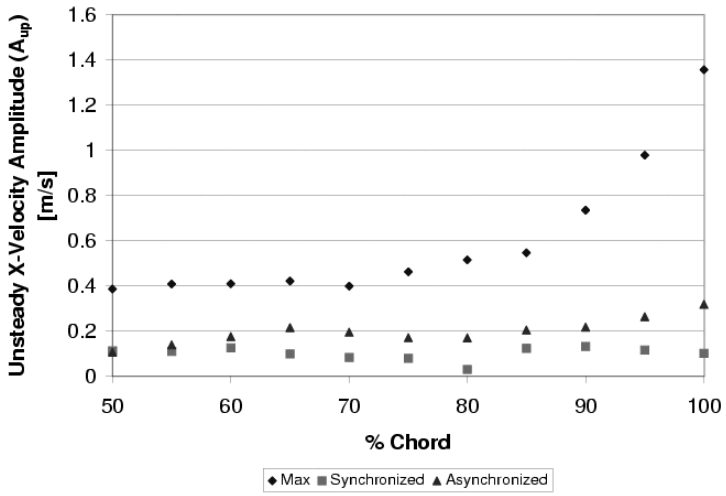

Figure 5.24 Superposition X-Velocity Amplitude on Pressure Side of Blade for Synchronous and Asynchronous Cylinder Shedding

This trend is not present in the synchronized case. The destructive interference from the synchronous cylinder shedding prevents the higher unsteady velocity amplitudes at the trailing edge of the blade.

The effects of the destructive wave interference is even more apparent in the unsteady x-velocity amplitudes present on the suction side of the blade, as seen in Fig. 5.25. Both the synchronous and asynchronous shedding produce amplitudes on the suction side that contain no readily discernible patterns. Initially, it was believed that this was caused solely by the separation of the flow along the suction surface; however, the maximum amplitude results display that each of the cylinders produces an unsteady amplitude that increases in the separation area aft of 75% chord. The increase of amplitudes towards the trailing edge is eliminated by the destructive interference of the cylinder array.

A comparison of the unsteady x-velocity amplitudes generated by asymmetric shedding created through superposition can be compared to the experimental amplitudes collected from the cylinder array, as seen if Fig. 5.26. As can be seen, the superposition results fairly accurately predict the experimental array data aft of 80% chord. In front of this region, the amplitude of the fluctuations are relatively small, as seen in the array results, and superposition results predict a larger amplitude than produced by the array.

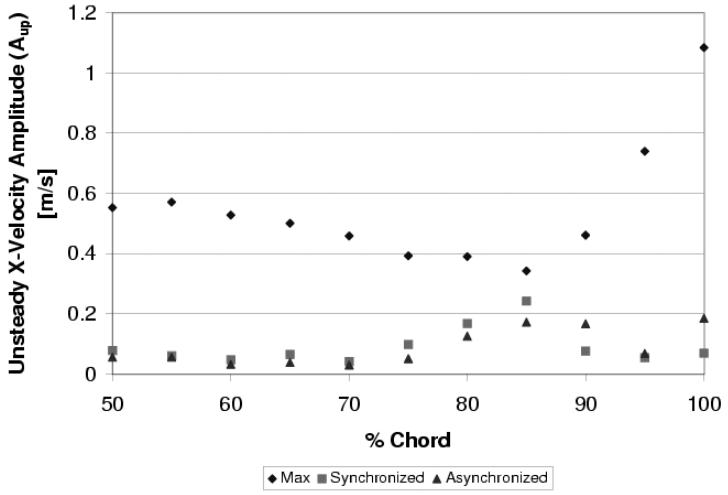

Figure 5.25 Superposition X-Velocity Amplitude on Suction Side of Blade for Synchronous and Asynchronous Cylinder Shedding

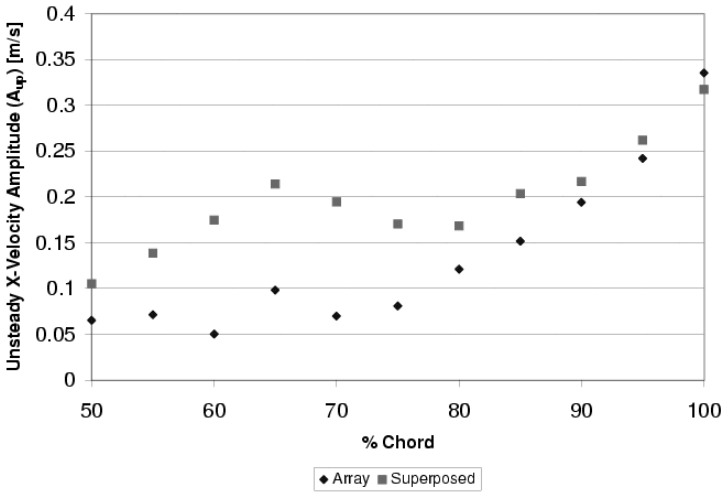

Figure 5.26 Superposition and Experimental Array X-Velocity on Pressure Side of Blade

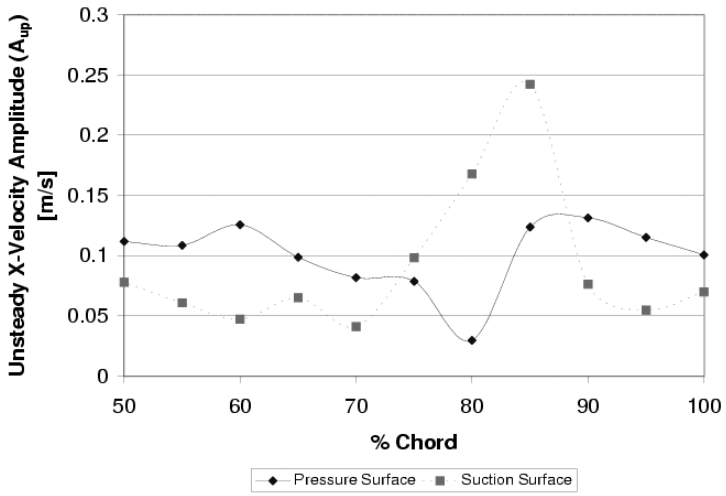

Figure 5.27 Super Position X-Velocity Amplitude Along Blade for Synchronous Cylinder Shedding

Errors in the superposition curve-fit for the regions of small fluctuations are compounded when the results are summed, causing superposition results to predict larger amplitudes.

In an actual engine, each of the blades passes through wakes from upstream blades almost simultaneously. This can be modeled through the use of the cylinders shedding synchronously. The results of the unsteady x-velocity amplitudes for the pressure and suction surface of the blade are shown in Fig. 5.27. The amplitude results from the synchronous case are very different from the other two results shown in Fig. 5.24. The unsteady amplitudes on the pressure side of the blade never exhibit a trend of increasing amplitudes towards the trailing edge of the blade, rather the results are fairly insensitive to chord location. The destructive interference of the effects of each cylinder cause the unsteady velocities to be insensitive to the chord of the blade.

A trend in the suction side unsteady x-velocity caused by the synchronous shedding is noticeable in Fig. 5.27. The amplitude increases with chord position beginning at 70% chord and continuing until 85% chord. Beyond 85% chord, the destructive interference of the waves causes the amplitudes to be reduced to the levels seen around mid chord.

Superposition can be used to simulate the unsteady velocity field forced by a downstream array of cylinders. In regions where the unsteady fluctuations are small, the errors

are compounded through superposition; however, the flow field can be fairly well described when the amplitudes of the fluctuations are large enough.

5.12 Chapter Summary

The unsteady velocity amplitudes were measured over a blade located in a cascade. The unsteady x- and y-velocities were largest at the trailing edge of the blade and were reduced with upstream distance on the pressure surface of the blade. The separation of the flow at 75% chord and destructive interference of the waves produced a flow around the suction side that did not exhibit any discernible trends. Any effects that increase the percentage of time of coherence of the cylinders is seen as an increase in the ensemble averaged velocities over the blade. Superposition provided a fairly accurate model of the influences of the cylinder array in the region of large unsteady amplitudes toward the trailing edge of the blade.

VI. Correlation of Pressure and Velocity in Unsteady Flow Field

The increased unsteady velocities towards the trailing edge of a blade when forced by upstream propagating waves was seen in Chapter V. The unsteady pressures at the trailing edge of the blade are the desired parameters for HCF effects. If the unsteady pressures are known, then the unsteady force acting on the blade can be calculated. This chapter provides a look at determining the pressure from the measured unsteady velocity field.

6.1 Unsteady Bernoulli Equation

From White [31], the unsteady Bernoulli equation for unsteady incompressible flow is

$$\rho\frac{\partial\phi}{\partial t} + P + \frac{1}{2}\rho V^2 + \rho g z = const \tag{6.1}$$

where g is gravity acting in the z-direction. Assumptions for deriving Eq. (6.1) include an irrotational, incompressible flows with constant viscosity [31]. When gravity is neglected from Eq. (6.1), the equation becomes

$$\rho\frac{\partial\phi}{\partial t} + P + \frac{1}{2}\rho V^2 = const \tag{6.2}$$

For the steady state problem, the first term of Eq. (6.2) is eliminated, and the equation reduces to the familiar form of Bernoulli's equation

$$P + \frac{1}{2}\rho V^2 = P_o \tag{6.3}$$

For the case of a steady flow, the pressure can easily be calculated for any point where the velocity is known, as long as at least one point exists along the streamline where both the pressure and velocity are known, generally taken from far-field conditions. Calculating the pressure from the velocity in an unsteady flow is far more complex because the change of the velocity potential must be known for all time. Because each velocity component at a given point is defined as the partial derivative of the velocity potential with respect to the component direction, a time accurate history of the velocity is necessary at surrounding points in all directions for the time derivative of the velocity potential to be calculated.

6.2 Computational Results

Unsteady CFD results can be used to determine the relative importance of the time derivative of the velocity potential in Eq. (6.2). Unlike the experimental results, both the velocity and pressure are known at a particular point for the CFD.

If the flow field is generally uninfluenced by the time derivative of the velocity potential, the pressure calculated using Eq. (6.3) should match the pressure provided by the computer simulation. The importance of $\frac{\partial \phi}{\partial t}$ from Eq. (6.2) on the results can be determined by calculating the pressure by inserting the CFD velocities in Eq. (6.3) and comparing the calculated pressure with the CFD pressure results.

Freestream CFD flows. The pressures were calculated for each of the three CFD cases without blades: random, synchronous, and asynchronous shedding. Points were examined at two different upstream locations of one and three inches at a height of one inch above the tunnel centerline. The error was determined as

$$\epsilon = \| \left(P_{cfd} - P_{calc} \right) \|$$

and then was scaled to give a percent error. The scaling was performed using two different methods of normalizing. The first was to use the average pressure at the given point. Using this value would show how accurately the overall pressure would be estimated by using Eq. (6.3) at a given time. The second choice for normalization was to use the peak-to-peak value of the pressure. Using this method would show the errors in capturing the fluctuations as a percentage of the fluctuations. The errors at one inch upstream are shown in Table 6.1. The errors for three inches upstream follow the same trends.

CFD Case	% Error Total	% Error Peak-to-Peak
Random	1.12	50.34
Synchronous	0.33	53.37
Asynchronous	1.48	50.47

Table 6.1 Maximum Percentage Error in Pressure Calculation With Bernoulli Eqn Calculated 1 Inch Upstream

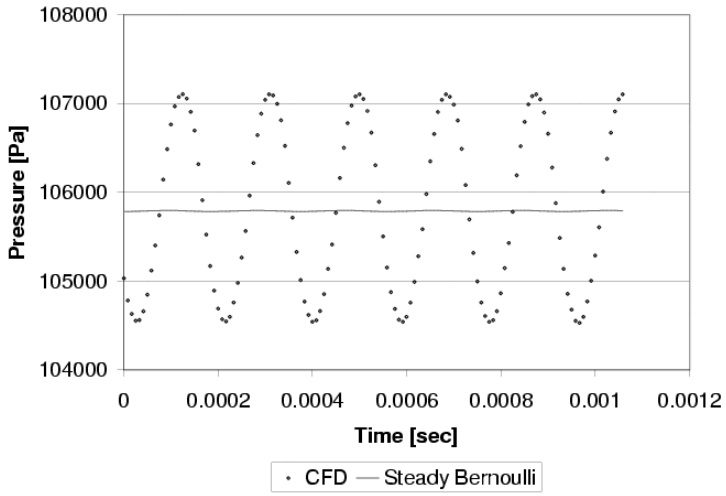

Figure 6.1 Steady Bernoulli Equation Predicted Pressure Trace for Random Shedding at 3 Inches Upstream and 1/2 Inch Above Centerline

As can be seen from Table 6.1, the use of the steady state Bernoulli Equation gives fairly good results when examining the overall time history of pressure, with a maximum error of less than 1.5% for all of the cases. The use of Eq. (6.3) for the estimation of the amplitude of the fluctuations does a very poor job of predicting the pressure peaks, with errors greater than 50% of the peak-to-peak pressure fluctuations.

An example of the poor capturing of the pressure fluctuations can be seen in Fig. 6.1. Eq. (6.3) predicts only very small fluctuations in the pressure, instead of the far larger results seen.

It can be concluded from the results in Table 6.1 that the first term of the unsteady Bernoulli equation, Eq. (6.2), is a very important part of the solution. This is not surprising because the fluctuations in both the velocity and pressure are caused by the upstream propagating oscillating potential waves. By definition, these potential waves will have a large time derivative component.

The pressure can only be calculated from the velocity if the unsteady velocity potential is known. In order to know the unsteady velocity potential, the entire flow around the desired point must be known for multiple instances in time.

Case	% Error at 2% Chord	% Error at 100% Chord
150 m/s - pressure side	57.45	38.14
100 m/s - pressure side	48.65	38.48
150 m/s - suction side	40.33	51.99
100 m/s - suction side	57.76	52.62

Table 6.2 Peak-to-Preak Error for Cascade Flow

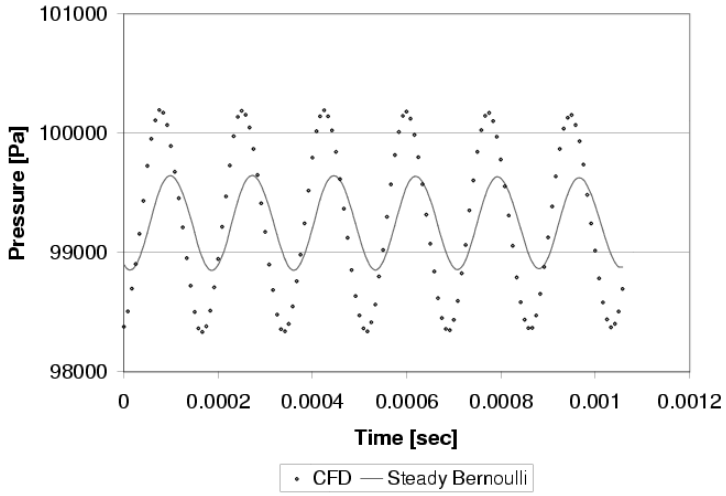

Figure 6.2 Bernoulli Equation Predicted Pressure Trace at 100% Chord, Pressure Side of Blade With 150 m/s Freestream Velocity

Cascade flows. The importance of the time derivative of the velocity potential was also examined for the cascade flows. The results once again showed a very large dependence of the flow on $\frac{\partial \phi}{\partial t}$. The percent errors based on the peak-to-peak values are shown in Table 6.2.

Once again, the errors of assuming a quasi-steady state solution by using Eq. (6.3) is very large, with maximum errors greater than 35% for all cases. A plot of the CFD pressure and the calculated pressure for 100% chord on the pressure side at 150 m/s is shown in Fig. 6.2. Unlike the calculated results from Fig. 6.1, the sinusoidal characteristic of the calculated pressure is clearly noticeable in Fig. 6.2.

A slight phase difference exists between the CFD pressure and the pressure calculated by Eq. (6.3). Any phase difference between the CFD pressure and velocity magnitude can be seen by placing both on a plot, as seen in Fig. 6.3. Quasi-steady state calculations using

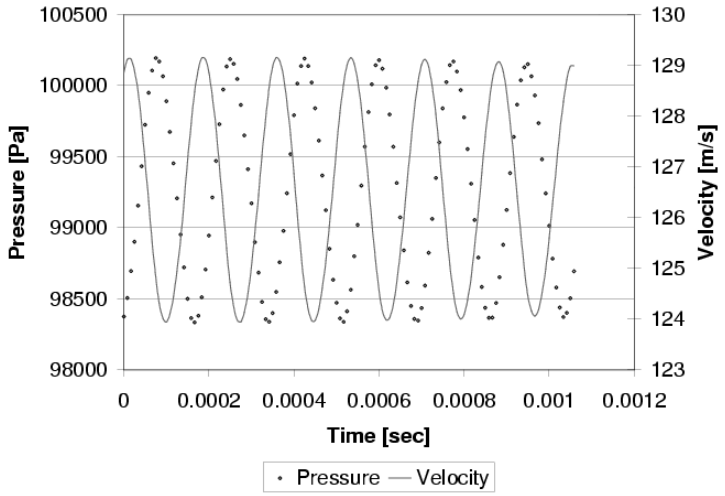

Figure 6.3 CFD Pressure and Velocity at 100% Chord, Pressure Side of Blade With 150 m/s Freestream Velocity

Eq. (6.3) suggest that the pressure and velocity should be exactly out of phase, with the pressure falling when the velocity is rising. However, the time derivative of the unsteady potential provides an influence large enough to allow for the two to be slightly out of phase.

Impact. From the computational results, the conclusion can be obtained that it is not possible to calculate the pressure field with velocity measurements in only one spatial direction. If enough time accurate velocity measurements were made in a grid, the velocity potential could possibly be calculated and $\frac{\partial \phi}{\partial t}$ could be known. Because the pressure cannot be estimated from the velocity flow field along a blade, the pressure trends present in the tunnel must be inferred by the trends present in the CFD data.

6.3 Unsteady Velocity and Pressure Trends

A comparison of the CFD velocity and pressure can be used in an attempt to predict the unsteady pressure in the experimental case. The CFD results were compared for the case best matching the baseline experiment with 125 m/s inlet velocity and cylinders located 1/2 inch downstream.

A comparison of the primary frequency amplitudes for both the pressure and the velocity on the pressure side of the blade is shown in Fig. 6.4. The trends of the unsteady

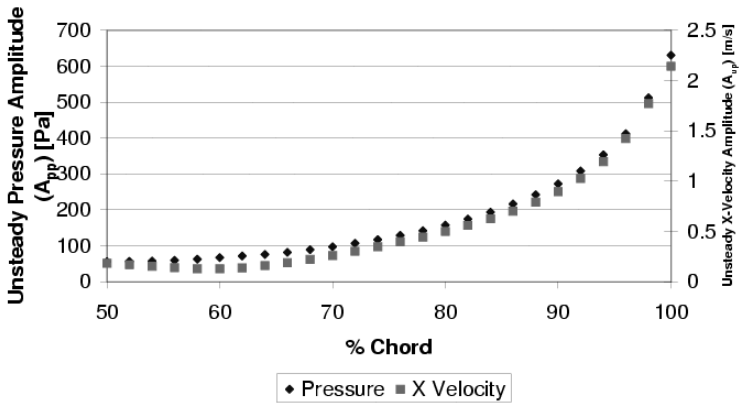

Figure 6.4 CFD Unsteady Pressure and X-Velocity Amplitudes on Pressure Side of Blade for 150 m/s Freestream Velocity

pressure and velocity amplitude match almost exactly. Thus, along the pressure side of the blade, the unsteady pressure has the largest amplitude at the trailing edge and is reduced along the chord distance upstream.

A phase diagram can be used to see if the pressure and velocity are in phase. A plot of the phases for the amplitude shown in Fig. 6.4 can be seen in Fig. 6.5. In the aft 30% of the chord, the phase difference between the velocity and pressure is fairly constant at just under 2 radians. If the pressure and velocity were related by Eq. (6.3), then the phase difference would be exactly π. The only way for the phase difference to be less than π is when $\frac{\partial \phi}{\partial t}$ is large enough to influence the signals.

6.4 Discussion of Expected Pressure Field in the Cascade

As mentioned previously, the pressure cannot be calculated due to the large influence of the time derivative of the velocity potential. Because this is the case, the possible pressure can only be inferred from the CFD results.

The experimental velocities seem to follow the same trend as the CFD results, although the CFD results have a larger magnitude. The primary influence in this discrepancy is due to the inherent unsteadiness in the experimental flow. Although the cylinders present in the flow are, on average, shedding in phase, the use of ensemble averaging will inherently

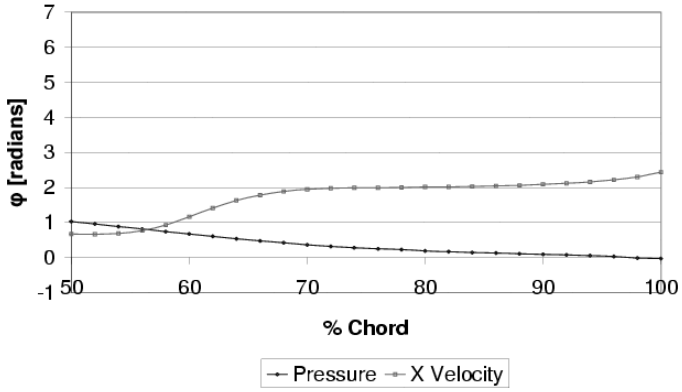

Figure 6.5 CFD Phase of Unsteady Pressure and Velocity on Pressure Side of Blade for 150 m/s Freestream Velocity

cause the amplitude to be slightly reduced. Because the cylinder is only shedding in the proper phase approximately 30% of the time, the influence of that cylinder will be reduced in the ensemble averaged results. Additionally, the magnitude of the shedding from the cylinder is highly unstable. The expected trend of the experimental pressure would be to have a maximum pressure at the trailing edge of the blade, which is reducing along the blade chord upstream in a fashion in scale with the velocity data.

6.5 Chapter Summary

The unsteady pressure present on the blades in the cascade cannot be calculated from the unsteady velocity results. The unsteady velocity potential created by the cylinders creates an effect on the pressure far exceeding the effects of only the velocity oscillations. Without knowledge of the entire flow around a point, the pressure cannot be calculated from the experimental results.

VII. Summary and Conclusions

This dissertation presented the effects of the propagation of pressure and velocity disturbances upstream of cylinders that were used to simulate fluctuations created by downstream components present in turbine engines. In rotating machinery, these perturbations originate from the fluctuating bound vorticity generated as the incidence rises and falls during blade transit through wakes created by an upstream row [10]. These high frequency oscillations of pressure and velocity can be seen over the upstream blades and can possibly lead to high cycle fatigue caused by the unsteady load on the blade [25]. In this work, the unsteady forcing was created by the von Karman shedding from a row of cylinders placed either within a freestream flow or 33% to 100% chord lengths downstream of blades.

The interaction of the vortex shedding between cylinders was examined. This work was the first work to look at determining the conditions required to generate coherent shedding from an array of cylinders without altering the spacing. All of the previous work (such as the work by Ohya, et al. [47]) was performed by altering the spacing between the cylinders and examining the impact on the coherence. This work showed that placing a wake upstream effectively lengthened the maximum spacing for coherence between cylinders. The freestream velocity was an important influence on the standard deviation of the mean relative cylinder shedding.

The effect of the downstream cylinders on the unsteady velocity field over a blade was measured for the first time. (The blades used for this work were the midspan coordinates from a stator vane in a Garrett F-109 turbofan.) Previous results by Fabian [13] have all focused on the unsteady pressure along the blade surface. The unsteady velocity amplitudes were maximum at the trailing edge of the blade and were mostly non-existent forward of 75% chord. CFD results indicate that the amplitude of the pressure fluctuations is largest in the cascade where the velocity amplitudes are largest. If this trend holds experimentally, the unsteady pressures towards the trailing edge could be larger than elsewhere on the blade.

The use of superposition of unsteady amplitudes upstream of a single cylinder produced results in which the predicted unsteady velocities towards the trailing edge compared

favorably to the experimental results from the cylinder array. Toward the trailing edge of the blade, where the largest fluctuations are present, the use of superposition predicted the unsteady velocities generated by the cylinder array. This work was the first to show the effectiveness of superposition for this flow field.

The flow field was modeled two-dimensionally, using CFD, to obtain a better understanding of the flow physics involved and the interaction of the array of cylinders on the blades. This work contains the first CFD simulation of the flow containing a cascade with a downstream array of cylinders. The CFD results showed increasing unsteady velocity and pressures towards the trailing edge of the blade. Although the magnitudes of the CFD did not match the experimental results, the effects of configuration changes were predicted by the CFD.

Analysis of these unsteady data has added to the understanding of the shedding response of an array of cylinders along with the forced response that such an array creates on upstream blades. A more detailed look at these results and conclusions follows.

7.1 Single Cylinder Results

The unsteady velocity field generated upstream of a single cylinder was measured. The phase of the unsteady amplitudes was used to verify that the unsteady fluctuations were propagating upstream at acoustic speed. The amplitude of the unsteady flow was not accurately modeled by a simple potential model or CFD, indicating that tunnel effects were a major influence. The tunnel effects include non-uniform spanwise shedding of the cylinder, non-constant vortex shedding amplitude, and unsteady tunnel interactions.

Three-dimensional propagation of the waves will also impact the results due to non-uniform phase distribution of the von Karman vortex street along the span of the cylinder. This effect in addition to the reflections from the side walls will also lead to a response that cannot be predicted from the simple potential model suggested by Fabian and Jumper [24] and extended by Hopper [28].

The upstream unsteady velocity amplitude was expected to drop off as $\frac{1}{r}$ where r is the distance from the cylinder. The actual fall off of the unsteady amplitude was much

less than $\frac{1}{r}$, indicating that the unsteady velocity fluctuations were not acting in a manner described by potential flow theory, a result seen by Hopper [28] and Falk et al. [25].

7.2 Multiple Cylinder Results in a Freestream Flow

An array of cylinders was placed in a freestream flow with a spacing of 0.8 inches between centerlines. As predicted by Ohya et al. [47], the spacing between cylinders was too large for any interactions of the vortex shedding between cylinders to be present. The vortex shedding from each cylinder was random compared to the remaining cylinders.

A viscous, incompressible CFD model was created in Fluent for the array of cylinders in an attempt to understand the interactions between the cylinders. Like the experimental results, the relative phase of the cylinder shedding between the cylinders was random for a spacing of 0.8 inches between cylinders placed in a freestream flow.

By creating a periodic square-toothed inlet flow roughly resembling wakes, synchronous shedding of the cylinders occurred in CFD. A doubling of the spatial period of the square wave inlet condition in CFD, or halving the number of wakes, created an asynchronous pattern in the cylinder shedding. The existence of a velocity inlet differential between the top and bottom surfaces of each cylinder caused the cylinders to shed vortices in a coherent fashion for the CFD results. These simulation results led to the conclusion that placing cylinders downstream of a series of shear layers, such as created by blades, could result in coherent shedding between the cylinders.

CFD results indicate that the type of coherence of the cylinder shedding is important in describing the resulting unsteady upstream field. The relative phase of the cylinders dictates the effects of the constructive/destructive interference of the potential-like waves. Synchronous shedding of the cylinder results in a flow field in which the unsteady velocity slowly decays with upstream distance, but the unsteady pressure is greatly reduced. Asynchronous shedding produces the opposite effect in which the unsteady pressure decays very slowly, but the unsteady velocity drops at a rate far faster than predicted by potential flow theory, due to the constructive and destructive wave interactions from the

cylinders. (CFD results were not verified experimentally because neither synchronous nor asynchronous shedding could be produced in a freestream flow.)

7.3 Cylinders Downstream of a Cascade

As expected from the CFD results in Section 7.2 from the modified inlet conditions, an array of cylinders located downstream of a set of blades shed vortices coherently. From the CFD results for an inlet condition with a shear layer between each cylinder, the expected cylinder shedding from the experimental set-up downstream of blades was to have synchronous shedding. However, the cylinders shed in an asynchronous fashion, similar to the CFD with the effective wake spacing doubled. The shear layer produced downstream of the blades was not strong enough to support the synchronous shedding. The blade induced shear layer was strong enough to force the cylinders to behave coherently; however, the shear layer was not strong enough to overcome the stable asynchronous shedding of the cylinders.

From the results from Ohya et al. [47], asynchronous cylinder shedding is expected in a freestream when the cylinder spacing is less than 3.5 diameters center to center. (The cylinder spacing was 5.33 in the current experiment.) The shear layer produced by the wakes from the blades of the cascade reduce the effective distance between the cylinders to that required for asynchronous shedding. The experimental cylinder vortex shedding phase results from the removal of every other cylinder from the array confirmed this argument. If the wakes themselves were solely causing the coherence of the cylinders, the expected results would be that each cylinder shed synchronously. Instead, each cylinder behaves randomly, indicating that the spacing between the cylinders is too large.

The position of the cylinders in relation to the wakes had a major impact on the coherence of the cylinder shedding. Placing the cylinders in the blade wakes eliminated any coherence in the shedding. The cylinder location mid-way between the blade chordlines provided the maximum asynchronous coherence among the cylinders.

The inlet velocity, and thus velocity through the array of cylinders, played a major role on the coherence of the array of cylinders. The cylinder coherence correlated with the

tunnel velocity. Increasing the tunnel velocity reduced the standard deviation of the mean relative phase difference between cylinders. At velocities less than 85 m/s, the cylinder shedding is completely random; however, increasing the velocity to 135 m/s created a flow field in which the relative phase between the cylinders followed a Gaussian distribution. The inherent coherence intermittency caused variance in the relative phase between the cylinders. Increasing the tunnel velocity decreased the phase difference standard deviation. A reasonable interpretation is that increasing the velocity (beyond the capabilities of this tunnel) would produce even lower standard deviation between the cylinder phases.

7.4 Unsteady Velocity Along a Cascade Blade

Unsteady velocities were experimentally measured along the blade surface for the cascade with the array of cylinders located downstream. On the pressure side, the unsteady velocity amplitude was maximum at the trailing edge of the blade and decreased rapidly with upstream chord location, losing over 50% of the amplitude aft of 90% chord. On the suction side of the blade, the combination of destructive interference and flow separation caused the amplitudes of the unsteady velocity to be minimal throughout the length of the blade. The unsteady effects of downstream cylinders shedding in an asynchronous fashion primarily affects the pressure side of the blade. For the experimental set-up used for this work, the unsteady velocities on the suction side of the blade would not be expected to contribute to any high cycle fatigue failures.

The unsteady velocities were increased with increased turning angle (rotated test section) and were slightly decreased with increased downstream distance of the cylinders. As expected, the ensemble averaged unsteady velocity was greatly influenced by the cylinder height above the wakes and the freestream velocity. The cylinder height influenced the unsteady velocity amplitudes because the cylinder shedding was affected by the presence of the wakes from the blades. The increased freestream increased both the percentage of time that the cylinders were shedding coherently and the magnitude of the vortices shed. Both of these parameters greatly affected the standard deviation of the relative cylinder shedding, and thus the velocity field. As the standard deviation was reduced, the measured unsteady velocities increased.

A superposition hypothesis was verified from the experimental set-up. Unsteady results from single cylinder runs were superposed to simulate different relative cylinder shedding phases. The asynchronous case of shedding produced results that closely matched the tunnel results for the cylinder array near the trailing edge of the blade, showing that superposition did hold in regions of high velocity fluctuations for the unsteady interactions between the cylinder for asynchronous shedding. The maximum amplitude was produced when each cylinder shed a vortex prior to any cylinders closer to the blade. This occurred because the unsteady velocity wave had to travel farther, and thus took a longer period of time for the unsteady influences to occur than the closer cylinders. This situation will not be seen in an engine, therefore the maximum unsteady amplitude possible will not occur on the blades. When a synchronous cylinder shedding was simulated, the superposed velocity measurements were reduced over the asynchronous case. The synchronous results would most closely model the effects of a moving rotor downstream of stators with equal number of blades. For the configuration with the cylinders 1/3 chord downstream, the expected rotor results would produce lower unsteady velocity amplitudes than were produced by the asynchronous shedding.

VIII. Future Work

The effects of downstream forcing was examined in this work and found to create unsteady velocities along the blade surface. Future work in this field would be of great benefit in developing a better understanding of this effect.

8.1 Three-Dimensional Effects

The three-dimensional effects of cylinder shedding were not examined in this work. It is well known that a cylinder located in crossflow will produce shedding that is not uniform with span. In this work, three-dimensional effects were minimized by measuring the velocities 1/16 inch from the centerline with the cylinder pressure tap at the centerline. The span of the tunnel was two inches, so wall effects in addition to the three-dimensional cylinder shedding will influence the results.

Propagating potential-like waves in the spanwise direction may influence the flow upstream of the cylinder array. For the CFD model used in this work, the waves were assumed to be propagating with no spanwise component, allowing the use of a two-dimensional simulation. This is not the case in the true flow and may prove to help explain the discrepancies between the CFD results and the experimental values.

The development of a CFD model in three-dimensions would increase the current understanding of the flowfield. The effects of the side walls and the spanwise shedding on a cylinder should be incorporated into the simulation results.

The simulation may never completely describe the tunnel flow field because the shedding of a single cylinder is unsteady in both phase and amplitude of the vortex being shed. These two effects are not represented in CFD because no randomness is present. Both of these effects would cause lower unsteady velocities on the blade than shown in the simulation.

8.2 High Velocity

It was noted in this work that the velocity of the flow influences the coherence of cylinder shedding, and thus the unsteady velocities on the blade. Using the current set-

up in a facility with a higher maximum velocity could create a flow with lower reduced coherence intermittency.

It is expected that increasing unsteady amplitudes with velocity would only continue up to some maximum velocity. At a high velocity, compressibility will alter the propagation of the potential-like waves, and the unsteady amplitudes would decrease.

8.3 Blade Pressure Readings

With current measurement techniques, the unsteady pressures cannot be measured near the trailing edge of the blade. Such surface measurement systems as pressure sensitive paint is an order of magnitude too slow for this work.

A method for possibly allowing the pressure to be measured would be to thicken the blade used for this work. Thicker blades might allow pressure sensors to be mounted internally in the blade.

Pressure measurements along with velocity measurements at a given point would greatly increase knowledge of the flowfield. The combination of pressure and velocity measurements for the flow could possibly be used to predict the pressure field for other configurations when only the velocity is known.

8.4 Active Forcing

All of the experimental results acquired for this work were the result of asynchronous cylinder shedding. Through the use of superposition, the flow upstream of a synchronous shedding array can be inferred. The use of an active forcing mechanism, however, can produce synchronized shedding.

Active forcing could also decrease the coherence intermittency between cylinders, allowing results more representative of the true flow with coherent shedding. Currently, high coherence intermittency between cylinders produces flows resembling coherent shedding when averaged, but with lower magnitudes because the effects of intermittency are included in the average.

8.5 Coherence Length Measurement

The coherence of the cylinder shedding was measured in this work by calculating a standard deviation of the relative phase differences between cylinders taken at different instances of time for a given cylinder vortex shedding strength.

The long term coherence between the cylinders and the true coherence length of the relative cylinder shedding could be determined by capturing a long string of data rather than using a phase-lock method to acquire the voltages. Once a long string of voltages have been captured, the phase-locking and phase relationships can be determined through post processing. This process would produce an accurate estimation of the coherence length. Additionally, capturing the unsteady velocities in this manner would produce results that more closely represent the true forces acting on the blades rather than the force on the blades for a given trigger cylinder vortex strength.

Appendix A. Probe Velocity Calibration

The velocity calibration for the probe is a very critical procedure for accurate data reduction. The first step in preparing for the calibration is to determine the value of K, which is calculated as

$$k_i = \frac{E_{1i}}{E_2 i} \tag{A.1}$$

where E_1 and E_2 are the voltages from the top and bottom of the sensor, respectively. For the calculations, only a single value for k is desired for the entire calibration velocity range. Because of this, the overheat settings are iterated and a wide velocity range is examined until K is roughly constant for all velocities. Once the values of the overheat for each of the channels are determined, they are fixed for all calibration processes and data collection performed using the probe.

Since the value for k does change slightly for the different velocities, Eq. (A.1) is rewritten for data reduction purposes as

$$k = \frac{1}{N} \sum_{i=1}^{N} \frac{E_{1i}}{E_{2i}} \tag{A.2}$$

where N is the total number of points.

A.1 Velocity Calibration

Once the value of the overheats has been determined, the velocity calibration can begin. The split-film probe is placed directly over the nozzle of the calibrator system. The velocity of the calibration flow is determined by comparing the pressure results from a pressure transducer located in the settling chamber to a correlation table provided by the manufacturer. The sensor must be placed less than one nozzle diameter above the nozzle exit for the results to be accurate. A number of points, typically 20 was used for this work, are collected over the entire desired velocity range. A small velocity range corresponding to the expected tunnel conditions for a single tunnel speed setting proved to provide a more accurate curve-fit than a single calibration that includes both of the tunnel velocities used.

If it is desired to calibrate the probe at a set temperature rather than use the temperature corrections in the data reduction process, the heater must be utilized. Calibration cannot continue until the temperature in the settling chamber stabilizes, a process which takes at least 20 minutes. The setting on the heater thermostat controls the air in the heater tube, but the temperature is greatly reduced at the settling chamber. An iterative method must be used with the thermostat if a specific temperature is desired in the settling chamber.

Although the gain and offset settings of the sensor can be used to maximize the signal to noise ratio and produce more accurate results, the voltage used for the calibration must be unamplified. Once the calibration voltages have been collected, the software must solve the following equation from TSI TB 20[45]

$$\left(E_{1i}^2 + \bar{K}^2 E_{2i}^2\right) = \left[C_{vel} + D_{vel}\vec{V}^{n_{vel}}\right](\Delta T) \tag{A.3}$$

where ΔT is defined as

$$\Delta T = \frac{T_1 - T_2}{2} - T_e \tag{A.4}$$

where T_e is the recovery temperature in the calibrator and T_1 and T_2 are the sensor temperatures.

In Eq. (A.3), all of the values are known for each point except for A, B, n. A nonlinear regression routine can be used to solve for best fit values for each parameter.

After convergence has been obtained, the error of the curve fit is calculated as

$$Error = \frac{\left[\frac{\left(E_{1i}^2 + k^2 E_{2i}^2\right)}{(\Delta T)} - \left(C_{vel} + D_{vel}\vec{V}_i^{n_{vel}}\right)\right]^2}{\frac{\left(E_{1i}^2 + k^2 E_{2i}^2\right)}{(\Delta T)}} \tag{A.5}$$

Once this error has been calculated, the value is displayed on the screen.

A.2 Angle Calibration

Upon completion of the probe calibration for multiple velocities, the probe must be calibrated for the angles of incidence the probe is likely to encounter in the flow. From

the combination of the velocity and angle calibrations, the velocity over the probe can be expressed in Cartesian components.

The angular calibration is performed by physically moving the probe to provide various flow angles over the probe axes. A velocity within the valid calibration velocities is set and held constant throughout this process. After the zero angle velocity is obtained, the angle is changed and voltages are collected again. This process occurs for the entire desired angular range.

An issue with the calibration setup is that the angles can only be changed in discrete increments of 6°. Also, the probe configuration prohibits calibration at negative angles because the probe body would physically touch the calibrator. For this reason, the angles used are only positive and only five points are used corresponding to $0° \leq \alpha \leq 24°$.

From the calibration equations, the incident angle can be calculated as

$$\sin\alpha = \frac{E_1^2 - k^2 E_2^2}{C_{angle}\left(E_1^2 + k^2 E_2^2\right)^{D_{angle}}} \tag{A.6}$$

where α is the angle of incidence and k is defined from Eq. (A.2). Eq. (A.6) can be rewritten as

$$E_1^2 - k^2 E_2^2 = C_{angle}\left(E_1^2 + k^2 E_2^2\right)^{D_{angle}} \sin\alpha \tag{A.7}$$

Eq. (A.7) is the form of the equation used for the angular calibration routines. From this equation, only C_{angle} and D_{angle} are unknown and are determined using the curve-fit routines discussed in Appendix B.

Upon the convergence of C_{angle} and D_{angle}, the angular sensitivity of the probe has been calibrated and these are used in the data reduction routines along with the velocity calibration to reduce the probe voltage data taken from the tunnel.

Appendix B. Curve-fit Routines

The curve fit routines were adapted from a Nonlinear Regression routine from Chapra and Canale[55]. This Gauss-Newton based algorithm was designed to allow data points to be curve-fit based on an equation of known form but unknown constants. For this algorithm, the partial derivatives for the equations are required and a matrix is created by evaluating the various partial derivatives at each point. For example, the matrix for an equation with three parameters would be expressed as

$$[Z] = \begin{bmatrix} \frac{df_1}{da_0} & \frac{df_1}{da_1} & \frac{df_1}{da_2} \\ \frac{df_2}{da_0} & \frac{df_2}{da_1} & \frac{df_2}{da_2} \\ . & . & . \\ . & . & . \\ \frac{df_N}{da_0} & \frac{df_N}{da_1} & \frac{df_N}{da_2} \end{bmatrix} \tag{B.1}$$

where $f(x)$ is the equation used for the curve fit.

The second matrix required for the calculations is a matrix containing the difference of the data and equation $f(x)$ evaluated at each point. The generated matrix is

$$\{D\} = \begin{Bmatrix} y_1 - f(x_1) \\ y_2 - f(x_2) \\ . \\ . \\ y_N - f(x_N) \end{Bmatrix} \tag{B.2}$$

Through the use of these equations the vector containing the changes in parameter values $\{\Delta A\}$ can be calculated using the following equation.

$$\left[[Z]^T [Z]\right] \{\Delta A\} = [Z]^T \{D\} \tag{B.3}$$

Solving Eq. (B.3) for $\{\Delta A\}$ gives

$$\{\Delta A\} = \left[[Z]^T [Z]\right]^{-1} [Z]^T \{D\} \tag{B.4}$$

The new values for each of the parameters of the equation $f(x)$ can be calculated from the value for $\{\Delta A\}$ calculated in Eq. (B.4). The new value of each parameter is calculated as

$$a_{i,j+1} = a_{i,j} + \Delta a_i \tag{B.5}$$

where i is the parameter number and j is the iteration.

This routine is repeated until the error defined as

$$|\epsilon_a|_i = \left| \frac{a_{i,j+1} - a_{i,j}}{a_{i,j+1}} \right| \tag{B.6}$$

is less than a user defined criteria. Once this occurs, the values for each of the parameters are output from the routine.

Appendix C. Data Reduction Software

C.1 Introduction

In an effort to streamline the data reduction process and to improve on data reduction times, a computer code was written in Microsoft® Visual Basic® 6.0 to allow for batch processing of files collected from the tunnel. The code was streamlined using a modular design process to improve performance and organization. Currently, this software is written only for split-film sensors and will not allow the use of x-wire sensors.

C.2 Software Organization

When the software is originally executed, a screen appears with four different options. The first option is to set-up the calibration of a probe, two of the options analyze files obtained from the experiments, and the final option is to exit the software.

Probe calibration screen. When the **Calibrate Velocity** button is selected from the overview screen, the probe calibration screen appears. As seen in Fig. C.1, the calibration screen is divided into three main parts. The first part contains the information regarding the calibration temperature and the probe temperatures.

The other two parts of the screen contain the information regarding the velocity and angular calibrations. After solving for the calibration constants in the probe calibration equations, the values for each of the parameters are displayed on this form for use with data reduction calculations.

Reduce data screen. When the **Reduce the Data** button is pressed from the Overview screen, the Reduce Data Screen is activated. From this screen, shown in Fig. C.2, the data collected can be reduced and an output file generated. It is important to note here that the calibration constants must be set on the Probe Calibration Screen *prior* to reducing the data. The reduce data screen is divided into three main sections. These sections are the file section, split film settings section, and the options section.

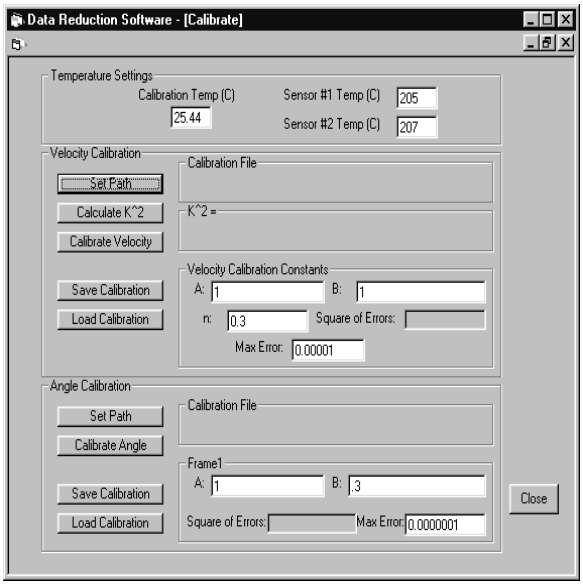

Figure C.1 Calibrate velocity screen

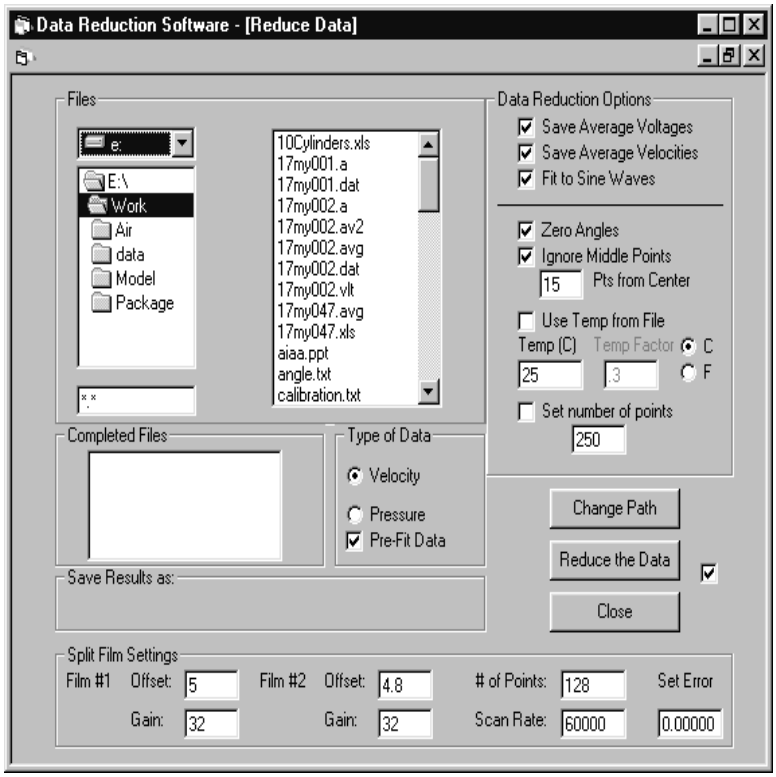

Figure C.2 Reduce data screen

File section. The first section is the file section of the screen. As seen in Fig. C.2, this section provides for a listing of the input files, the output file, and the current file status.

The input files are selected from the upper left side of the screen. Once the correct disk drive and directory are selected, individual files can be selected. Multiple files can be selected through the use of the *Shift* or *Control* keys as used in most applications. A filter is provided to aid in the selection of input files by allowing only files matching a certain criteria to be displayed.

The output file name is selected through the use of the **Change Path** button on the right side of the form. This file will contain all output of the curve-fit data created during the data reduction execution. If the file already exists, the old file is erased and the new results are written. The output file is not necessary if the data is not being curve fit.

The current file status provides a list of each of the files that have been reduced in this run. This function is very helpful for monitoring the progress of the data reduction. This box only provides the names of the previous six completed files.

Split-film settings section. The bottom of the Reduce Data screen contains the split film settings section. This section provides most of the necessary settings required to provide for an accurate data reduction. The first portion of this section provides information regarding the signal conditioning of the split film sensor. In an effort to obtain the best resolution possible, the voltage signal from the sensor is passed through a signal conditioner which provides both an offset and a gain. From this, much of the range of the voltage output can be used and a better resolution of the signal is achieved. Inputting this information is very important because the voltages read must be converted back into unamplified voltages prior to using the calibration.

The next part of the split film settings provides information regarding the data file and the data collection. The data collection frequency is important for generating a time step for each point in the ensemble averaged file. The other entry in this section is the number of points per sample. This is critical for use in generating the ensemble averaged file because there is no mark in the file between each sample. If it is not properly entered,

the points used for each time step in the ensemble averaging process will not correspond to same phase of the cylinder shedding.

The final entry in this portion of the form is the maximum error allowed for the velocity curve-fits. A value is only required in this section if a curve-fit of the data is being performed.

Options section. The options section of the form can be divided into three parts. The first part of this section is located under the file selection area. From this section, the type of data being reduced is set. This is required is because the frequency for the velocity curve-fits is assumed to be at the same frequency as the cylinder shedding; however if the file contains the pressure data from three cylinders, the frequency of each cylinder is calculated. The option to prefit the data provides for a more accurate and faster convergence of the curve-fit by using a simple routine to calculate an initial guess for the frequency that will be used in the curve-fit routines.

The next portion of the options section sets the various output files for the data reduction. The first option is to *Save Average Voltages*. If this option is selected, the values for the ensemble averaged voltages will be saved with a filename in the form *filename.*vlt.

The second option available, selected by choosing *Save Average Velocities*, provides an output file for each input file with Cartesian velocity information in tunnel coordinates. This file includes the time and cylinder voltage along with the velocities. The naming convention for this file is *filename.*avg. The average velocity file provides the ensemble averaged time history of velocity over a period of shedding oscillations.

The final output option is *Fit to Sine Waves*. This option, if selected, produces an output file that contains the curve-fit information for each of the selected files. The filename used for the curve-fit data is set in the filename section of the screen. If this is selected and a valid filename has not been entered, the software will not reduce the data. Each file selected to be reduced is a single entry in the output file consisting of the curve-fit information for the trigger cylinder and either the two velocities or two additional cylinders.

The remaining portions of the options section provide some settings used in the data reduction calculations. *Zero Angles* is used if the orientation of the probe is not known to be exactly along the flow. If this option is selected, the mean flow is assumed to be only in the x-velocity and thus is only valid for points far upstream of the cylinder.

The second option is *Ignore Middle Points*. If selected, this option does not use the points near the trigger for the curve-fit. It was decided after analyzing the results generated in previous work by Hopper[28] that the readings around the trigger point, located in the middle of the file, were being influenced by the trigger. This produced a voltage spike in both velocity channels. In an effort to prevent the effects of this artificial phenomenon from influencing the curve-fit, the middle number of points selected by the user are not used for the curve-fit.

The use of tunnel temperature is essential in calculating the velocities of the flow using the split-film sensors. In an effort to increase the flexibility of the system, the temperature can either be entered on the screen, or if the *Use Temp from File* option is selected, read from the file. If the file is used for the temperature, a conversion factor is entered to allow the software to convert from voltage to degrees. The temperature can be entered in either Fahrenheit or Celsius.

The final choice in the options section of the screen allows for some flexibility in the data reduction. If *Set Number of Points* is selected, only the first number of samples equal to the number entered will be used for the data reduction. This selection is useful primarily to determine to effects of adding additional samples to the ensemble averaging to determine the effects on the output values.

Reduce data execution. Upon selection of the **Reduce the Data** button on the screen, the software begins to perform the required calculations. The first step for the reduction routine is to determine the first file to be used. This is executed by stepping from the top of the file listbox. If the first file is not highlighted, then the code steps to the filename below it. This continues until the code finds a selected file or reaches the end of the filenames.

Once the file has been selected, it is opened and the voltages are read and ensemble averaged. During the process of ensemble averaging each point, an RMS error is calculated to determine the variability in the data. The equation used was

$$Avg_{RMS} = \frac{\sqrt{\sum_{j=1}^{M} \sum_{i=1}^{N} \frac{\left(E_{j,i} - \bar{E}_j\right)^2}{|\bar{E}_j|}}}{M} \tag{C.1}$$

where v is the voltage, N is the number of samples in the file, and M is the number of points per sample. From this equation, a number is generated which describes the repeatability of the voltages. A larger value for Avg_{RMS} indicates a chaotic velocity flowfield that is not well synchronized with the shedding.

Once the average voltages have been determined, then the effects of the signal conditioner must be removed prior to any data reduction. This influence only impacts the velocity readings, so this process is not necessary for an all pressure file. The true voltage is calculated by

$$E_{true} = \frac{E_{reading}}{G} - E_{offset} \tag{C.2}$$

where $V_{reading}$ is the voltage from the ensemble averaging, G is the selected gain, and V_{offset} is the offset chosen. The true voltage, V_{true} from Eq. C.2 can then be used to determine the velocity of the flow. Eq. (C.2) is used for both channels of split-film voltage data.

The next step in the process is to determine a value for the temperature of the tunnel. Because the temperature of the flow in the tunnel reaches a steady-state value, only a single temperature is used in the calculations. If the tunnel temperature used is being taken from the file, the temperature is calculated by taking an average of all of the temperature readings made during the run. For the low speed tunnel runs, the temperature reaches a steady-state rather quickly. However, for the high speed runs, the tunnel heats up greatly, so data cannot be taken until the tunnel reaches thermal steady-state. If the temperature is directly entered on the form, this process is not necessary and the entered value is used. The temperature finally used for the calculations is converted into Celsius.

The actual data reduction is now performed by the software. Initially, the difference in temperatures is calculated as

$$\Delta T = \frac{T_{s1} + T_{s2}}{2} - T_e \tag{C.3}$$

where T_{s1} and T_{s2} are the top and bottom sensor temperatures, respectively. T_e is the average temperature from the flow. Along with ΔT, the sum and difference of voltage must be calculated as

$$Sum = E_1^2 + k^2 E_2^2 \tag{C.4}$$

$$Diff = E_1^2 - k^2 E_2^2 \tag{C.5}$$

where E_1 and E_2 are the true voltages from Eq. (C.2). The value for k is calculated in the calibration of the sensor. The magnitude of the velocity is then calculated from Fisk[44] as

$$\vec{V} = \left(\frac{\frac{Sum}{\Delta T} - C_{vel}}{D_{vel}} \right)^{\frac{1}{n_{vel}}} \tag{C.6}$$

where C_{vel}, D_{vel}, and n_{vel} are calculated from the calibration process. The angle of incidence of the flow is calculated from Fisk[44] as

$$\alpha = \sin^{-1} \left[\frac{Diff \cdot Sum^{-D_{angle}}}{c_{angle}} \right] \tag{C.7}$$

where c_{angle} and D_{angle} are calculated from the angular calibration process.

Once the magnitude of the velocity and the flow angle are known, the flow can be converted the Cartesian components as

$$u = \vec{V} \cos \alpha \tag{C.8}$$

$$v = \vec{V} \sin \alpha \tag{C.9}$$

The final portion of the data reduction portion of the code is to curve fit the data to a Sine wave. Initially, the pressure signal, in voltages, is fit using

$$P = \bar{P} + A_{Pp} \sin\left(\omega t + \phi_{Pp}\right) \tag{C.10}$$

where A_{pP}, ω, and ϕ_{pP} are calculated using a curve fit. If the file is an all pressure file, Eq. (C.10) is used twice more for the other pressure channels. Otherwise, only the frequency, ω, is used from Eq. (C.10). If desired, prior to curve fitting the pressure data, a prefit is used. For this prefit, the code searches for one voltage peak to the left of the trigger point and one voltage peak to the right. Since the trigger occurs at a peak, the number of points between the left and right point define two periods of the frequency and a frequency can be initially guessed.

The velocity is then fit using both the primary frequency, and the harmonic, defined as 2ω. The equation then becomes

$$u = \bar{u} + A_{up} \sin\left(\omega t + \phi_{up}\right) + A_{uh} \sin\left(2\omega t + \phi_{uh}\right) \tag{C.11}$$

where A_{up} and ϕ_{up} are calculated for the primary frequency. A_{uh} and ϕ_{uh} are calculated for the first harmonic frequency. Eq. (C.10) is used to calculate the y-component of the velocity by replacing the u with v.

After the curve fit has been generated, the software performs a check on how well the data fits the curve. An RMS error similar to the one calculated in Eq. (C.1) is used. This provides a general idea on how the curve fit performed and how clean the data is.

The output file contains the filename, the shedding frequency, the amplitude and phase shift for the pressure signal, the mean of both velocity components, and the amplitude and phase shift for both the primary and harmonic fits for the velocities. Additionally, the output file contains the RMS error values for both the ensemble averaged voltages and for the curve fit for each component.

Fit data screen. The Fit Data screen is designed to allow for a quick analysis of data that has already been either ensemble averaged or saved in the Cartesian velocity

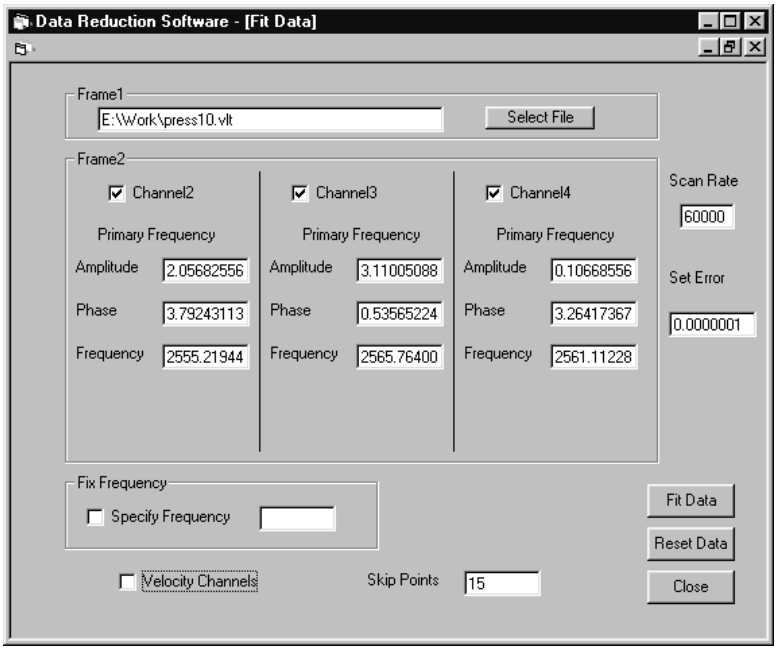

Figure C.3 Fit data pressure screen

components. This screen provides the results of the curve fit on-screen. The flexibility of this form allows for only the desired channel to be reduced, reducing the time required for the data reduction. The two types of data that can be reduced by this form are the all three channel pressure voltages and the velocity.

Pressure data. This form provides quick insight into the three channel pressure file. The files generally used for this purpose have been saved as *filename.vlt*. Once the filename has been selected, the data can then be quickly reduced. As seen in Fig. C.3, the form outputs to the screen the amplitude, phase shift, and frequency for each channel. Because each of the channels is a pressure signal, the unique frequency for each is desired; however, all of the frequency readings should be approximately identical.

The bottom of the screen allows the frequency to be specified. Using this option forces all three curve fits to be executed for that exact frequency. This method allows for an identical shedding frequency to be specified for all three channels.

Velocity data. Through the use of this function, selected by choosing the velocity checkbox, the velocity signals are reduced to the curve-fit parameters and displayed

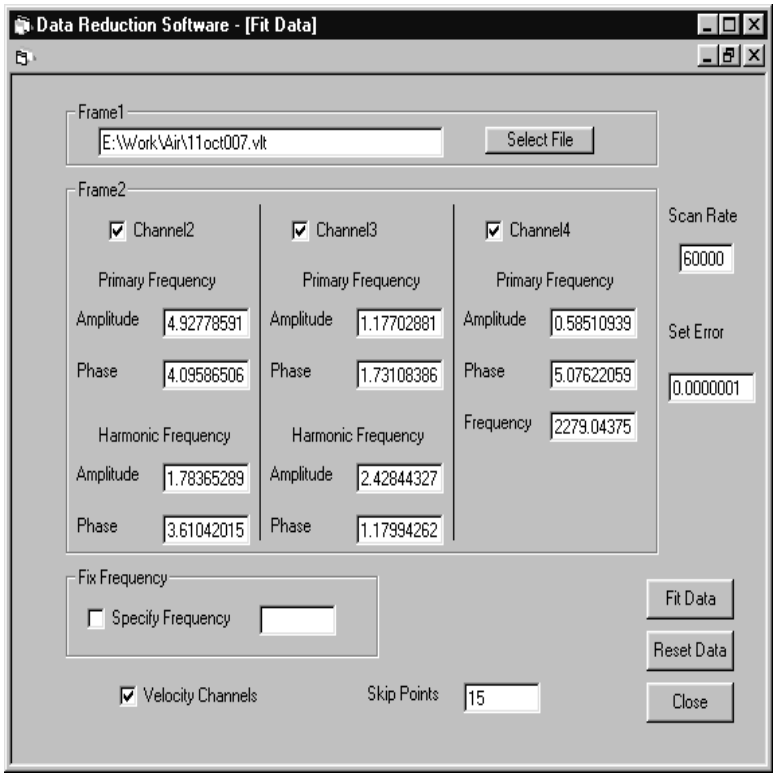

Figure C.4 Fit velocity data

on-screen. As seen in Fig. C.4, the displayed parameters are changed from those shown in Fig. C.3.

For the second and third channels, the frequency field has been changed from frequency to the harmonic amplitude and phase curve-fit values. The frequency is removed because the frequency for the velocity channels is forced to be the same frequency as the pressure signal.

Appendix D. Single Cylinder CFD Results

The computer simulations were performed with Fluent, Version 6.0[49] on a Beowulf cluster located at the Air Force Institute of Technology. Fluent was designed to model fluid flow and heat transfer in complex geometries using structured or unstructured grids.

The solutions generated were 2-D in keeping with the experimental assumptions made. The laminar solver was used, given the Reynolds number in the experiment, and provided an excellent resolution of the vortex shedding from the cylinder. The segregated solver, which solves the continuity and momentum equations sequentially, was used since this solver has traditionally been used for mildly compressible or incompressible flows. The flow field was assumed to be incompressible for these results due to the Mach number of the flow field being approximately 0.3 and because the desired oscillations are believed to be caused by the oscillating incompressible potential waves propagating from the cylinders.

D.1 Single Cylinder Grid

The grid shown in Fig. D.1 was produced using the Elliptic-Laplace structured mesh option[50] in the mesh generator add-on for TecPlot. The grid consists of approximately 36,000 nodes. The field was divided into two sections by a horizontal line passing through the center of the cylinder. Grid spacing for each section was established with 2-sided exponential spacing, allowing the points to be clustered along the cylinder surface as well as the top and bottom walls in order to capture viscous effects. An unfortunate side effect of partitioning the flow field in this manner is the high concentration of grid points along the inlet and outlet of the test section, a region where lower grid density is desired, increasing the time required to generate a solution.

The dimensions for the grid (shown in inches) were taken from the experimental set-up. Both the height and the width of the test section were 8 inches, with the cylinder located in the center. The cylinder diameter was 3/16 in diameter.

The boundary conditions for the top and bottom walls were set as a wall boundary with zero normal velocity and no-slip conditions. The outlet was set to the outflow bound-

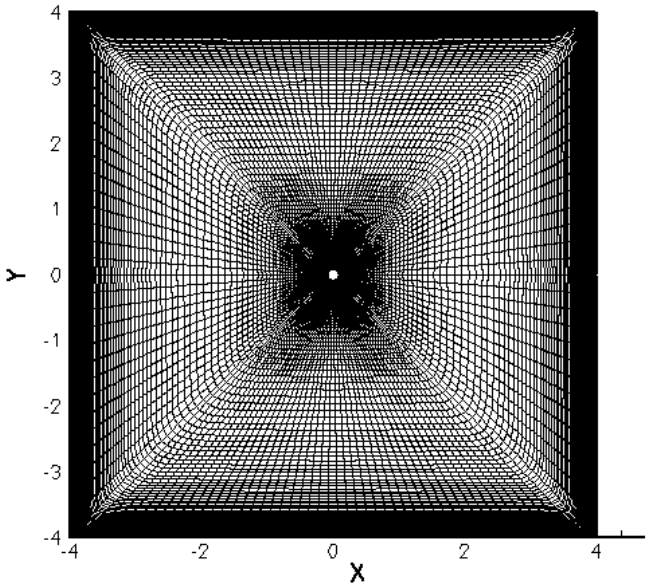

Figure D.1 Single Cylinder Grid

ary condition available for incompressible runs in Fluent. The inlet velocity was set to a constant velocity of 125 m/s.

D.2 Data Reduction

The CFD results were generated using a time incremented unsteady solution of the flow field. The time step was chosen so that 512 sequential time files would capture more than five periods of shedding (based on 5.25 kHz at 125m/s). This time step was one fourth the time step used in the experimental data collection. That is, for the free stream flows of 125 m/s at a data collection rate of 120kHz, a quadrupling of this rate led to a time step of $2.0833 \text{x} 10^{-6}$ seconds. 128 output files were saved at every fourth time step, thus generating the time spacing equivalent to the experimental data collection.

For the collection of 128 data files representing field data at every other time step, a routine was written to extract field location, u- and v-velocity, and pressure at locations in the flow field corresponding to experimental work. Data was also collected from a location just above each cylinder surface, corresponding to the pressure tap located at the ninety-degree point on the experimental cylinders. The unsteady flow properties for each location

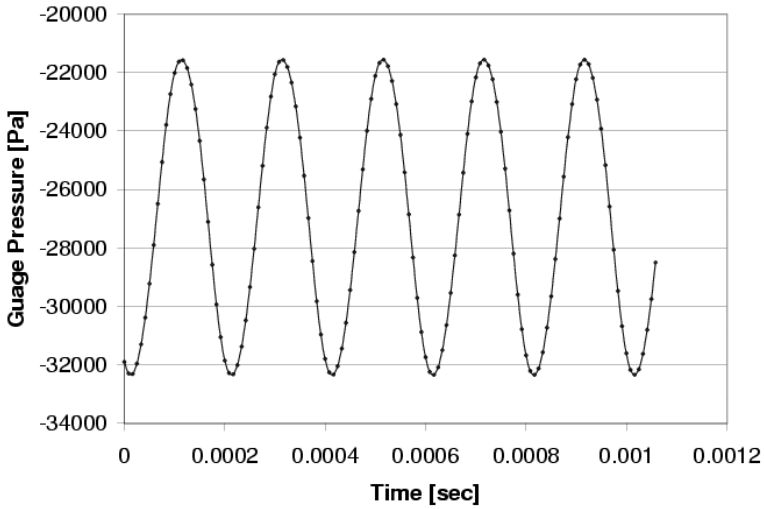

Figure D.2 CFD Pressure Along Top of Cylinder

were placed in a time resolved file for each field location, allowing the data to be time and frequency analyzed.

At each desired point, the pressures and velocity components were curve fit to a version of the sinusoidal equation used for the experimental data. The CFD results were reduced using Eqs (2.8) and a form of Eq. (2.7) modified by adding a harmonic term as

$$P = \bar{P} + A_{pp} \sin\left(\omega t + \phi_{pp}\right) + A_{ph} \sin\left(2\omega t + \phi_{ph}\right) \tag{D.1}$$

where A_{ph} and ϕ_{ph} are the first harmonic amplitudes and frequency.

D.3 Results

Time results at cylinder surface. The reference point for the time analysis of each simulation run is the point corresponding to the top of the cylinder - the trigger point for data collection in the experimental results. The pressure signal for the point located at the cylinder surface with 125 m/s inlet velocity, shown in Fig. D.2, is sinusoidal and the calculated two-frequency sine fit follows the signal almost exactly. From the curve fit, a harmonic is present with an amplitude approximately 4% of the primary frequency.

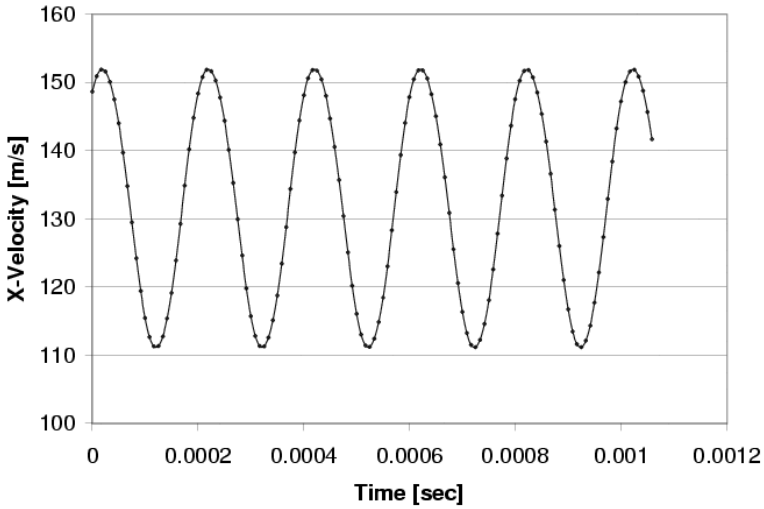

Figure D.3 CFD X-Velocity Along Top of Cylinder

The velocity components of the flow at the same location are shown in Figs. D.3 and D.4. Both of the velocities exhibit sinusoidal behavior, with a harmonic component amplitude less than 2.5% of the primary frequency amplitude for both of the velocity signals.

Time results in flow field. The results at a location one inch upstream of the cylinder and 0.125 inches above the centerline were chosen because the data provided the worst-case curve fit of all the points examined. As seen in Figs. D.5 and D.6, the velocity components have a sinusoidal character. For the x-velocity component, Fig. D.5, the amplitude of the harmonic increased to 10% of the fundamental amplitude. The y-velocity exhibited the fundamental frequency with a harmonic amplitude less than 1% of the fundamental frequency.

Some interesting results are seen from the pressure trace at the same location shown in Fig. D.7. The pressure fluctuation at this point in the flow field now has a harmonic component greater than 50% of the fundamental amplitude.

The pressure result agrees closely with Fabian[13] who showed the importance of the harmonic frequency on the pressure signal propagating upstream in the cascade. It is

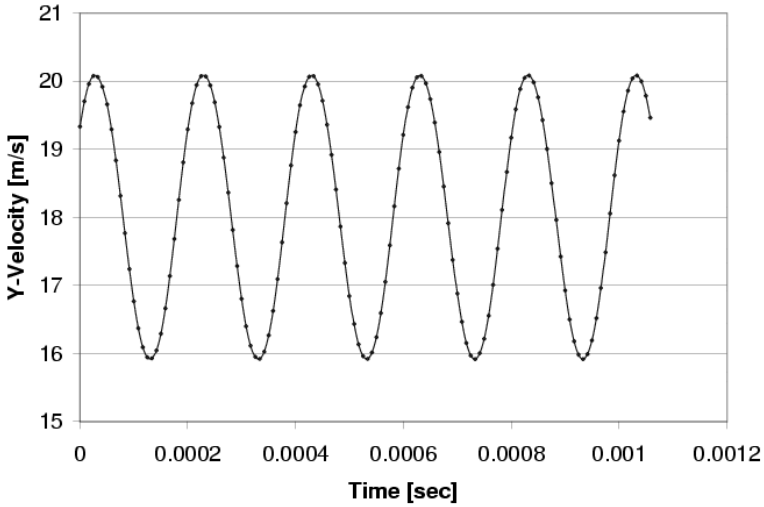

Figure D.4 CFD Y-Velocity Along Top of Cylinder

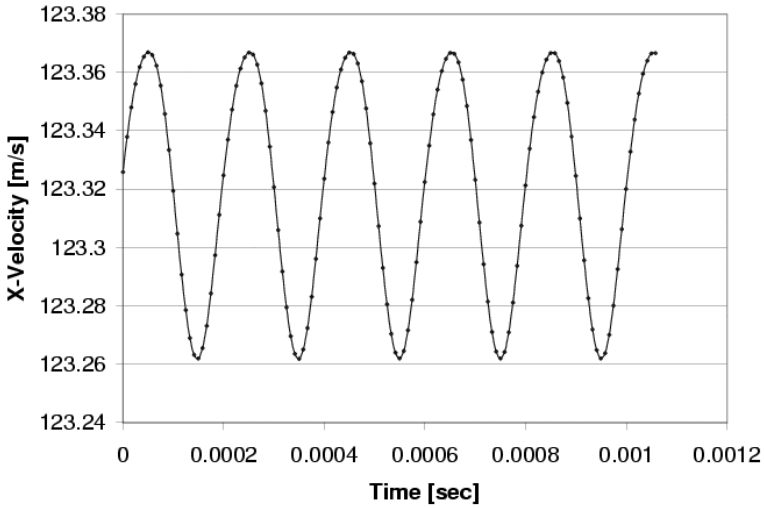

Figure D.5 CFD X-Velocity at 1 Inch Upstream and 1/4 Inch Above Cylinder

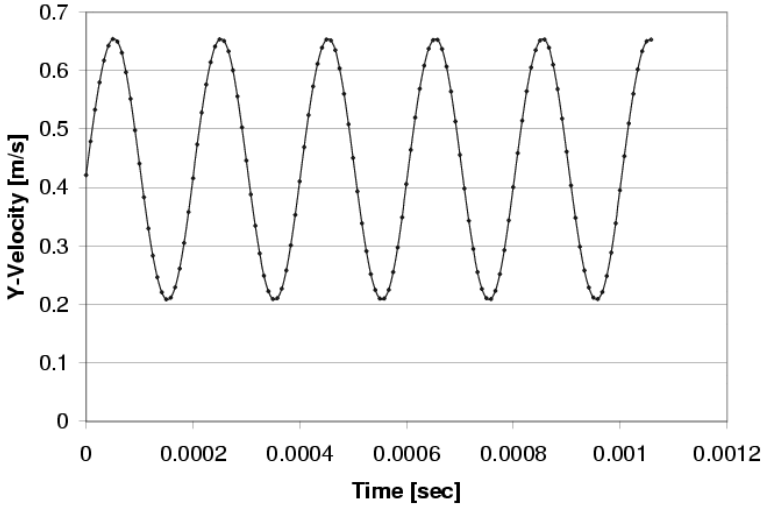

Figure D.6 CFD Y-Velocity at 1 Inch Upstream and 1/4 Inch Above Cylinder

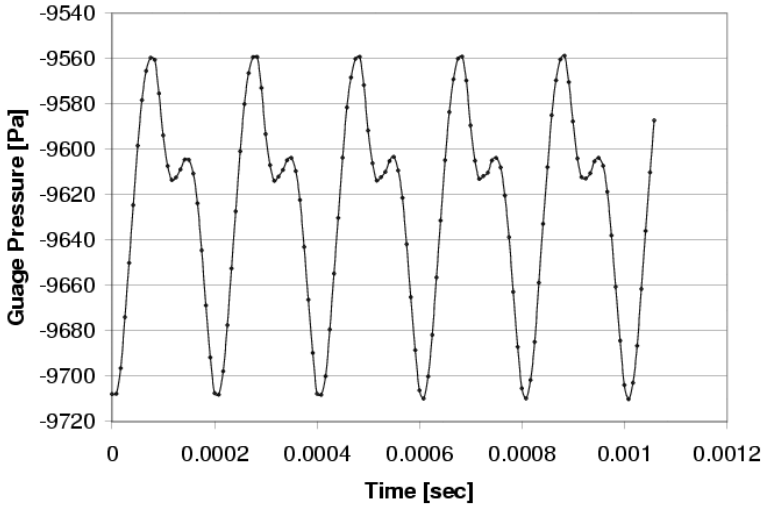

Figure D.7 CFD Pressure at 1 Inch Upstream and 1/4 Inch Above Cylinder

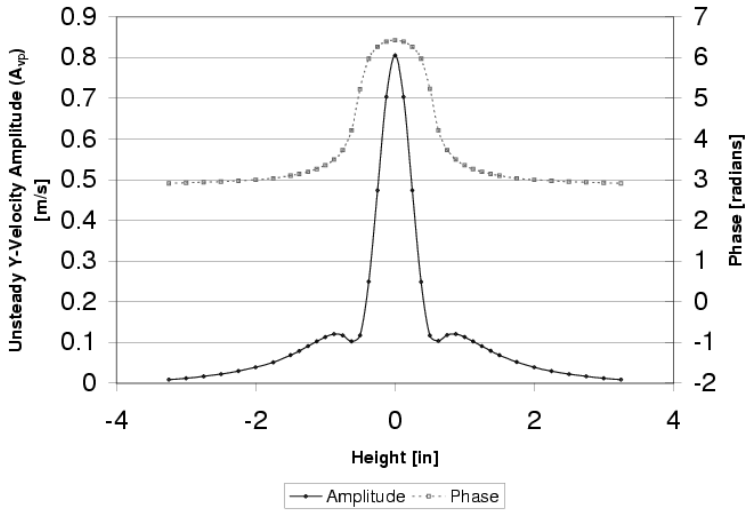

Figure D.8 Singe Cylinder CFD Y-Velocity Amplitude at 1/2 Inch Upstream of Cylinder

interesting to note that, even though the harmonic in the pressure signal is large, only a small harmonic is seen in the velocity components.

Amplitude/phase comparisons. As shown in the previous figures, the curve fits accurately describe the time-resolved results. Thus, it is expedient merely to compare unsteady amplitudes and phase shifts, rather than examining the actual time data.

An example of the results of the amplitude of the y-velocity fluctuations is shown in Fig. D.8 for a location $\frac{1}{2}$inch upstream of a cylinder. A peak in the y-velocity fluctuation is directly upstream of the cylinder, but the amplitude diminishes with y-distance up to about $\frac{1}{2}$inch. At this point, the amplitude increases for a small distance and then declines with distance. The phase shift of the sinusoidal fluctuations falls off by about π radians at $\pm\frac{1}{2}$inch. This may be a wall effect since potential flow theory absent wall images would not predict the phase shift.

At distances upstream of the cylinder, the amplitude decline is spread out, as can be seen in Fig. D.9, and the sudden phase shift has disappeared. In addition, the amplitude fall off does not follow a 1/r law (where r is the radial distance upstream of the cylinder) as might be expected in potential flow.

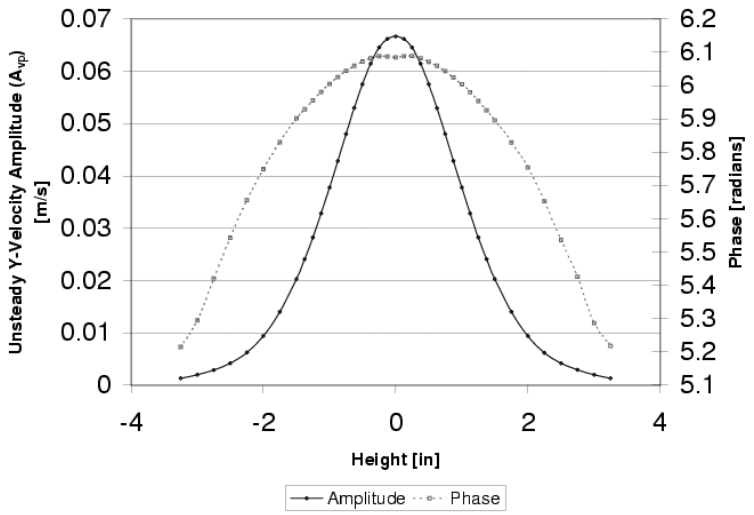

Figure D.9 Single Cylinder CFD Y-Velocity Amplitude at 2 Inches Upstream of Cylinder

The decrease of the y-velocity fluctuations at the tunnel centerline is shown in Fig. D.10. The fall off has the form of approximately $1/r^2$. The phase also generally drops with distance.

All CFD results presented thus far have been for the y-velocity at the fundamental frequency. Results were also obtained for the harmonic frequency and the x-velocity fits. A representative sample of the x-velocity component is shown in Fig. D.11. (The peak of the x-amplitudes is approximately 1.5 inches upstream of the cylinder center.) The amplitudes of the x-velocity results are symmetric about the centerline of the cylinder; however the phase changes by π radians due to fluctuations in the circulation around the cylinder that result in a positive x-velocity fluctuation on one side of the cylinder and a negative fluctuation on the other side. It can also be seen that the maximum of the x-amplitude shown in Fig. D.11 is approximately half the maximum of the y-amplitude shown in Fig. D.9.

At the location closest to the cylinder in Figs. D.9 and D.11, the x-velocity is influenced by the stagnation line of the cylinder, causing the x-velocity fluctuations to be eliminated. The y-velocity amplitudes are maximum at the point because the circulation propagating from the cylinder is entirely in the y-direction along the centerline. At a point one inch above the centerline, the unsteady velocities are approximately the same for both

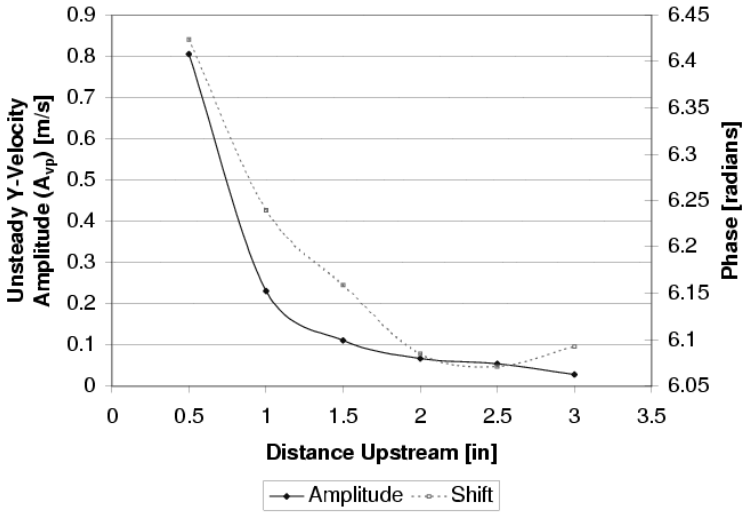

Figure D.10 Single cylinder CFD Y-Velocity Amplitudes Along Test Section Centerline Upstream of Cylinder

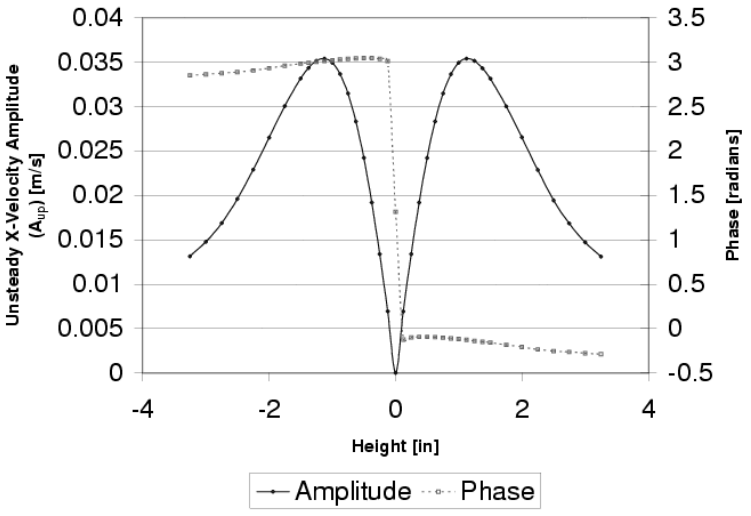

Figure D.11 Single Cylinder CFD X-Velocity Amplitude at 2 Inches Upstream of Cylinder

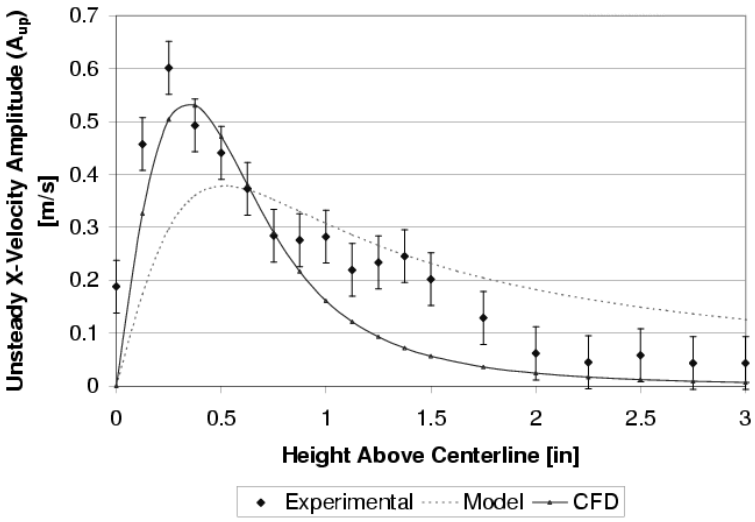

Figure D.12 Comparison of Unsteady X-Velocity Amplitude 1/2 Inch Upstream of a Cylinder

the x- and y-velocities. The lower maximum x-velocity amplitude is caused by the radial distance at the location of maximum x-velocity fluctuations being greater than the radial distance to the y-velocity maximum fluctuations..

When the free stream velocity was decreased from 125m/s to 60m/s, the shedding frequency of the cylinder was more than halved (not shown). The amplitudes were also decreased, but the general shapes of the amplitudes were identical for the two speeds. (That is, if the magnitudes for the two speeds are normalized by the maximum magnitude at the upstream location, the curves are identical.)

D.4 Comparison of Experimental and CFD Results

The accuracy of the CFD model can be determined by plotting the CFD calculated unsteady amplitudes along with the experimental and modelled results, as seen in Fig. D.12. Both the CFD and the model poorly predict both the actual unsteady amplitude values and the trends present in the data. Like the model, the CFD results predict that the x-velocity unsteady amplitude will be eliminated along the centerline although the experimental data does not show this trend.

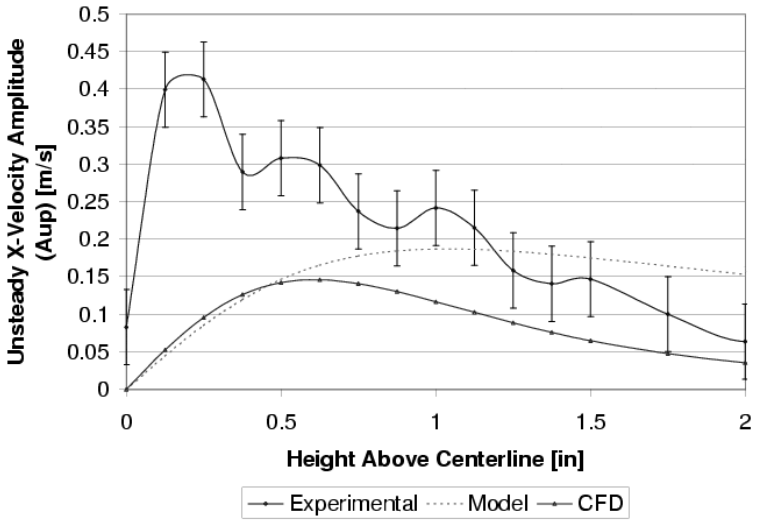

Figure D.13 Comparison of Unsteady X-Velocity Amplitude 1 Inch Upstream of a Cylinder

Each of the three solutions predict a different rate of decline of the amplitude with height. The amplitudes predicted by the model have the smallest decline with height and the CFD predicts the largest decline in amplitude. The experimental results indicate that the decline is greater than the 1/r predicted by the model, but less than the CFD results.

The effect of upstream propagation of the potential wave can be seen in the results for the unsteady x-velocity amplitudes at one inch upstream, seen in Fig. D.13. Like the results shown in Fig. D.12, both of the simulations fail to describe the true flow field accurately. The x-velocity amplitude is over twice the predicted results for heights less than 1/2 inch.

The experimental x-velocity amplitudes are influenced more by the height in the tunnel than by the upstream location. Both the model and the CFD predict a larger influence of the upstream distance than is seen by the experimental data.

One of the largest influences contributing to the poor agreement between the experimental results and the simulations is the three-dimensionality of the true flow field. Both the model and the CFD assume that the flow is fully two-dimensional. The three-dimensional effects missing from the simulations include the sidewalls which introduce boundary layers and cause reflections of the unsteady potential wave being examined.

A major three-dimensional effect on the flow field is present on the cylinder which sheds in a three-dimensional fashion. The shedding phase at one spanwise location along the cylinder is not necessarily the phase at a different spanwise location. The closer the two points are, the more likely that they are in phase. Three-dimensional shedding from the cylinder causes constructive and destructive interference between the potential waves emanating from various spanwise locations.

The randomness of the three-dimensional cylinder shedding cannot be duplicated using CFD. Extending the domain of the flow to include any spanwise effects would produce a cylinder that contains three-dimensional shedding. However, the simulation would be deterministic in that the results would be identical each time the simulation is run, which is not the case in the experimental results.

Any compressibility effects present in the flow are not present in the CFD model. For the CFD, the flow was assumed to be incompressible, a fairly good assumption throughout most of the flow field. However, near the cylinder surface, the flow is accelerated around the cylinder, causing the flow to be at a higher Mach number where compressibility may be an issue.

Appendix E. Computational Cascade Results

Fluent 6.0 was used to simulate the flow over a two dimensional cascade. Like the calculations performed for the freestream results, seen in Section 3.5, a time accurate solution was calculated. CFD data files for 128 time steps were used to perform a curve fit for the pressure and velocities at certain desired points.

E.1 Set-up

A computational model was developed to model the experimental set-up used in this work. The blade used was a cross section of the F109 compressor blade with a chord length of 1.5 inches. The spacing between blades was 1 inch and the solidity was 1.5. The blade was placed such that there was no stagger of the blade; thus the chord line was perpendicular to the line between the leading edges. A total of 8 blades were located within the flow field, with a blade profile used on the top and bottom walls. The exit angle of the tail boards was set to 9 degrees, a value obtained from the experimental results. The inlet angle was set to 19 degrees and the inlet plane was adjusted to provide velocity normal to that plane at 19 degrees to the cascade blades.

The grid, shown in Fig. E.1, was generated using Gridgen. A mixed grid, consisting of structured and unstructured cells, was used to grid the flow.

A structured grid was used around each of the blades and cylinders. Around each object, a structured grid of 200 points along the surface and 41 points in height was used. The initial spacing was set to 1×10^{-5} inches to ensure that the boundary layer could be clearly resolved. A geometric growth of 1.225 was used for the 40 rows off the surface.

The remainder of the test section was created using an unstructured grid. In order to capture the cylinder wakes, points were clustered behind each of the cylinders for a distance of 2 inches downstream. The decay selected for the unstructured grid was 0.9, which greatly reduced the increase in the size of the cells in most of the flow.

The simulation was executed for three different velocities: 150 m/s, 125 m/s, and 100 m/s. From these results, the effects of Reynolds number on the flow field can be examined.

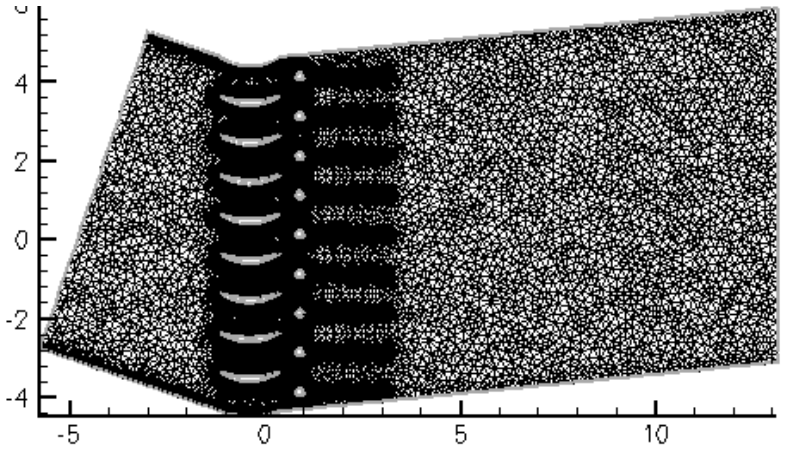

Figure E.1 Cascade grid

Three different downstream cylinder locations were also used, with distances of 1/3 chord, 2/3 chord, and 1 chord downstream.

The boundary conditions were very similar to those used for the freestream case. The blades, cylinders, and top and bottom surfaces were created as walls. A viscous structured mesh was used around the blades and the cylinders in an attempt to capture the boundary layer in these regions. A constant velocity inlet was used and the outlet was set to outflow. The flow field was initialized to have no velocity, and the inlet velocity provided the forcing required to create the flow field.

The convergence of the solution depended strongly on the time step chosen. The desired flow variations occurred up to a frequency of approximately 10 kHz. The experimental data was obtained at a rate of 120 kHz. Initially, a time step of $4.167 \text{x} 10^{-6}$ seconds, corresponding to twice the experimental collection rates, was used. The pressure and velocity fluctuations failed to converge. Using a time step of $2.033 \text{x} 10^{-6}$ seconds created a flow field that quickly converged to the desired fluctuations. For the data presented, the results are generated after an initial converging of 25,000 time steps.

Each of the CFD cascade models used laminar incompressible equations. Laminar flow was used because none of the turbulent flow models produced time accurate cylinder shedding. Each of the turbulent models created wakes behind the cylinders, but no sinu-

soidal shedding was present. The flow over the cylinders and along the blades was laminar for these velocities.

Flow simulations were attempted using compressible results, but the amplitude of the velocity and pressure fluctuations never converged. A low frequency beating caused the amplitudes and the means of the values to oscillate over time. The incompressible results produced an easily interpreted flow field because the amplitudes and means of the oscillations were constant once the flow field converged.

E.2 Baseline Results

The baseline set-up was established with an inlet velocity of 125 m/s and downstream cylinder location of 1/3 chord. Once the results created by this experimental set-up are determined, the influences of velocity and downstream cylinder location can be seen.

Cylinder shedding. The relative cylinder shedding phases are critical to the developed upstream flow field, as seen in Section 3.5. If the cylinders are shedding in a synchronous manner, the expected velocity amplitudes are relatively large, but the pressures are small. Asynchronous shedding produces very small velocity amplitudes, but high pressure oscillations upstream of the cylinder array.

As can be seen from Fig. E.2, the cylinder shedding for the baseline cascade fails to follow synchronous or asynchronous shedding for the entire cylinder array. Close to the centerline of the tunnel (cylinders 4-6), the shedding is approximately asynchronous. The relationship of the shedding between the remaining cylinders is random.

Because the data is taken from the 5th blade, the closest cylinders are numbers 5 and 6. The expected forced amplitudes are expected to be between the asynchronous and random shedding results.

Steady state velocity. Before an accurate interpretation of the unsteady results can be made, the steady state velocity along the blade must to be examined. The velocity magnitudes for both sides of the blade are shown in Fig. E.3. The magnitude of the results indicates that the location of the velocity measurements were taken outside of the

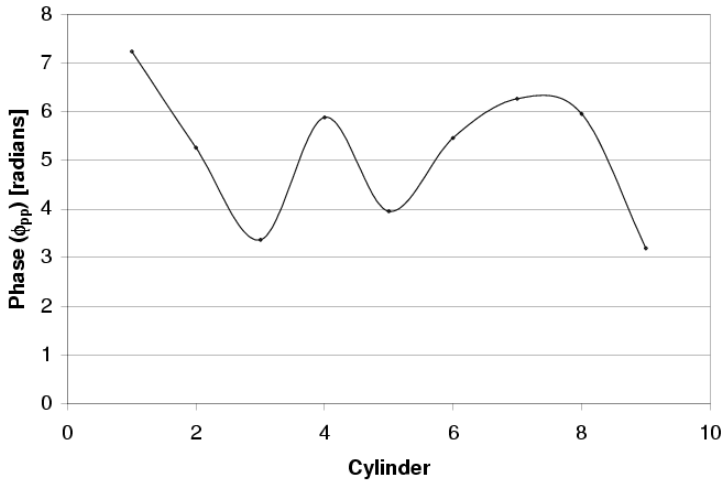

Figure E.2 CFD Pressure Phase of Each Cylinder Downstream of Cascade

boundary layer of the blade. The pressure side velocities show little dependence on the chordwise location. The velocity is approximately constant at a value lower than the inlet velocity, as expected. A slight increase in the velocity is present at 98% chord, but then is reduced at the trailing edge.

The velocity on the suction side of the blade indicates that separation occurs along the blade between 60-75% chord. At 60% chord, the velocity begins to be reduced with chord distance until a minimum is reached at 75% chord. Experimental flow visualization using oil flow shows that the blade does separate at 75% chord for this case.

Velocity fluctuation results. Amplitudes of the fluctuations were calculated for both components of the velocity. The results of the x-velocity amplitudes are shown in Fig. E.4 for both the pressure and suction side of the blade.

The pressure side of the blade produces very smooth results. For most of the chordlength, up to about 75% chord, there are very minimal amplitudes in the x-velocity direction. Aft of 75% chord, the amplitudes begin to rise as the distance is increased. This trend continues to the trailing edge, where amplitudes are maximum at approximately 2 m/s. Although a high frequency oscillation appears to exist at the trailing edge, it is

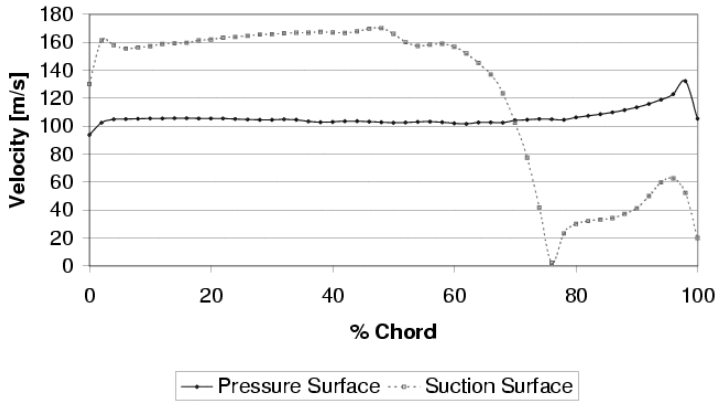

Figure E.3 CFD Velocity Magnitude Over Cascade Blade

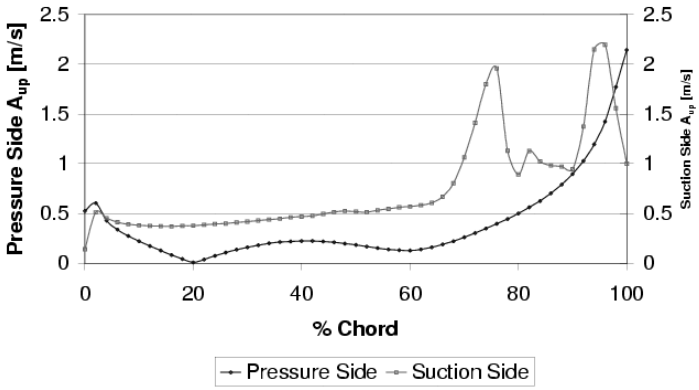

Figure E.4 CFD X-Velocity Amplitudes for Pressure Surface of Blade

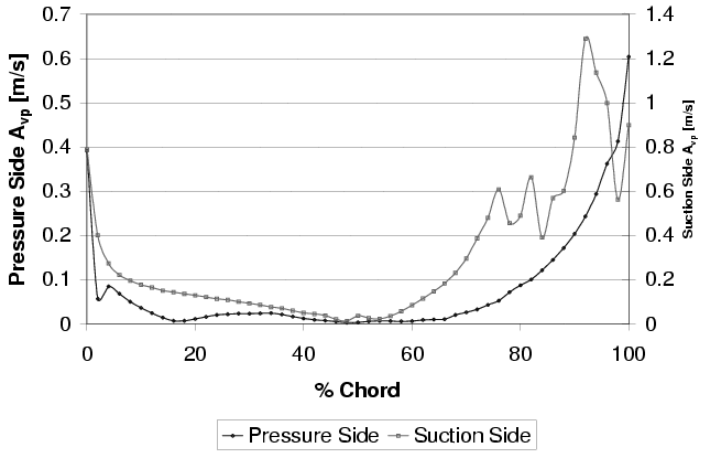

Figure E.5 CFD Y-Velocity Amplitudes for Pressure Surface of Blade

important to note that the unsteady velocity amplitudes at the trailing edge are less than 2% of the free stream velocity.

The suction side of the blade produces very different results. Over the portion of the blade less than 70% chord, the amplitudes are larger than those on the pressure side. The amplitudes also appear to be slowly increasing towards the trailing edge.

The flow separation shown in the steady state results has a very large impact on the amplitudes towards the trailing edge. A sharp increase is present just aft of the separation point, but no coherent pattern in the amplitudes exists farther back. Although the amplitudes of the velocity at all points beyond separation have a higher magnitude than in the non-separated region, there appears to be no increase in amplitude towards the trailing edge as is present on the pressure side of the blade.

The y-velocity amplitudes, shown in Fig. E.5, appear to have many of the same characteristics as the x-velocity results. On the pressure side of the blade, the trend is identical to that shown in Fig. E.4. The amplitudes are minimum through the center portion of the blade and begin to increase towards the trailing edge, however the amplitudes at the trailing edge are less than 1/3 of the amplitudes of the x-velocity component at the trailing edge.

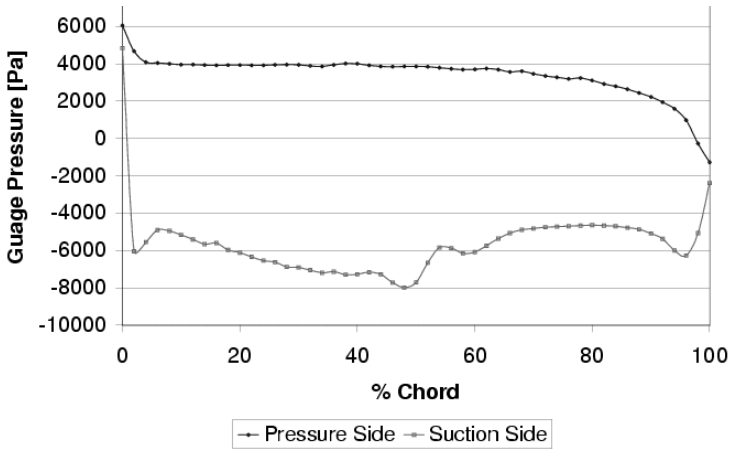

Figure E.6 CFD Pressure Along Cascade Blade

The suction side also exhibits many of the same characteristics as the x-velocity case, including a sharp increase in the amplitudes beyond the separation point. Unlike the x-velocity case, the y-velocity amplitudes are generally constant from 75-88% chord locations. An increase in amplitudes occurs between 88-92% chord prior to falling-off at the trailing edge.

Steady state pressure. The steady state pressure along the blade surface on both the pressure and suction side is shown in Fig. E.6. The results of the pressure are expected for the blade. The pressure on the pressure side of the blade is relatively constant until 80% chord, at which point the pressure is reduced with distance to the trailing edge.

The suction side pressure begins at approximately the same value as the pressure side at the leading edge. Within 2% chord, the pressure drops by 10 kPa to the value fairly constant along most of the suction side. At 98% chord, the pressure is increased and the pressure is approximately identical for both the sides at the trailing edge.

Pressure fluctuations. The amplitudes of the unsteady pressures are shown in Fig. E.7 for both sides of the blade. Like the velocity amplitudes shown in Figs. E.4 and E.5, the pressure amplitudes over the pressure side of the blade increase towards the trailing edge. For most of the blade surface, the amplitudes are minimal; however, an increase begins at 80% chord to the maximum value of 600 Pa at the trailing edge.

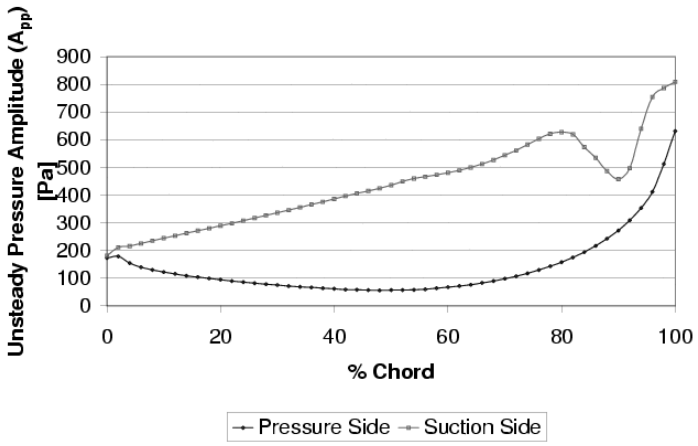

Figure E.7 CFD Pressure Amplitudes Over Blade Surface

A more coherent view of the pressure amplitudes on the suction side exists than is seen with the velocities. Like the pressure side, the amplitudes on the suction side increase towards the trailing edge of the blade. Except for the region between 82-96% chord, the pressure amplitudes increase fairly linearly with chord distance for the entire blade to the maximum value of 800 Pa at the trailing edge of the blade.

The peak pressure amplitudes present at the trailing edge of the blade lead to a possible conclusion that a large amplitude oscillation may exist on the trailing edge, if the phases on the pressure amplitudes are aligned correctly. The combination of the pressure on the two sides of the blade can be clearly seen on the calculations of the force on the blade.

Steady state force on blade. The force on the blade was calculated based on the pressure on both sides of the blade at a chordwise location. The steady state force can be calculated as a simple subtraction of the pressures on each side, by

$$F_{blade} = P_p - P_s \tag{E.1}$$

where P_p and P_s are the pressures on the pressure and suction sides of the blade, respectively. F_{blade} is the resultant pressure which is positive on the suction side of the blade.

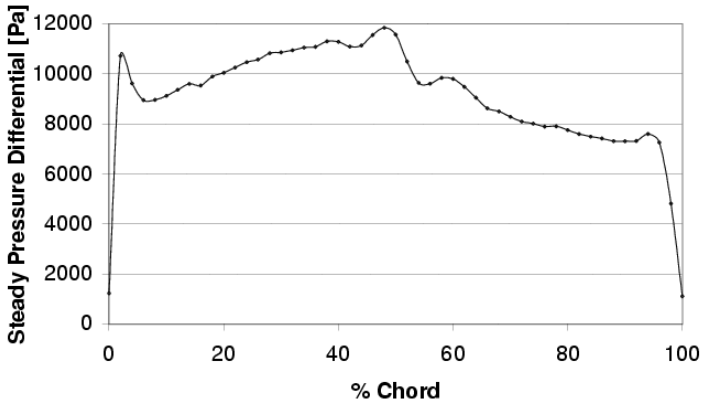

Figure E.8 CFD Steady Force (per Square Meter) On Blade Surface

The resulting steady force over the blade is shown in Fig. E.8. As expected, the force is greatly reduced at the leading and trailing edges with a value of 1100 Pa. The maximum force occurs at the midchord with a force of 12,000 Pa.

Blade force fluctuations. The unsteady force requires an equation more complicated than Eq (E.1) because the summation of the amplitudes are affected by the phase of the sine waves. The equation used is

$$A_{force} = \sqrt{\Big(A_p \cos(\phi_p) - A_s \cos(\phi_s\Big))^2 + \Big(A_p \sin(\phi_p) - A_s \sin(\phi_s\Big))^2} \quad \text{(E.2)}$$

$$\phi_{force} = \tan^{-1}\left(\frac{A_p \sin(\phi_p) - A_s \sin(\phi_s)}{A_p \cos(\phi_p) - A_s \cos(\phi_s)}\right) \quad \text{(E.3)}$$

where A_p and A_s are the amplitudes of the unsteady pressure on the pressure and suction sides, respectively. ϕ_p and ϕ_s are the phase shift for the unsteady pressures for the pressure and suction side. A_{force} is the resulting unsteady force and ϕ_{force} is the phase shift.

The resulting amplitude and phase of the unsteady force are shown in Fig. E.9. The amplitude of the force is low at the leading edge and increases until 80% chord where a maximum value of 500 Pa is present. After 80% chord, the force begins to fall off, even though both the pressure and suction sides of the blade have increasing unsteady pressures, indicating that the pressure and suction side unsteady pressures are in phase.

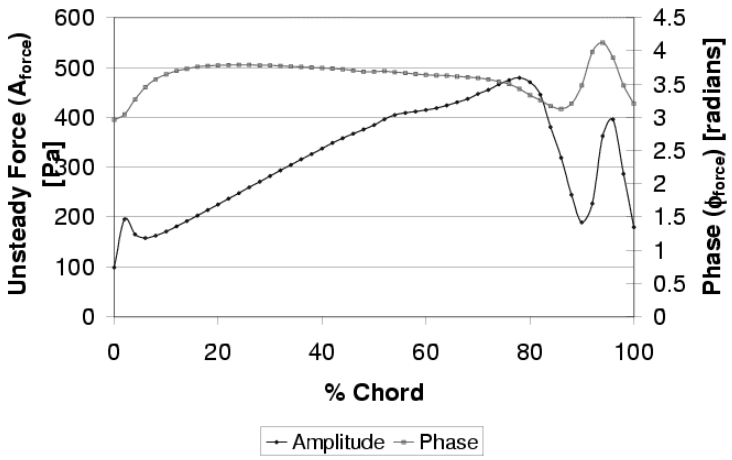

Figure E.9 CFD Unteady Force Amplitude (per Square Meter) On Blade Surface

At the aft of the blade, the unsteady force is reduced with chordwise distance. At the trailing edge, the unsteady force is less than 200 Pa, less than 18% of the steady pressure at that point.

The maximum unsteady pressure, located at 80% chord, is less than 7% of the steady pressure at that point. Thus, at no point does the unsteady pressure approach values close to the steady state pressure.

E.3 Inlet Velocity Effects

The effect of the inlet velocity on the amplitudes was determined by simulating the flow field at 3 different conditions, the baseline and velocities ±25 m/s from the baseline. All other aspects of the simulations were held constant, including the time steps.

Steady state velocity. Inlet velocity has a large impact on the separation point over a blade. The suction side velocity magnitude is shown in Fig. E.10 for the three inlet velocities. All three of the cases have identical properties. The velocity begins to decrease with distance beyond 60% chord. The amplitudes are a minimum at 76% chord for all three of the cases and the amplitudes begin to rise further on the chord line. The inlet velocity appears to have no effect on the separation point on the blade.

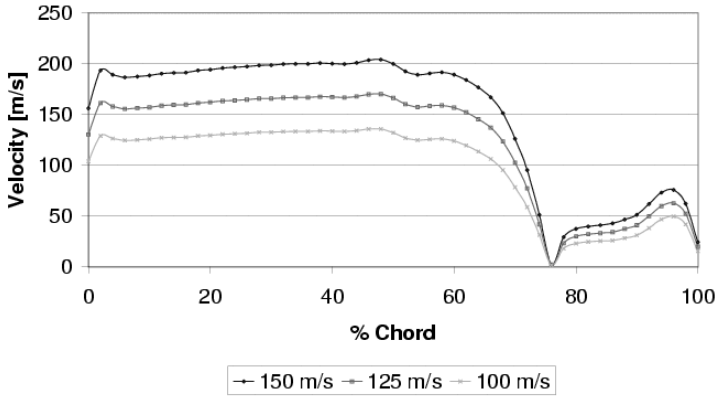

Figure E.10 CFD Velocity Magnitude on Suction Side of Blade for Multiple Freestream Velocities

Velocity fluctuations. The effect of the inlet velocity magnitude on the velocity fluctuations can be seen in Fig. E.11. On the pressure side of the blade, increasing the inlet velocity increases the velocity amplitudes at the trailing edge of the blade. The general shape of the curve remains approximately the same with increasing amplitudes at the leading and trailing edge of the blade.

On the suction side, the separation greatly influences the results, as seen in Fig. E.12. The initial fall-off of velocity shown in Fig. E.10, which begins at 60% chord, leads to increased amplitudes in the x-velocity trace. This increase continues with chordwise location until the minimum velocity magnitude is reached after which the amplitudes begin to fall off. Beyond 80% chord, the only pattern which can be seen is that increasing the velocity increases the peak amplitudes in the region.

The y-velocity results follow the same trends as the x-velocity for both the pressure and suction side. The pressure side y-velocity amplitudes are shown in Fig. E.13. The y-velocity amplitudes are virtually non-existent between 25-60% chord. There is a steady increase towards the trailing edge until 98% chord, where a sharp increase in the y-velocity amplitudes occurs for each of the three cases. The higher velocities lead to higher amplitudes.

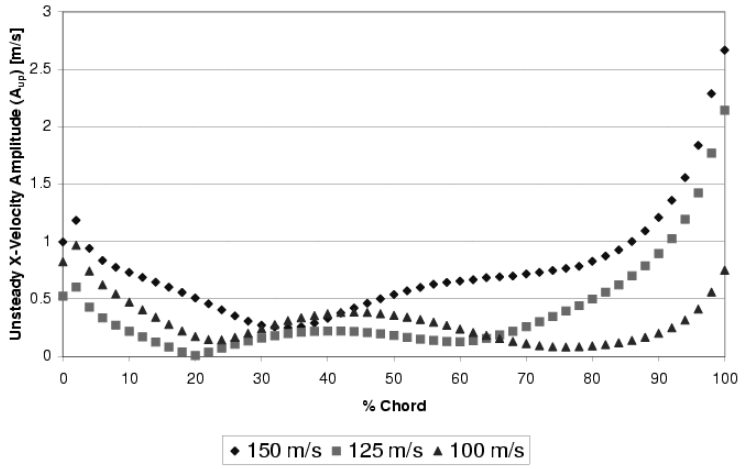

Figure E.11 CFD X-Velocity Amplitude on Pressure Side of Blade for Multiple Freestream Velocities

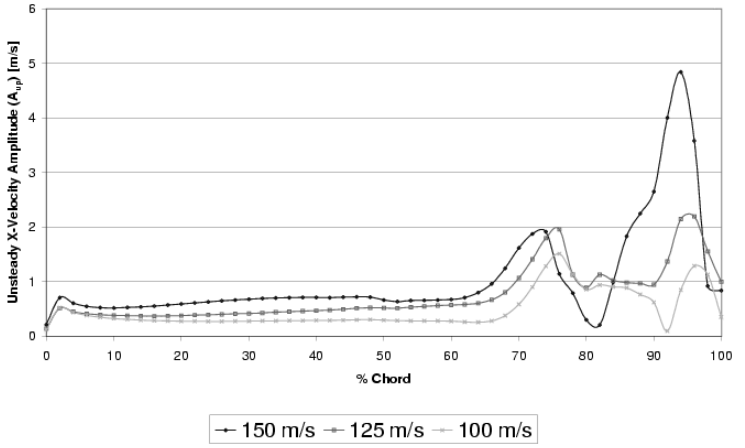

Figure E.12 CFD X-Velocity Amplitude on Suction Side of Blade for Multiple Freestream Velocities

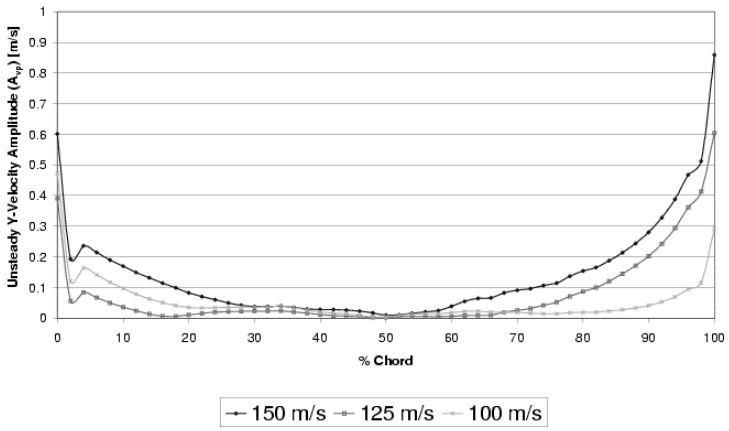

Figure E.13 CFD Y-Velocity Amplitude on Pressure Side of Blade for Multiple Freestream Velocities

Pressure. The effect of different inlet velocities on the amplitudes of the pressure fluctuations for the pressure side of a blade can be seen in Fig. E.14. For each of the three velocities, the pressure amplitudes are increased towards the trailing edge of the blade. Increasing the velocity has the effect of increasing the unsteady pressure at the trailing edge. A increase in the velocity from 100 m/s to 150 m/s leads to an increase of over four times the unsteady pressure amplitude. For each of the velocity cases, the unsteady pressure amplitude reaches a minimum across the center of the blade and increases towards each edge. For the 100 m/s case, the amplitudes of the pressure at the leading edge are larger than the amplitudes at the trailing edge.

The suction side blade pressure amplitudes are shown in Fig. E.15. For each of the cases, there is a slight increase in the amplitudes along most of the chordline. For the 100 m/s case, the amplitudes begin to decrease at 60% chord and the amplitude at the trailing edge is smaller than at the leading edge. For the other two cases, the amplitude increase continues through the separation region and decreases around 80% chord.

Unsteady force. The pressures shown in Figs. E.14 and E.15 were combined using Eq. (E.2) and the resulting force amplitudes are shown in Fig. E.16. For the front 70% of the blade, the two slower velocity cases have identical forces that are increasing with chord distance. The maximum unsteady forces present on the blade increase with

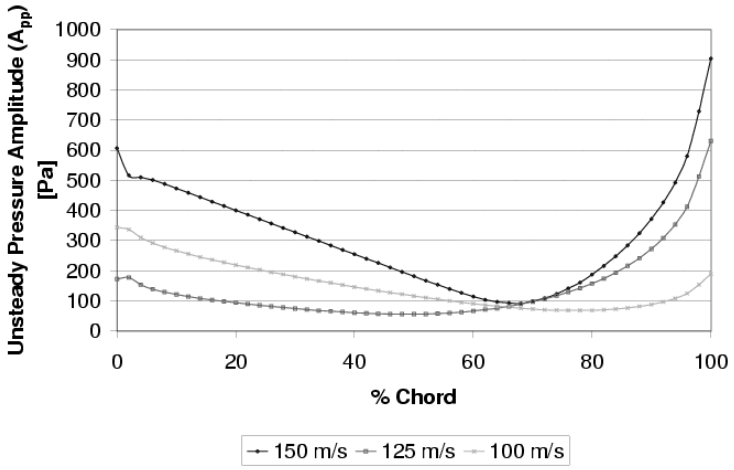

Figure E.14 CFD Pressure Amplitude on Pressure Side of Blade for Multiple Freestream Velocities

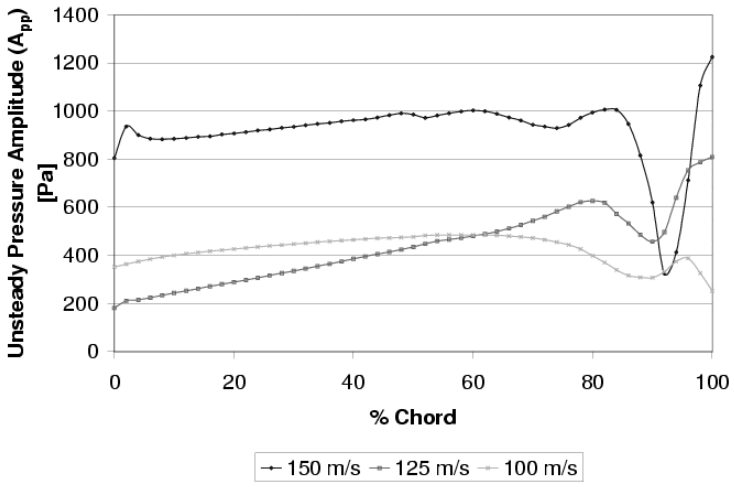

Figure E.15 CFD Pressure Amplitude on Suction Side of Blade for Multiple Freestream Velocities

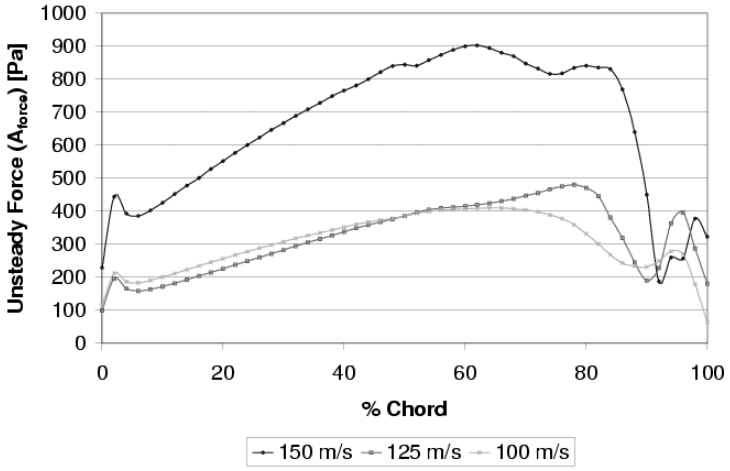

Figure E.16 CFD Force Amplitude (per Square Meter) for Multiple Freestream Velocities

increasing velocity. The maximum force is 400 Pa for the 100 m/s case, 500 Pa for the 125 m/s case, and over 900 Pa for the 150 m/s case. For each of these cases, the maximum amplitudes do not occur close to the trailing edge. The highest trailing edge amplitude is 350 Pa for the 150 m/s case. While increasing the inlet velocity increases the unsteady forces, a strong unsteady force on the trailing edge is not produced.

Cylinder downstream location effects. The effect of the distance between the cascade and the cylinder array was examined using three different downstream cylinder locations. The distances used were 33% chord (1/2 inch), 67% chord, and 100% chord. For all locations, the cylinders were located exactly between the chordlines of the blades forming each passage. The expected influence of the cylinder locations would be a decrease in the amplitudes with downstream distance.

Unsteady velocity. The effect of the downstream location of the cylinder array can be clearly seen in Fig. E.17. As expected, the closer cylinders produce a larger velocity amplitude on the trailing edge. Moving the cylinder from 33% chord to 100% chord reduces the amplitude on the trailing edge by 83%. The three different cylinder locations produce very similar trends, including a rise in the amplitudes towards the trailing edge.

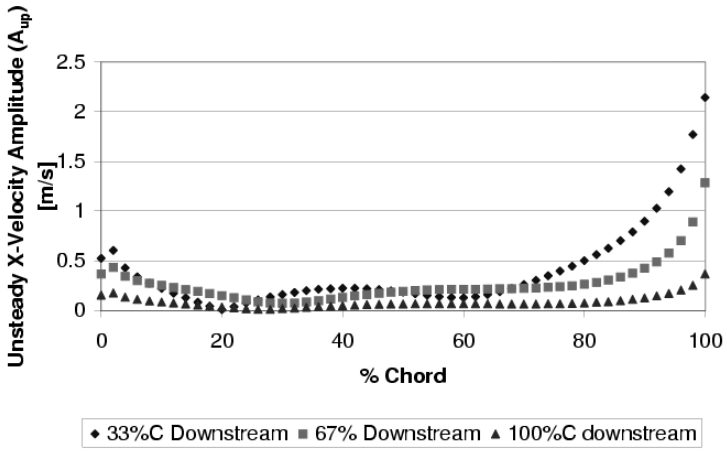

Figure E.17 CFD X-Velocity Amplitude on Pressure Side of Blade for Multiple Downstream Cylinder Locations

The suction side x-velocity amplitudes are shown in Fig. E.18. In front of the separation point, the higher amplitudes correspond to the closer array of cylinders. However, this is not the case in the separated region, where the flow becomes random. At the trailing edge, the velocity amplitudes for all three cases are decreasing. As expected, the closer array of cylinders leads to larger amplitudes.

The y-velocity amplitudes follow the same trends shown in Figs. E.17 and E.18. The main difference is on the suction side where the y-velocity amplitude present at the trailing edge is slightly larger than the amplitude at 98% chord for each of the cases.

Pressure. The downstream cylinder locations greatly affect the unsteady pressure amplitudes over the pressure side of the blade, as shown in Fig. E.14. The same trend exists for each of the three locations, but the closer cylinder array produces the largest amplitudes. Moving the cylinder from 33% to 100% chord results in a decrease of the trailing edge pressure amplitude from 179 Pa down to 42 Pa, a decrease of 77%.

The suction side pressure amplitudes are shown in Fig. E.20. For all points greater than 25% chord, the closer cylinder locations results in larger pressure amplitudes. The pressure amplitudes from the 33% chord case are the only results that increase with chordwise distance over most of the blade. Although a decrease in amplitudes exists beyond

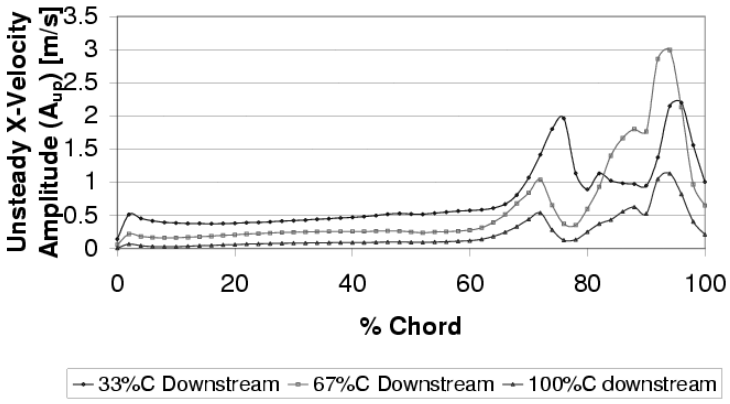

Figure E.18 CFD X-Velocity Amplitude on Suction Side of Blade for Multiple Downstream Cylinder Locations

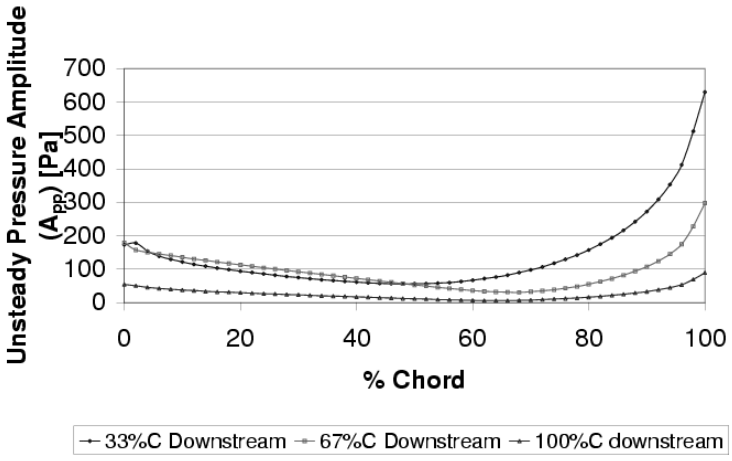

Figure E.19 CFD Pressure Amplitude on Pressure Side of Blade for Multiple Downstream Cylinder Locations

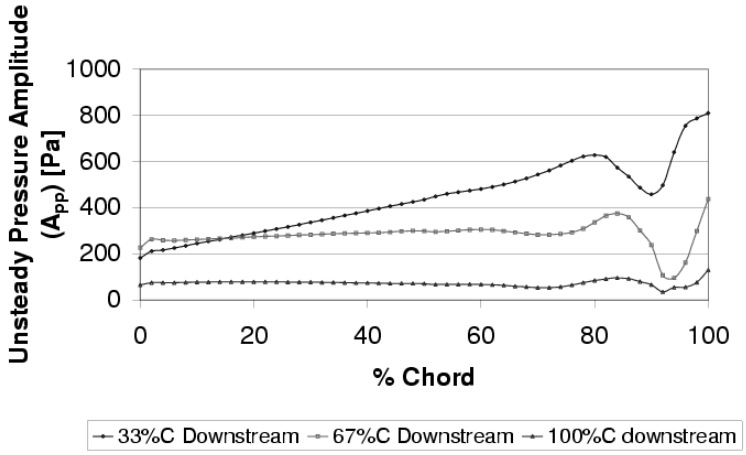

Figure E.20 CFD Pressure Amplitude on Suction Side of Blade for Multiple Downstream Cylinder Locations

the separation point for all three cases, the pressure amplitudes are greatest at the trailing edge. The pressure amplitude at the trailing edge for the 100% chord case is only 16% of the amplitude for the 33% case. For all three cases, the trailing edge pressure amplitudes are larger on the suction side than the pressure side.

Force. Once the unsteady pressure amplitudes are known, the amplitude of the unsteady forces can be calculated to determine if a strong high frequency force is present on the trailing edge. The resultant amplitude of the unsteady force is shown in Fig. E.21. For each of the three downstream cylinder locations, the force at the trailing edge is not the maximum present on the blade. For most points along the blade, the closest cylinder locations results in larger forces. This is only untrue for the region between 85-90% chord where the separation is causing a decrease in the force.

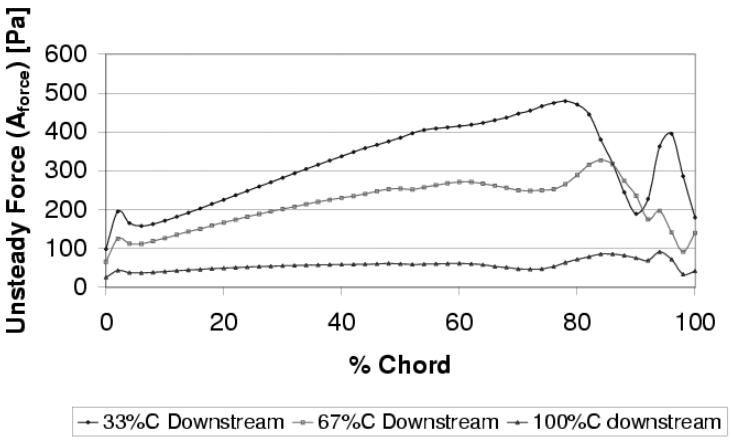

Figure E.21 CFD Unsteady Force Amplitude (per Square Meter) on Blade for Multiple Downstream Cylinder Locations

Appendix F. Hot Wire Control Equations

This appendix very closely follows the development created by Lake.[56] The software used for the hot wire calibration was obtained from Dr. Rolf Sondergaard at AFRL/PRTT and was slightly modified for this application.

F.1 Physical Dimensions

The sensor used for the velocity measurements was a TSI 1240-20 Cross Flow "X" Probe. Each wire had a diameter of 5.08 x 10^{-2} mm (2 x 10^{-3} inches) and had a sensing length of 1.02 mm (0.04 inches). The two wires were placed at a 90° angle to each other and were placed in the flow such that the mean flow split the angle.

F.2 Single Component Velocity Equations

The velocity component measured by each wire was calculated through a series of equations which accounted for the day to day changes in humidity, pressure and temperature. The temperature was a major factor in this work because the tunnel airflow was taken from outside of AFIT and the tunnel then heated that air up to 20°F. The temperature was measured in the stilling chamber where the velocity of the flow was a minimum through the use of a thermocouple. The humidity was obtained from the base weather office. This humidity measurement was used rather than the humidity measured inside the room because the air for the tunnel flow was being obtained externally. The pressure used was obtained from a total pressure sensor located in a stagnation portion of the stilling chamber.

Molecular weight. According to Reid, et al.[57], the molecular weight of the air can be adjusted for the presence of humidity by first calculating the following exponent

$$Z = a_0 + a_1 T_D + a_2 T_D^2 + a_3 T_D^3 + a_4 T_D^4 \tag{F.1}$$

where a_0 through a_4 are constants and T_D is the dew point in Celsius. The humidity mass fraction can then be calculated as

$$m_f = 10^Z \tag{F.2}$$

From the humidity mass fraction calculated by Eq. (F.2), the corrected molecular weight of air can be calculated as

$$M_w = \frac{1}{\left[\frac{1-m_f}{Mw_{air}} + \frac{m_f}{Mw_{water}}\right]} \tag{F.3}$$

where Mw_{air} and Mw_{water} are the molecular weights of dry air and water, respectively

Atmospheric conditions. The specific heat is calculated as

$$c_p = b_0 + b_1 T + b_2 T^2 + b_3 T^3 + b_4 T^4 \tag{F.4}$$

where b_0 through b_4 are constants and T is the temperature.

The gas constant can be calculated using the molecular weight by

$$R = \frac{8314.3}{M_w} \tag{F.5}$$

After c_p and R are known, the ratio of specific heats was calculated as

$$\gamma = \frac{c_p}{c_p - R} \tag{F.6}$$

The speed of sound is calculated by

$$a = \sqrt{\gamma R T} \tag{F.7}$$

The viscosity can be calculated as a function of the temperature as

$$\mu = 1.716 \times 10^{-5} \left(\frac{T}{273.16}\right)^{\frac{3}{2}} \frac{383.716}{T + 110.556} \tag{F.8}$$

and the thermal conductivity is given as a function of temperature as

$$k = 2.414 \times 10^{-2} \left(\frac{T}{273.16} \right)^{\frac{3}{2}} \frac{473.16}{T + 200} \tag{F.9}$$

From these parameters, the Prandtl number is easily calculated by

$$\mathrm{Pr} = \frac{c_p \mu}{k} \tag{F.10}$$

The density can be calculated by

$$\rho = \frac{P}{RT} \tag{F.11}$$

The curve-fits used in the calculation of c_p, μ, and k are valid for temperatures between 275 and 600 Kelvin.

Determination of velocity. The calculation of the velocity begins with the determination of the temperature of the wire. This temperature can be calculated by

$$T_w = \frac{\Omega_{oper} - \Omega_0}{\Omega_{100-0}} \cdot 100 + 273.16 \tag{F.12}$$

where Ω_{oper} is the operating resistance of the wire, Ω_0 is the probe resistance at $0^\circ C$ (provided by probe manufacturer), and Ω_{100-0} is the change in resistance between $0^\circ C$ and $100^\circ C$ (provided by probe manufacturer).

Once the wire temperature is known, the velocity computation routine begins an iterative method to converge the static temperature to the actual value. Initially, a static temperature, T_s, is guessed. This temperature is then used to find the mean temperature, calculated as

$$T_m = \frac{T_{s,guess} + T_w}{2} \tag{F.13}$$

The velocity can then be calculated through the use of four parameters which must be calculated. The first parameter is given by

$$A = \frac{\rho D_w}{\mu} \tag{F.14}$$

where the ρ and μ are calculated using the mean temperature in Eqs. (F.11) and (F.8), respectively.

The second parameter is given as

$$B = E^2 \frac{\Omega_{oper}}{(\Omega_{oper} + 10)^2} \tag{F.15}$$

where E is the voltage acquired from the IFA 100.

The third parameter is

$$C = \left(\frac{T_m}{T_{s,guess}} \right)^{R_T} \tag{F.16}$$

where R_T is the temperature ratio power which is determined during the calibration process. The use of R_T allows the calibration to cover various flow temperatures rather than just a single temperature. For this work, the value for R_T was -5.95×10^{-3}.

The final parameter is calculated as

$$D = 4\pi L_w k \left(T_w - T_{s,guess} \right) \tag{F.17}$$

where L_w is the length of the wire sensor.

The velocity over a single sensor element then becomes

$$V = \frac{\left(\frac{\frac{BC \, \mathrm{Pr}^{-\frac{1}{3}}}{D}}{D_s} - C_i \right)^{\frac{1}{0.45}}}{A} \tag{F.18}$$

The final step in the process was to calculate the new static temperature by

$$T_{s,new} = T_{total} - \frac{0.85 V^2}{2 c_p} \tag{F.19}$$

and $T_{s,new}$ was compared to $T_{s,guess}$. If the difference between the two were within a specified value (0.00005 K was used for this work), then the solution was converged. Otherwise, $T_{s,guess}$ was replaced by $T_{s,new}$ and the iteration was performed again.

F.3 Two Component Velocity

Once the calculated velocity over each wire was known, the velocities could be used to determine the components of the true velocity. The behavior of the x-film sensor prevented the velocities calculated by Eq. (F.18) from being directly converted to the desired velocity components. The wire velocity perpendicular to the wire is a function of both velocity and the angle of the flow. For this reason, a detailed angle calibration was used. This angle calibration was performed at three different velocities, bracketing the expected flow field. the multiple velocities were also required because the velocity impinging on the wire also dictates the angle correlation.

For the angle calibration, the calibrator was set to a single velocity and the probe was rotated between -30° and 30° in 6° increments. This process was repeated for the three velocities. For this work, the angle calibration velocities were 105 m/s, 125m/s, and 150 m/s.

For the data reduction process, the velocities of the wires, u and v, were used to calculate a velocity magnitude by

$$\vec{V}_{est} = \sqrt{u_1^2 + v_2^2} \tag{F.20}$$

The angle was estimated by

$$\alpha_{est} = \tan^{-1}\left(\frac{v_2}{u_1}\right) - \frac{\pi}{4} \tag{F.21}$$

where the $\frac{\pi}{4}$ term is used to correct for the 45° offset between the wires and the defined 0° angle of the flow. The angle is then placed in the angle calibration equation

$$\alpha_{true} = a_{a0,i} + a_{a1,i}\alpha_{est} + a_{a2,i}\alpha_{est}^2 + a_{a3,i}\alpha_{est}^3 \tag{F.22}$$

where $a_{a0,i}$ through $a_{a3,i}$ are calibration constants where i is the velocity regime being used (high, mid, or low) which is determined through the use of $\vec{V}_{est}$

The velocity ratio is calculated from the true angle as

$$R_v = a_{v0,i} + a_{v1,i}\alpha_{true} + a_{v2,i}\alpha_{true}^2 + a_{v3,i}\alpha_{true}^3 \tag{F.23}$$

where R_v is the velocity ratio, $a_{v0,i}$ through $a_{v3,i}$ are calibration constants where i is the velocity regime being used.

Once the velocity ratio is known, the true velocity magnitude can be calculated by

$$\vec{V} = \frac{\vec{V}_{est}}{R_v} \tag{F.24}$$

and the components of the velocity can be determined by

$$\begin{aligned} u &= \vec{V}\cos(\alpha_{true}) \\ v &= \vec{V}\sin(\alpha_{true}) \end{aligned} \tag{F.25}$$

Appendix G. Calculation of Location of Transition to Turbulence

The blade chord location for the transition to turbulence can be approximated using two different models. The first model is a very simple one step method developed by Michel, aptly called the one step method of Michael [31]. This method estimates the transition point based on the momentum thickness, θ, and only accounts for pressure gradients. The second model used in this work to estimate the location of transition is the correlation of Dunham [31]. This method was developed to model the transition location in a flow with both pressure gradients and freestream turbulence.

G.1 The One-Step Method of Michel

The transition point of the flow from laminar to turbulent can be calculated, for a flow influenced only by a pressure gradient, by use of a one step process. Transition occurs when [31]

$$\frac{U(x)\,\theta(x)}{\upsilon} \approx 2.9\,\mathrm{Re}_x^{0.4} \tag{G.1}$$

where Re_x is the local Reynolds number at a point, $U(x)$ is the local velocity outside of the boundary layer, and $\theta(x)$ is the momentum thickness. θ can be calculated from Thwaites' method as [31]

$$\theta^2 \approx \frac{0.45\upsilon}{U^6}\int_0^x U^5 dx \tag{G.2}$$

where U is the local velocity outside of the boundary layer.

For the calculation of transition point, the velocities for the flow outside of the boundary layer were obtained from the CFD results. Experimental velocities were not used because the velocities along the blade were unable to be measured to the leading edge. From the CFD velocities, the momentum thickness is calculated from Eq. (G.2) and is used in Eq. (G.1). The left-hand side of Eq. (G.1) approaches the right-hand side from below. Transition occurs when the left-hand side equals the right-hand side.

For the CFD case with the angle of attack of 19 degrees and the cylinder 1/2 inch downstream, the transition point was calculated. On the pressure side of the blade, the favorable pressure gradient prevented transition from occurring. This was not the case on

the suction side of the blade. Transition occurred at 63% chord, about 10% chord upstream of the separation point from the blade.

G.2 The Correlation of Dunham

The effect of freestream turbulence can be accounted for in the calculation of the transition point through the correlation of Dunham. For a known inlet turbulence and freestream velocity along the blade, the transition point can be calculated. The initial step in the process is to calculate the Thwaites parameter as [31]

$$\lambda = \frac{\theta^2 \left(\frac{dU}{dx}\right)}{\upsilon} \tag{G.3}$$

where θ is calculated from Eq. (G.2). Once the Thwaites parameter is known, the transition point occurs when [31]

$$\frac{U(x)\,\theta(x)}{\upsilon} \approx \left(0.27 + 0.73e^{-80T}\right)\left[550 + \frac{680}{(1 + 100T - 21\lambda)}\right] \tag{G.4}$$

where T is the turbulence (fraction, not percent).

The transition point for same conditions used in the last section was calculated for an inlet turbulence level of 1.5% [36]. The favorable gradient on the pressure surface of the blade prevents transition from occurring. On the suction side, the transition point is 63% chord, the same result calculated from the one-step method of Michel.

References

1. Y. El-Aini, R. DeLaneuville, A. Stoner and Capece, V., "High Cycle Fatigue of Turbomachinery Components - Industry Perspective." AIAA97-3365, 33rd AIAA/ASME/SAE/ASEE Joint Propulsion Conference and Exhibit, Seattle WA, July 6-9 1997.

2. White, Andrew L. *Computational Investigation of Aeromechanical HCF Effects in a Compressor Rotor*. MS thesis, Air Force Institute of Technology, March 2001.

3. Wisler, David C. and Shin, Hyoun-Woo. "Blade Row Interaction and Unsteady Effects in Axial-Flow Compressors and Fans." *Blade Row Interference Effects in Axial Turbomachinery Stages*. Lecture Series 1998-02. February 9-12 1998.

4. Wisler, David C. "The Technical and Economic Relevance of Understanding Blade Row Interaction Effects in Turbomachinery." *Blade Row Interference Effects in Axial Turbomachinery Stages*. Lecture Series 1998-02. February 9-12 1998.

5. Thompson, D. E., "The National High Cycle Fatigue (HCF) Program." Proceeding of the Thrid National Turbine Engine High Cycle Fatigue Conference, February 1998.

6. Thompson, D. E. and Griffin, J. T., "The National High Cycle Fatigue (HCF) Program." Proceedings of the Fourth National Turbine Engine High Cycle Fatigue Conference, March 1999.

7. Canders, A. J. and Fleeter, S. "Blading Response to Potential Field Interactions in Axial- and Radial-Flow Turbomachinery," *Journal of Propulsion and Power*, *14*(2):199–207 March-April 1998.

8. Johnston, Robert T. and Fleeter, Sanford, "Time Resolved Variations of an IGV Flow Field in the Presence of a Rotor Potential Field." AIAA92-96-2670, 32nd AIAA/ASME/SAE/ASEE Joint Propulsion Conference and Exhibit, Lake Buena Vista, FL, July 1-3 1996.

9. Fleeter, Sanford, "Forced Response Unsteady Aerodynamic Experiments." AIAA92-0114, 30th Aerospace Sciences Meeting and Exhibit, Reno NV, January 1992.

10. Wilson, David G. and Korakianitis, Theodosius. *The Design of High-Efficiency Turbomachinery and Gas Turbines*, 317–322. Upper Saddle River NJ: Prentice-Hall, 1998.

11. Korakianitis, Theodosius. "On the Propagation of Viscous Wakes and Potential Flow in Axial-Turbine Cascades," *Journal of Turbomachinery*, *115*:118–127 1993.

12. Korakianitis, Theodosius. "Influence of Stator-Rotor Gap on Axial-Turbine Unsteady Forcing Functions," *AIAA Journal*, *31*:1256–1264 1993.

13. Fabian, Michael K. *Unsteady Pressure Distributions Around Compressor Vanes in an Unsteady, Transonic Cascade*. PhD dissertation, University of Notre Dame, December 1995.

14. Commerford, G.L. and Carta, F.O. "Unsteady Aerodynamic Response of a Two-Dimensional Airfoil," *AIAA Journal*, 43–48 1974.

15. Wille, Rudolf. "Generation of Oscillatory Flows." *Flow-Induced Structural Vibrations*. IUTAM-IAHR Symposium, Aug 1972.

16. Turgut Sarpkaya, Ray L. Shoaff. "An Inviscid Model of Two Dimensional Vortex Shedding for Transient and Asymptotically Steady Separated Flow Over a Cylinder." *AIAA 79-0281*. 1979.

17. Clements, R. R. and Maull, D. J. "The Representation of Sheets of Vorticity by Discrete Vortices," *Progress in Aerospace Science*, *16*(2):129–146 1975.

18. J. Wu, J. Sheridan, M. C. Welsk K. Hourigan M. Thompson. "Longitudinal Vortex Structures in a Cylinder Wake," *Phys. Fluids*, *6*(9):2883–2885 September 1994.

19. P. Le Gal, I. Peschard, M. P. Chauve and Takeda, Y. "Collective Behavior of Wakes Downstream a Row of Cylinders," *Phys. Fluids*, *8*(8):2097–2106 August 1996.

20. Zdravkovich, M. M. "Smoke Observations of the Wake of a Group of Three Cylinders at Low Reynolds Numbers," *Journal of Fluid Mechanics*, *32*(2):339–351 1968.

21. Honji, Hiroyuki. "Viscous Flows Past a Group of Circular Cylinders," *Journal of the Physical Society of Japan*, *34*(3):821–828 1973.

22. Fabian, M. K. and Jumper, E. J., "Unsteady Pressure Distributions Around Compressor Vanes in an Unsteady, Transonic Cascade." AIAA95-0302, 33rd Aerospace Sciences Meeting, Reno NV, January 1995.

23. Fabian, M. K. and Jumper, E. J. "Rearward Forcing of an Unsteady Compressible Cascade," *Journal of Propulsion and Power*, *15*(1):23–30 Jan-Feb 1999.

24. M. K. Fabian, E. A. Falk and Jumper, E. J. "Upstream-Propagating Potential Disturbances Interacting with A Compressible Cascade," *Journal of Propulsion and Power*, *17*(2):240–247 March-April 2001.

25. E. A. Falk, E. J. Jumper, M. K. Fabian and Stermer, J. "Upstream-Propagating Potential Disturbances in the F109 Turbofan Engine Inlet Flow," *Journal of Propulsion and Power*, *17*(2):262–269 March-April 2001.

26. Eric A. Falk, Eric J. Jumper, Michael K. Fabian Brenda A. Haven, "A Characterization of the Unsteady Velocity Field Aft of the F109 Turbofan Rotor." AIAA99-0237, 37th Aerospace Sciences Meeting and Exhibit, Reno NV, January 11-14 1999.

27. Eric A. Falk, Joel F. Kirk, Eric J. Jumper Brenda A. Haven and Stermer, Jerry, "Unsteady Forcing of an IGV Forward of a Fan in Subsonic Flow: Amplitude Results." AIAA2001-3475, 37th AIAA/ASME/SAE/ASEE Joint Propulsion Conference and Exhibit, Salt Lake City UT, July 8-11 2001.

28. Hopper, David R. *Measurements of the Effects of Tunnel Wall Proximity on the Velocity Field Upstream of a Rod with Vortex Shedding in Low-Speed Flow*. MS thesis, Air Force Institute of Technology, March 2000.

29. Fabian, Michael K. and Jumper, Eric J., "Convected and Potential Unsteady Disturbances Interacting with an Unsteady Cascade." AIAA96-2672, 32nd

AIAA/ASME/SAE/ASEE Joint Propulsion Conference, Lake Buena Vista FL, July 1-3 1996.

30. Fabian, M. K. and Jumper, E. J., "Upstream-Propagating Acoustic Waves Interacting with a Compressible Cascade." AIAA97-0380, 35th Aerospace Sciences Meeting and Exhibit, Reno NV, January 6-9 1997.

31. White, Frank M. *Viscous Fluid Flow* (Second Edition). McGraw-Hill, 1991.

32. Fung, Y.C. *An Introduction to the Theory of Aeroelasticity*. Dover Publications, 1993.

33. Unal, M F and Rockwell, D. "On Vortex Formation From a Cylinder. I - The Initial Instability," *Journal of Fluid Mechanics*, *190*:491–529 May 1988.

34. Chyu, C-K; Rockwell, D. "Karman Vortex Development - Relation to Symmetry and Circulation," *AIAA Journal*, *34*(9):1954–1956 September 1996.

35. Szepessy, Stefan. "On the Spanwise Correlation of Vortex Shedding From a Circular Cylinder at High Subcritical Reynolds Number," *Phys. Fluids*, *6*(7):2406–2416 July 1994.

36. Allison, Dennis M. *Design and Evaluation of a Cascade Test Facility*. MS thesis, Air Force Institute of Technology, 1982.

37. TSI Incorporated, "Innovation In Thermal Anemometry: A Complete Family of Thermal Anemometry Systems, Probes, and Accessories."

38. Dantec, "StreamLine/StreamWare Installation and User's Guide," 2000.

39. Kulite, "Kulite Miniature IS Silicon Diaphragm Pressure Transducer Catalog." Bulletin KS-1000E.

40. Vishay Measurements Group, "Signal Conditioning Amplifier Model 2310 Instruction Manual," April 1997.

41. Omega, "DP41-TC, DP41-RTD High Performance Temperature Indicator Operator's Manual," 1994. Number M1296/0991.

42. National Instruments, "The Measurement and Automation Catalog," 2002.

43. Richard K. Burden, J. Douglas Faires. *Numerical Analysis* (5th Edition). PWS Publishing Co., 1993.

44. Fisk, Timothy E. *Comparison of Split-Film and X-Film Measurements in 2-D Flow*. MS thesis, Air Force Institute of Technology, November 1988.

45. *TSI Split Film Sensor Calibration and Application*. Technical Bulletin TB 20.

46. Wheeler, Anthony J. and Ganji, Ahmad R. *Introduction to Engineering Experimentation*. Prentice-Hall Inc., 1996.

47. Yuki Ohya, Atsushi Okajima, Masanori Hayashi. *Wake Interference and Vortex Shedding*, chapter 10, 323–389. Encyclopedia of Fluid Mechanic Vol 8, Gulf Publishing Co., 1989.

48. Hamakawa, Hiromitsu; Fukano, Tohru; Nishida Eiichi, "Vortex Shedding From Serrated-Fin-Tube Banks." AIAA Paper 2000-2001, 6th AIAA/CEAS Aeroacoustics Conference and Exhibit, Lahaina, HI, June 12-14 2000.

49. Fluent Inc., "Fluent 6.0 User's Guide," Nov 2001.

50. Amtec, "Mesh Generator Version 1.0 User's Guide," 1999.

51. Hsu, S. T. and Wo, A. M. "Near-Wake Measurement in a Rotor/Stator Axial Compressor Using Slanted Hot-Wire Technique," *Experiments in Fluids*, *23*(5):441–447 1997.

52. Edevco, "Edevco Instrumentation Catalog," Aug 1999.

53. Bruun, H. H. *Hot Wire Anemometry: Principles and Signal Analysis*. Oxford: Oxford University Press, 1995.

54. Pointwise, "Gridgen Version 14 User Manual," 2002.

55. Chapra, Steven C., Canale Raymond P. *Numerical Methods for Engineers* (2nd Edition). McGraw-Hill Publishing Co., 1988.

56. Lake, James P. *Flow Separation Prevention on a Turbine Blade in Cascade at Low Reynolds Number*. PhD dissertation, Air Force Institute of Technology, June 1999.

57. Reid, R.C., Prausnitz J.M. and Polling, B.E. *The Properties of Gases and Liquids* (Fourth Edition). New York: McGraw Hill, 1987.

Vita

Mr. Wade lived in Maryland until entering college at Virginia Tech in 1989 where he studied Aerospace Engineering. While at Va. Tech, Mr. Wade was enrolled in Air Force ROTC and the Corps of Cadets.

Upon graduation and comissioning in December, 1993, Lt. Wade was assigned to the Flight Dynamics Directorate of Wright Laboratory at Wright-Pattersion AFB. At Wright Lab, Lt. Wade worked on the development nonintrusive diagnostic techniques for use in the Air Force wind tunnels including Doppler Global Velocimetry and Global Holographic Interferometry. While assigned to Wright Lab, Lt Wade completed his Masters degree in Aerospace Engineering from the University of Dayton. His area of study for this degree was external aerodynamics.

In 1997, Lt. Wade was accepted into the Education With Industry (EWI) program and was assigned to Southwest Research Institute in San Antonio, Texas for 10 months. While at SwRI, Lt Wade worked as a SwRI employee on developing software to aid Air Force maintainence personnel in troubleshooting the Line Replacable Units on A-10 aircraft.

Upon completion of the 10 month EWI program, Capt Wade was assigned to the Human Systems Program Office (SPO) located at Brooks AFB in 1998. While at the SPO, Capt Wade worked on both the Aircrew Eye and Resporatory Protection (AERP) program and the Aircrew Laser Eye Protection (ALEP) program.

In 1999, Capt. Wade was assigned to AFIT and began his Doctor of Philosophy under Dr. King. Experimental and computational work were completed in August 2002.